UNIVERSITAT POLITÈCNICA DE VALÈNCIA

_ TELECOM ESCUELA TÉCNICA VLC SUPERIOR DE INGENIERÍA DE TELECOMUNICACIÓN

# UNIVERSITAT POLITÈCNICA DE VALÈNCIA

## School of Telecommunications Engineering

# Photonic reservoir computing with tunable interconnections using electro-optic modulators

**Master's thesis**

**Master's Degree in Telecommunication Engineering**


**AUTHOR: Francisco Pastor Naranjo**

**Tutor: José Capmany Francoy**

**External cotutor: Jeroen Beeckman**

**External cotutor: Peter Bienstman**

**External counsellor: Enes Lievens**

**External counsellor: Ruben Van Assche**


**ACADEMIC YEAR: 2023/2024**

# Acknowledgements

First, I would like to thank my two counsellors, Enes and Ruben, for the constant help, guidance and patience. Without you, it would have been impossible to finish this work, and I am very proud we did it.

También me gustaría agradecer a todas las personas que he conocido en Gante, que me han acompañado en este año lleno de retos. No ha sido un año fácil, han habido momentos buenos y malos, pero he tenido en quien apoyarme cada día y eso es un lujo que no todo el mundo puede decir que tiene. Quiero hacer especial mención a mi amigo Arrey, que me ha enseñado más que nadie en este tiempo. Sé que te va a ir muy bien en la vida, amigo mío.

Agradecer por supuesto a mi padre, Luis, a mi madre, Valery, a mi hermano, Álvaro, y a mi hermana, Kyra, por estar siempre ahí, apoyándome en la distancia. A mis abuelas, Águeda y Sacramento, por su amor incondicional. A mi compañero de piso, Arturo, que este año (y de ahora en adelante) se ha convertido también en mi familia. A mi familia adoptiva, Gustavo, Rosa y María, que también me han apoyado y aguantado en todo este tiempo y con este trabajo. Y por último, a mi novia, Ana, que siempre está, tanto en las buenas como en las malas, que me quiere más que nadie y que la quiero con locura.

Y mucha más gente que no pongo pero que agradezco que estén en mi vida.

Gracias a todos por haberme ayudado a llegar hasta aquí.

# Abstract

The constant increase in throughput demand due to the steady growth of Internet traffic [1] requires systems with ever-greater capabilities for data management and processing. With Moore's law approaching its limits, new computing paradigms must be explored [2]. Neuromorphic computing, inspired by principles from neuroscience, aims to mimic the behaviour of the brain to create efficient computing systems [3]. Reservoir computing is a neuromorphic approach that leverages a fixed, recurrent network with complex nonlinear dynamics, called a reservoir, to transform input signals into a higher-dimensional space. The reservoir's output is then processed by a simpler readout layer, which is trained to produce the desired output through linear regression. This architecture is well-suited for implementation with physical systems, as it does not require gradient-based optimization techniques, which are often challenging to apply. Photonic integrated circuits, known for their efficiency and speed, are ideal candidates for integrating such architectures [4].

In this work, a tunable photonic spatially distributed reservoir architecture has been studied, simulated, and fabricated. Tunability is achieved by placing PZT electro-optic modulators in the interconnections between nodes, where they act as phase shifters that modify the system's dynamics. The reservoir nodes are implemented using 3x3 multi-mode structures, while the readout is realized as a linear combination of the reservoir output with weights in the electrical domain.

The objective is to evaluate how phase variations affect the dynamics and analyze the performance of the circuit in a reference problem, which involves calculating the XOR between consecutive bits of an input bitstream. A mathematical study shows that using two 3x3 MMIs as nodes and two phase shifters is sufficient to compute the XOR with an ideal input signal.

The primary configuration examined in this study is a 2x2 reservoir in a swirl architecture, where only two consecutive nodes are used to input signal to the reservoir, and two phase shifters in the interconnections between such nodes acting as tunable parameters. During simulations, this architecture and variations from it have been tested for various signal distortions, including phase and intensity noise, high power effects and chromatic dispersion. The results show that incorporating configurable parameters significantly improves circuit performance. They also reveal that this tunable setup outperforms higher-dimensional, non-tunable reservoirs and demonstrates the feasibility of using non-volatile phase shifters. Additionally, the study investigates whether utilizing all nodes for input signals is beneficial and explores the impact of recurrency on the circuit behavior. The layout design and fabrication process of a chip implementing the studied reservoir are also presented.

# Extended abstract

1st Francisco Pastor Naranjo
MSc student
Universiteit Gent
Gent, Belgium
francisco.pastornaranjo@ugent.be

2nd Enes Lievens
Liquid Crystals and Photonics Group
Universiteit Gent
Gent, Belgium
enes.lievens@ugent.be

3rd Ruben Van Assche
Photonics Research Group
Universiteit Gent
Gent, Belgium
ruben.vanassche@ugent.be

4th Jeroen Beeckman
Liquid Crystals and Photonics Group
Universiteit Gent
Gent, Belgium
jeroen.beeckman@ugent.be

5th Peter Bienstman
Photonics Research Group
Universiteit Gent
Gent, Belgium
peter.bienstman@ugent.be

Abstract—This work investigates the dynamics of a spatially distributed photonic reservoir system with phase shifters integrated into the interconnections between nodes. The system features PZT electro-optic modulators as phase shifters, 3x3 multi-mode structures as nodes, and an electrical readout that performs a linear combination of reservoir outputs. The study focuses on computing an XOR operation between consecutive bits of a given bitstream. Various architectures and input signals with different distortions are analyzed to evaluate the circuit's response. The primary configuration is a 2x2 reservoir, where two nodes are used to input signal to the reservoir, and two phase shifters serve as tunable parameters. The simulation results indicate that this tunable setup outperforms higher-dimensional, non-tunable reservoirs, and demonstrate the feasibility of using non-volatile phase shifters. Additionally, the study explores using all nodes to input signal to the reservoir, the network's complexity requirements in terms of nodes, and the impact of recurrency on performance.

Index Terms—neuromorphic computing, photonic integrated circuits, reservoir computing, photonic neuromorphic circuits, spatially distributed reservoir.

The rapid growth in data traffic [1], driven by digitalization [2], IoT [3] and AI applications [4], is beginning to outpace the capabilities of traditional Von Neumann architectures. With Moore's law reaching its limits [5], there is an urgent need for new computing paradigms. Neuromorphic computing, inspired by the human brain's analog and parallel processing, offers a promising alternative [6]. While artificial neural networks excel in non-temporal tasks, they struggle with time-varying signals. Recurrent neural networks (RNNs) introduced feedback loops to address this, but their complexity limits generalization.

Reservoir computing is a computational approach that leverages the rich interactions of a fixed non-linear dynamic systems, known as reservoirs, to transform input signals into higher-dimensional spaces. A readout layer, then extracts the relevant information from this representation to produce the final output. This approach is particularly efficient for processing time-varying signals, as the reservoir's dynamics can capture temporal patterns effectively. Unlike traditional deep learning models, which rely on gradient-based optimization for training, reservoir computing simplifies the process by only training the readout layer while keeping the reservoir fixed [7]. This characteristic makes reservoir computing well-suited for physical implementations, such as using Photonic Integrated Circuits (PICs), where tracking gradients can be challenging.

PICs bring speed and efficiency to reservoir computing, with their inherent fabrication randomness aligning well with the random interconnections needed in reservoir stages. Advances in photonic neuromorphic circuits have primarily focused on spatially distributed reservoirs and delayed feedback loops [7]. Early designs with cascaded SOAs as the reservoir [9] evolved into complex architectures such as the "swirl" topology and "four-port" architecture, improving tasks like speech recognition and signal equalization [9], [10]. Further innovations include multimodal Y junctions, external optical feedback systems, all-optical readout systems, and silicon microring resonators (MRRs), which have expanded the capabilities of photonic reservoirs for high-speed, efficient computing [11]–[13].

This project aims to develop a tunable spatially distributed reservoir computing architecture using multimode structures as nodes on a Silicon on Insulator (SOI) platform. The main goal is to design, fabricate, and evaluate a PIC with phase shifters embedded in node interconnections for tunability. The study includes optimizing reservoir dimensions, analyzing performance mathematically, simulating responses under various distortions, and comparing non-volatile and regular phase shifters. The work also involves the practical design and fabrication of the PIC, followed by experimental validation against simulation results. The thesis is structured to provide a comprehensive exploration of these aspects, culminating in conclusions and directions for future research.

## I. Problem formulation

The chosen problem to evaluate the reservoir consists of calculating the XOR between consecutive bits of an input bitstream using a spatially distributed photonic reservoir with an electrical readout. The input bitstream is generated via on-off keying modulation. It is then propagated through the photonic reservoir, and the output is converted to the electrical domain via direct detection. The final result is obtained through a linear combination of the detected signals.

The XOR operation is challenging due to its non-linear nature, requiring a specially configured reservoir for linear separation. Real-world factors like noise and distortions add complexity, so simulations must consider both ideal and distorted signals. Moreover, the XOR problem is useful for initial studies because its low memory requirements simplifies the circuit design and optimization.

The objective is to identify the optimal parameters $\theta$ for the reservoir and $\phi$ for the readout stage to achieve accurate XOR computation from a bitstream $U = (u[1], u[2], \ldots, u[N])$, producing an output $\hat{Y} = (\hat{y}[1], \hat{y}[2], \ldots, \hat{y}[N])$ that aligns with the XOR logic gate, whose true value is $Y = (y[1], y[2], \ldots, y[N])$. In other words:

$$\hat{Y} = g_\theta \circ f_\phi(U) = XOR(U) \tag{1}$$

Mathematically, the reservoir stage $g_\theta$ is defined as:

$$x[n+1] = \sigma(W^{res}x[n] + W^{in}u[n]) \tag{2}$$

where $x[n]$ represents the reservoir state, and $W^{in}$ and $W^{res}$ denote the input and reservoir weight matrices, respectively. The readout stage $f_\phi$ is described by:

$$\hat{y}[n] = W^{out}x[n] \tag{3}$$

where $W^{out}$ are the linear weights mapping the reservoir state to the output space. The delay $\tau$ before computing the linear regression is also optimized. The linear weights are obtained using the Moore-Penrose pseudoinverse [14]:

$$W^{(out)} = (X^\intercal X + \beta I)^{-1} X^\intercal Y \tag{4}$$

where $X$ is the vectorial notation for the reservoir state $x[n]$, and $\beta \in [0, 1]$ is a regularisation term that also needs to be optimized.

## II. Physical implementation

The physical implementation of the reservoir circuit is designed on a Silicon on Insulator (SOI) platform using PZT electro-optic modulators. The aim is to create a tunable photonic reservoir with both optical and electrical components, allowing control over the system's dynamics to perform the XOR operation. The circuit is based on a 2x2 swirl topology, where each node is a 3x3 structure formed either by cascaded 2x2 balanced MMIs or 3x3 balanced MMIs.

The circuit's nodes are interconnected with phase shifters, placed between each pair of nodes, enabling full control over the reservoir's dynamics. The interconnections are designed to include a delay of exactly one bit period, ensuring synchronized interactions between incoming bits. The readout stage of the circuit is handled electrically, where the signals from the photodetectors are combined through a weighted sum. These weights are adjustable, allowing for optimization of the XOR operation.

The diagram of the full system (Figure 1) illustrates the key components: the reservoir stage where the signal is processed, and the subsequent electrical stage where a linear combination of the signals is performed. This implementation allows for the physical realization of the equations described in the previous section, with the electrical weights corresponding to $W^{out}$ and the phase shifts in the reservoir corresponding to $W^{in}$ and $W^{res}$.

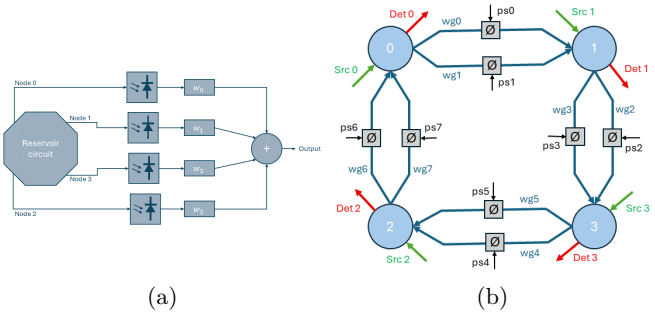


(a) (b)

Fig. 1: Schematic view of the implemented reservoir computing architecture. (a) Complete system. (b) Reservoir circuit.

## III. Mathematical analysis

The analysis evaluates a simplified circuit model for XOR computation under ideal conditions. Using nodes 0 and 1 for signal input, along with phase shifters 0 and 1, proved to be the minimal complexity configuration capable of computing XOR. Outputs from nodes 2 and 3, as well as feedback signals, were excluded from this study.

In this setup, the intensity output at node 0 is directly the bit symbol, and the intensity output at node 1 was calculated based on wave interference, as described in Equation 5. The intensities of both nodes for all the bit combinations is summarized in Table I.

$$I = \frac{1}{3}(I_{t=1} + I_{t=0}\frac{2}{3}x(1 + \cos(\Delta\phi_0)) + \sqrt{I_{t=1}I_{t=0}}\frac{2}{\sqrt{3}}\sqrt{x}(\cos(\Delta\phi_1) + \cos(\Delta\phi_2))) \tag{5}$$

To achieve XOR computation, the reservoir output must be linearly separable in this new space, requiring a specific phase shifter configuration. Figure 2 depicts such intensities, and it shows that, to reach the separability, the following condition must hold:

TABLE I: Simplified intensities resulting from the interference of all posible bit configurations.

| Input intensity | | Output normalized intensity | |
|---|---|---|---|
| t=1 | t=0 | Node 0 | Node 1 |
| 0 | 0 | 0 | 0 |
| 0 | 1 | 0 | $\frac{2}{3}x(1+\cos(\Delta\phi_0))$ |
| 1 | 0 | 1 | 1 |
| 1 | 1 | 1 | $1+\frac{2}{3}x(1+\cos(\Delta\phi_0))+\frac{2}{\sqrt{3}}\sqrt{x}(\cos(\Delta\phi_1)+\cos(\Delta\phi_2))$ |

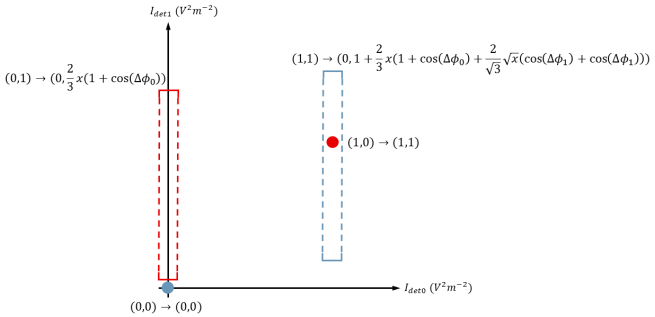


Fig. 2: Transformed space after observing the output of nodes 0 and 1. Proper use of the phase shifters allows to find the separability condition.

$$1+\frac{2}{3}x(1+\cos(\Delta\phi_0))+ \frac{2}{\sqrt{3}}\sqrt{x}(\cos(\Delta\phi_1)+\cos(\Delta\phi_2)) < 1 \tag{6}$$

Analyzing phase shifter values, a configuration with $\Delta\phi_0 = 0$, $\Delta\phi_1 = \pi$, and $\Delta\phi_2 = \pi$ shows that within the loss range $x < 3$, the linear separation is achieved, which is always true. The behavior for $x = 0.8998$ is shown in Figure 4, illustrating the required phase shifts for separability in that case.

Further analysis reveals that for $\Delta\phi_1 = \pi$ and $\Delta\phi_2 = \pi$, the maximum allowable phase error is approximately 56.79°. The minimum resolution for non-volatile phase shifters is also calculated, showing that three states are needed to ensure reliable operation.

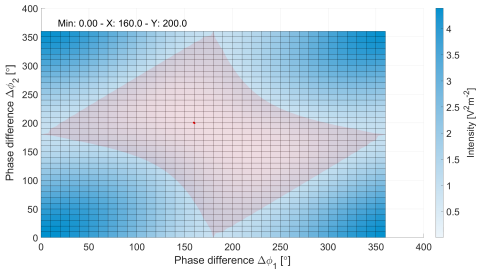


Fig. 3

Fig. 4: Instensity from node 1 with respect to the different possible combination of values of $\Delta\phi_1$ and $\Delta\phi_2$. The red plane determines the configurations that reach the separability condition.

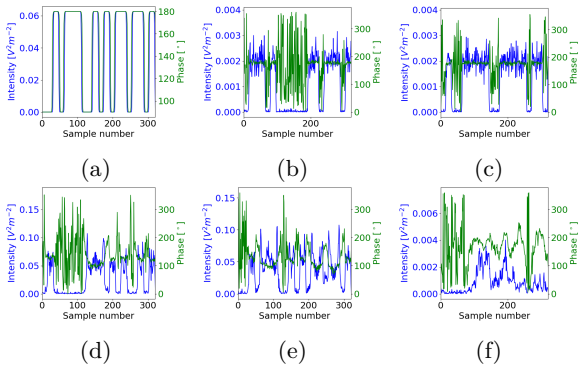


Fig. 5: Signals generated by 6 different configurations of setup parameters summarized in Table II.

| Figure | Chromatic dispersion compensation | Signal power | Amplifier noise |
|---|---|---|---|
| a | Ideal signal | | |
| b | Yes | 3 dBm | No |
| c | Yes | 3 dBm | Yes |
| d | Yes | 18 dBm | No |
| e | Yes | 18 dBm | Yes |
| f | No | 3 dBm | No |

TABLE II: Configurations used by the transmission setup to generate the simulation signals.

## IV. Signal generation

For the generation of the signals used in the simulations, the transmission setup employed is composed of a laser, an OOK modulator, a 25km fiber and a linear amplifier. While not all possible distortions were considered, key effects such as intensity and phase distortions were included.

Figure 5 and Table II illustrate the generated signals under different configurations of the setup parameters. The intensity of the 'on' and 'off' states and certain phase coherence of the 'on' states can be observed, indicating that the system could be functioning as in the mathematical analysis when no chromatic dispersion is involved.

## V. Simulation

Each experiment involves simulating various phase shifter configurations for specific source signals and circuit setups. Following the minimum complexity criteria, only nodes 0 and 1 are used for signal input, and only phase shifters 0 and 1 are evaluated. Each phase shifter is tested with 36 values, resulting in 1296 simulations per seed. Performance is assessed using error heatmaps, and the effects of non-volatile phase shifters are also investigated. Initial experiments with a single seed filter out irrelevant signals. Multi-seed experiments follow with relevant signals and alternative architectures.

The parameter sweep process includes 1296 iterations to test all phase shifter combinations. Performance is evaluated using the bit error rate (BER). To optimize readout weights for XOR computation, three datasets are used: training ($\mathcal{D}_{\text{train}}$), validation ($\mathcal{D}_{\text{val}}$), and test ($\mathcal{D}_{\text{test}}$), each with 1000 symbols and XOR target labels.

The procedure starts with random phase shift initialization. Phase shifter values are applied, and the $\mathcal{D}_{\text{train}}$ bitstream is propagated through the reservoir. Linear regression weights are computed, and BER is evaluated for $\mathcal{D}_{\text{val}}$. The configuration with the lowest validation error is used to recalculate weights with $\mathcal{D}_{\text{train}}$, and final BER is assessed on $\mathcal{D}_{\text{test}}$. This process continues until all iterations are complete, resulting in the final heatmaps.

## A. Single-seed experiments

In this part, the qualitative and quantitative analysis of the signals from Figure 5 is carried out. Figure 6 illustrates the heatmaps from the test BER of every parameter configuration for each experiment. Figure 7 includes a red mask indicating which regions from such heatmaps are computed with the minimum time delay. Table III and Table IV provide a statistical evaluation of the previous heatmaps.

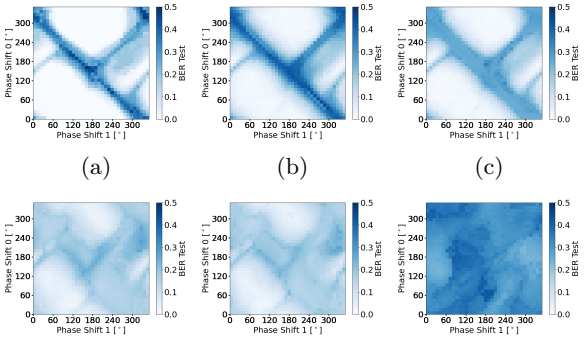


Fig. 6: Test BER heatmaps for every experiment from Table II.

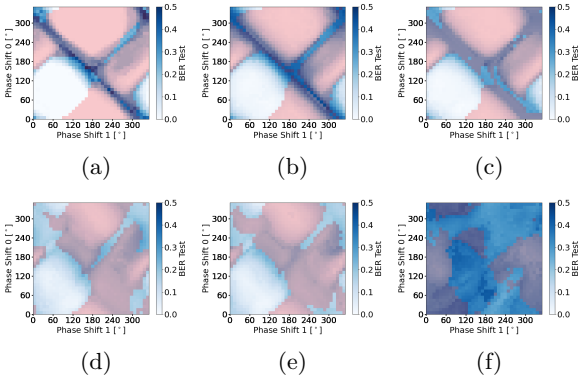


Fig. 7: Masked test BER heatmaps for every experiment from Table II.

First, we can observe that there are regions of high error in all the cases, which underscores the need for tunable parameters in the reservoir. Then, we see that the response of the reservoir remains the same for all the signals except when chromatic dispersion is present, which means that the same configurations are always providing similar results. The optimal performance in low distortion signals has lower error than higher distorted signals, and their low error regions are also larger. However, the more distorted signals have better performance in high error regions, so their behaviour is more stable. Regarding the signal with chromatic dispersion, the circuit lacks complexity to handle this kind of data.

The masked heatmaps show that adding extra nodes to the minimum computing unit (2-node stage) increases the richness of the circuit, which enables additional low error regions and improves the performance in high error regions, especially in signals with high distortion.

The gain from the metrics is high enough to justify the use of phase shifters. Moreover, the quantized metrics are comparable to the regular metrics so, in principle, the non-volatile phase shifters might be a good option in this setup.

| Exp | Metrics | | | | |
|---|---|---|---|---|---|
| | Error | Worst | Best | Ratio | Effective ratio |
| a | 0.1064 ± 0.1272 | 0.4880 | 0.0 | inf | inf |
| b | 0.1543 ± 0.1308 | 0.4560 | 0.0021 | 215.0 | 72.8082 ± 61.6737 |
| c | 0.1326 ± 0.1017 | 0.3464 | 0.0011 | 326.6535 | 125.1353 ± 95.8403 |
| d | 0.1417 ± 0.0570 | 0.2821 | 0.0244 | 11.5652 | 5.8138 ± 2.3331 |
| e | 0.1393 ± 0.0552 | 0.2712 | 0.0201 | 13.4594 | 6.9178 ± 2.7346 |
| f | 0.3218 ± 0.0406 | 0.4252 | 0.2309 | 1.8414 | 1.3939 ± 0.1754 |

TABLE III: Metrics quantifying the performance of the reservoir architecture for the different signals shown in Table II.

| Exp | Quantized metrics | | | |
|---|---|---|---|---|
| | Worst | Best | Ratio | Effective ratio |
| a | 0.4020 ± 0.0539 | 0.0 ± 0.0 | inf | inf |
| b | 0.4089 ± 0.0218 | 0.0064 ± 0.0022 | 73.8673 ± 32.9528 | 28.4067 ± 28.1531 |
| c | 0.2917 ± 0.0143 | 0.0058 ± 0.0021 | 69.3732 ± 63.7417 | 32.3869 ± 43.6101 |
| d | 0.2422 ± 0.0141 | 0.0325 ± 0.0042 | 7.5776 ± 1.0645 | 4.5330 ± 1.8245 |
| e | 0.2346 ± 0.014 | 0.0300 ± 0.0056 | 8.1367 ± 1.7966 | 4.9265 ± 2.1058 |
| f | 0.4061 ± 0.0103 | 0.2411 ± 0.0065 | 1.6859 ± 0.0629 | 1.3455 ± 0.1655 |

TABLE IV: Quantized metrics quantifying the performance of the reservoir architecture for the different signals shown in Table II.

## B. Multiple-seed experiments

For the multiple-seed experiments, only the ideal signal, the most distorted signal without chromatic dispersion and the signal with chromatic distortion are considered. Moreover, four different blocks of experiments trying different architectures have been carried out: one repeating the experiments from the single-seed experiments, one using all nodes to input signal into the reservoir, a block in which the recurrency is blocked, and the last block where fully random reservoirs with higher dimensions are evaluated. Every experiment is conducted 5 times with different intializations. Table V and Table VI summarize the results from this section. Heatmaps are omitted due to extension constraints.

| Exp | Metrics | | | | |
|---|---|---|---|---|---|
| | Error | Worst | Best | Ratio | Effective ratio |
| 1 | 0.1396 ± 0.1413 | 0.4547 ± 0.0168 | 0.0000 ± 0.0000 | inf | inf |
| 2 | 0.1487 ± 0.0546 | 0.2841 ± 0.0263 | 0.0250 ± 0.0026 | 11.5626 ± 2.0067 | 5.9940 ± 2.2673 |
| 3 | 0.3142 ± 0.0315 | 0.3952 ± 0.0146 | 0.2373 ± 0.0279 | 1.6842 ± 0.1707 | 1.3357 ± 0.1595 |
| 4 | 0.0934 ± 0.1026 | 0.2332 ± 0.1117 | 0.0000 ± 0.0000 | inf | inf |
| 5 | 0.1604 ± 0.0487 | 0.2547 ± 0.0386 | 0.0633 ± 0.0155 | 4.2519 ± 1.1479 | 2.6843 ± 1.0642 |
| 6 | 0.3366 ± 0.0316 | 0.4150 ± 0.0110 | 0.2453 ± 0.0240 | 1.7069 ± 0.1613 | 1.3833 ± 0.1720 |
| 7 | 0.0077 ± 0.0349 | 0.1205 ± 0.1114 | 0.0000 ± 0.0000 | inf | inf |
| 8 | 0.1399 ± 0.0587 | 0.2517 ± 0.0157 | 0.0216 ± 0.0016 | 11.7189 ± 1.2254 | 6.5182 ± 2.7904 |
| 9 | 0.3564 ± 0.0207 | 0.4252 ± 0.0079 | 0.3005 ± 0.0070 | 1.4163 ± 0.0531 | 1.1867 ± 0.0747 |
| 10 | 0.0002 ± 0.0004 | - | - | - | - |
| 11 | 0.0775 ± 0.0198 | - | - | - | - |
| 12 | 0.2744 ± 0.0335 | - | - | - | - |
| 13 | 0.0131 ± 0.0201 | - | - | - | - |
| 14 | 0.0876 ± 0.0191 | - | - | - | - |
| 15 | 0.2788 ± 0.0144 | - | - | - | - |
| 16 | 0.0000 ± 0.0000 | - | - | - | - |
| 17 | 0.0331 ± 0.0096 | - | - | - | - |
| 18 | 0.1622 ± 0.0227 | - | - | - | - |
| 19 | 0.0002 ± 0.0004 | - | - | - | - |
| 20 | 0.0806 ± 0.0222 | - | - | - | - |
| 21 | 0.1953 ± 0.0345 | - | - | - | - |

TABLE V: Metrics from the multi-seed experiments.

| Exp | Quantized metrics | | | |
|---|---|---|---|---|
| | Worst | Best | Ratio | Effective ratio |
| 1 | 0.4102 ± 0.0269 | 0.0000 ± 0.0000 | inf | inf |
| 2 | 0.2414 ± 0.0193 | 0.0350 ± 0.0064 | 7.1055 ± 1.3003 | 4.4804 ± 1.7428 |
| 3 | 0.3742 ± 0.0166 | 0.2559 ± 0.0242 | 1.4721 ± 0.1219 | 1.2409 ± 0.1333 |
| 4 | 0.2137 ± 0.1077 | 0.0001 ± 0.0006 | inf | inf |
| 5 | 0.2320 ± 0.0373 | 0.0752 ± 0.0168 | 3.2060 ± 0.7609 | 2.2540 ± 0.7980 |
| 6 | 0.3943 ± 0.0146 | 0.2648 ± 0.0231 | 1.5004 ± 0.1442 | 1.2875 ± 0.1512 |
| 7 | 0.0803 ± 0.1089 | 0.0000 ± 0.0000 | inf | inf |
| 8 | 0.2326 ± 0.0211 | 0.0289 ± 0.0049 | 8.2787 ± 1.5627 | 5.0926 ± 2.2014 |
| 9 | 0.4013 ± 0.0111 | 0.3130 ± 0.0082 | 1.2832 ± 0.0553 | 1.1432 ± 0.0696 |

TABLE VI: Quantized metrics from the multi-seed experiments.

In block 1, we confirmed the conclusions from the single-seed experiments. Specifically, the ideal case achieved both the best and worst error values across all experiments, consistent with previous findings. The introduction of amplifier noise and non-linearities in the second experiment resulted in more stable performance, with reduced variability compared to the ideal case. This makes the setup more suitable for fully random reservoirs and non-volatile phase shifters. The third experiment, which included chromatic dispersion, reaffirmed that the system lacks the necessary complexity and memory to compute the XOR task, as indicated by consistently high error values. Overall, while the gains and average gains were lower than those observed in single-seed experiments, the results still justify the use of tunable parameters in reservoir circuits. Moreover, the importance of adding extra complexity to the network, which enhances the circuit's performance, was also demonstrated, consistent with the single-seed experiments. Finally, the suitability of non-volatile phase shifters for this task was shown, enabling the creation of reservoirs with low power consumption.

In block 2, we aimed to determine the optimal input configuration by comparing the use of all four nodes against just two nodes (0 and 1). Experiment 4, which used an ideal input signal, demonstrated that the four-node configuration produced better results in terms of every metric and quantized metric compared to the two-node setup in block 1. Specifically, the average error and worst-case scenarios were significantly improved, indicating more consistent behavior. The optimal values and ratios between metrics and quantized metrics were also similar, reinforcing the tunable non-volatile reservoir idea.

However, in experiment 5, which introduced amplifier noise and high-power non-linearities, the average error increased, and the lowest error values were higher than in the previous setup, indicating a drop in overall performance. Despite this, the quantized metrics remained consistent with the regular ones.

In experiment 6, which included chromatic dispersion, all metrics worsened compared to the two-node setup, highlighting the system's lack of complexity to compute the XOR task with this type of data. Again, the quantized metrics provided results similar to the regular metrics, showing that they remain reliable even under less optimal conditions.

In block 3, we explored the impact of removing recurrency from the circuit, limiting signal propagation to just three cycles by blocking the feedback loop at node 2. The goal was to determine whether the additional interactions from previous signals improve the model's performance.

In experiment 7, which used an ideal input signal, the results significantly outperformed those from previous blocks, showing extremely low error and consistent behavior across both regular and quantized metrics.

Experiment 8, which introduced amplifier noise and high-power non-linearities, also showed better overall performance compared to earlier setups. Although the improvement wasn't as dramatic as in the ideal case, it was still notable, especially in terms of maximum and average gain (both ratio and effective ratio). The role of phase shifters, both regular and non-volatile, became more crucial in this scenario.

However, experiment 9, which involved chromatic dispersion, yielded the worst performance across all circuits tested, aligning with the qualitative analysis. The lack of sufficient memory in the no-recurrent setup meant that the circuit couldn't handle the expanded pulse information from the distorted signal, leading to poor results.

In block 4, we compared the performance of the 2x2 tunable reservoir circuit against higher complexity configurations, specifically 2x4 and 4x4 reservoirs. The goal was to determine whether the smaller 2x2 circuit could maintain performance levels comparable to larger reservoirs.

The results indicated that, for the 2x4 reservoir, the error values for all types of signals were worse than those of the 2x2 reservoir, regardless of whether regular or non-volatile phase shifters were used. When examining the 4x4 reservoirs, the experiment involving chromatic dispersion produced the lowest error among all setups. However, for the other two types of input signals, the 4x4 reservoir did not outperform the 2x2 setup, similar to the results seen with the 2x4 reservoir.

These findings are promising, suggesting that, at least in simulations for this case, it is possible to reduce the circuit size by half without sacrificing performance. In

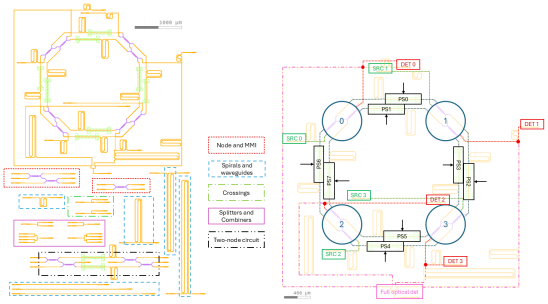


(a) (b)

Fig. 8: (a) Design of the full chip, with the different test devices highlighted. (b) Layout design of the complete reservoir circuit, with logical analog of the geometrical components on top of it.

some cases, a reduction to a quarter of the original circuit size might even be achievable.

## VI. Design and fabrication

Simulations provide a good overview of the circuit's general behavior, but real-world device responses often differ from theoretical predictions. Therefore, the 2x2 reservoir circuit has been fabricated to test its performance. Figure 8a shows the designed layout, while Figure 8b illustrates the reservoir and its logical representation for component identification.

The fabrication process involves five blocks: The first block, deep etching (200 nm), was performed using electron beam lithography (EBL) and reactive ion etching (RIE). The second block, shallow etching (70 nm), used a similar process. The third block involved planarizing the chip with silicon oxide deposition followed by RIE. In the fourth block, materials related to the EO effect, lanthanide and PZT, were deposited via spin coating and annealing. Lastly, Ti/Au metal contacts for the phase shifters were deposited using a lift-off process, which included photolithography for photoresist patterning, e-beam evaporation for metal deposition, and removal of excess material along with the photoresist.

## VII. Conclusions

In this work, a tunable 2x2 spatially distributed reservoir architecture was studied, featuring 3x3 multi-mode node structures, phase shifters in the interconnections, and an electrical readout. The aim was to analyze the dynamics with phase shifters and evaluate performance on an XOR logic operation with a generated input bitstream. Mathematical analysis showed that two nodes and phase shifters could solve the problem with an ideal signal.

Simulations included signals with various distortions to assess different real-world scenarios. The main setup consisted of a 2x2 reservoir with 3x3 MMIs as nodes, where only two nodes are used to input signal into the reservoir, and only two phase shifters placed in their interconnections are used as tunable parameters. Three reservoir variations were also tested: using all nodes to input signal, blocking circuit recurrence, and adding more nodes. The former produced both better and worse results compared to the vanilla case, so we cannot confirm if it improves performance. The non-recurrent setup showed the best performance, though no configuration handled chromatic dispersion effectively. Tunable reservoirs matched or outperformed higher-dimensional ones without phase shifters. Non-volatile phase shifters were comparable to continuous ones. In general, the presence of high-error phase shifter configurations in all setups underscored the need for tunable parameters.

Fabrication encountered misalignment issues, leaving measurements for future work. Overall, the promising results suggest further exploration of tunable reservoirs.

## References


[1] I. T. Union. (2023) Facts and figures 2023 - internet traffic. [Online; accessed 16-05-2024]. [Online]. Available: https://www.itu.int/itu-d/reports/statistics/2023/10/10/ff23-internet-traffic/.

[2] P. Glauner, P. Plugmann, and G. Lerzynski, Digitalization in healthcare. Springer, 2021.

[3] R. Hassan, F. Qamar, M. K. Hasan, A. H. M. Aman, and A. S. Ahmed, "Internet of things and its applications: A comprehensive survey," Symmetry, vol. 12, no. 10, p. 1674, 2020.

[4] D. Haileselassie Hagos, R. Battle, and D. B. Rawat, "Recent advances in generative ai and large language models: Current status, challenges, and perspectives," arXiv e-prints, pp. arXiv–2407, 2024.

[5] C. Architecture and P. Group, "The death of moore's law: What it means and what might fill the gap going forward," 2024, [Online; accessed 16-05-2024]. [Online]. Available: https://cap.csail.mit.edu/death-moores- law-what-it-means-and-what-might-fill-gap-going-forward.

[6] A. B. Abdallah and K. N. Dang, Neuromorphic computing principles and organization. Springer, 2022.

[7] G. Van der Sande, D. Brunner, and M. C. Soriano, "Advances in photonic reservoir computing," Nanophotonics, vol. 6, no. 3, pp. 561–576, 2017.

[8] K. Vandoorne, W. Dierckx, B. Schrauwen, D. Verstraeten, R. Baets, P. Bienstman, and J. Van Campenhout, "To- ward optical signal processing using photonic reservoir computing," Optics express, vol. 16, no. 15, pp. 11 182– 11 192, 2008.

[9] K. Vandoorne, P. Mechet, T. Van Vaerenbergh, M. Fiers, G. Morthier, D. Verstraeten, B. Schrauwen, J. Dambre, and P. Bienstman, "Experimental demonstration of reservoir computing on a silicon photonics chip," Nature communications, vol. 5, no. 1, p. 3541, 2014.

[10] A. Katumba, J. Heyvaert, B. Schneider, S. Uvin, J. Dambre, and P. Bienstman, "Low-loss photonic reservoir computing with multimode photonic integrated circuits," Scientific reports, vol. 8, no. 1, p. 2653, 2018.

[11] I. Bauwensa, K. Harkhoea, E. Gooskensb, P. Bienstmanb, G. Verschaffelta, and G. Van der Sandea, "Increasing the nonlinear computational capacity of a spatial photonic reservoir computing system," in Proceedings of SPIE. SPIE, 2024.

[12] C. Ma, J. Van Kerrebrouck, H. Deng, S. Sackesyn, E. Gooskens, B. Bai, J. Dambre, and P. Bienstman, "Integrated photonic reservoir computing with an all-optical readout," Optics Express, vol. 31, no. 21, pp. 34 843–34 854, 2023.

[13] S. Biasi, G. Donati, A. Lugnan, M. Mancinelli, E. Staffoli, and L. Pavesi, "Photonic neural networks based on integrated silicon microresonators," Intelligent Computing, vol. 3, p. 0067, 2024.

[14] R. Penrose, "A generalized inverse for matrices," in Mathematical proceedings of the Cambridge philosophical society, vol. 51, no. 3. Cambridge University Press, 1955, pp. 406–413.

**RESUMEN EJECUTIVO**

| CONCEPT (ABET) | CONCEPTO (traducción) | ¿Cumple? (S/N) | ¿Dónde? (páginas) |
|---|---|---|---|
| 1. IDENTIFY: | 1. IDENTIFICAR: | | |
| 1.1. Problem statement and opportunity | 1.1. Planteamiento del problema y oportunidad | S | 1-9 |
| 1.2. Constraints (standards, codes, needs, requirements & specifications) | 1.2. Toma en consideración de los condicionantes (normas técnicas y regulación, necesidades, requisitos y especificaciones) | N | |
| 1.3. Setting of goals | 1.3. Establecimiento de objetivos | S | 9-10 |
| 2. FORMULATE: | 2. FORMULAR: | | |
| 2.1. Creative solution generation (analysis) | 2.1. Generación de soluciones creativas (análisis) | S | 25-41 |
| 2.2. Evaluation of multiple solutions and decision-making (synthesis) | 2.2. Evaluación de múltiples soluciones y toma de decisiones (síntesis) | S | 42-74 |
| 3. SOLVE: | 3. RESOLVER: | | |
| 3.1. Fulfilment of goals | 3.1. Evaluación del cumplimiento de objetivos | S | 92-93 |
| 3.2. Overall impact and significance (contributions and practical recommendations) | 3.2. Evaluación del impacto global y alcance (contribuciones y recomendaciones prácticas) | S | 93-94 |

# Contents

# List of Figures

# List of Tables

# 1

# Introduction

## 1.1 Motivation

The digital revolution has led to an exponential increase in internet traffic over the past few years. This is mainly due to businesses and individuals increasingly relying on the internet for a wide variety of activities, especially after the Covid-19 pandemic. Examples of these activities include the deployment of IoT applications, which currently involves the connection of billions of devices [5], and the digitalization of industries like healthcare [6], finance [7] or commerce [8], among others. As a result, the demand for data transmission has skyrocketed. This trend is clearly illustrated in the International Telecommunication Union's 2023 report on data traffic statistics [1]. The report shows a steady increase in both mobile and fixed broadband traffic, as depicted in Figure 1.1.

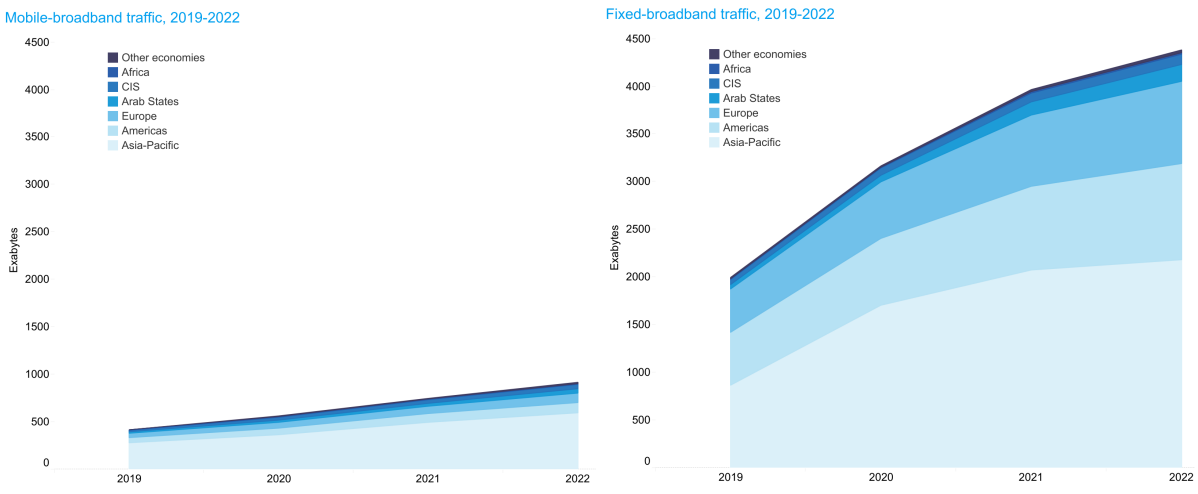


(a) (b)

Figure 1.1: Data traffic trends according to the International Telecommunication Union's 2023 report. [1]

Consequently, huge amounts of data are generated, transmitted and processed every day, requiring significant computational power to manage the increasing data traffic. Additionally, the rise of AI-based applications, par-

ticularly those utilizing large generative models, is further rising the demand for computational resources [9]. This situation highlights the need for efficient computing techniques that can handle this data influx while also reducing power consumption.

Traditional computation techniques and hardware architectures are increasingly proving inadequate to handle the escalating computational demand. For instance, in the realm of electronics, many experts assert that Moore's law, which has long dictated the pace of technological advancement, is nearing its end [2]. Therefore, to achieve greater capabilities, the fabrication of larger and more power-intensive devices would be necessary. However, this could have a detrimental impact on the environment. In response to this increasing demand, new types of computational architectures and technologies beyond Von Neumann architecture are emerging to meet these needs [10, 11, 12, 13, 14, 15].

## 1.2 Neuromorphic computing

The human brain is a highly efficient analog system capable of performing multiple tasks simultaneously (e. g. speaking and walking while mantaining the vital signs) and with very low energy consumption [16]. For this reason, it has often been used as a source of inspiration for the design of computing techniques to further improve the capabilities of traditional digital systems, which face challenges related to power density and clock frequency. Our brain operates entirely differently compared to von Neumann architectures, distributing computation and memory across more than 100 billion biological neurons, each connected to thousands of others via synapses (structure that enables communication between neurons) and communicating through spikes (short electrical pulses). These neurons only send a signal when a membrane potential reaches a specific value. Moreover, neurons and their interconnections are continuously being adjusted to learn how to respond to different input stimuli, which could be understood as biological reconfigurable circuits [3].

Neuromorphic computing is an emerging paradigm that seeks to mimic the brain's structure and operation using artificial neurons and synapses to solve machine learning problems [3]. By leveraging principles from neuroscience, these systems achieve efficiency while consuming minimal power.

An example of neuromorphic circuits are traditional artificial neural networks (ANNs) [17]. These networks partly emulate the structure of the brain by implementing artificial neurons that combine signals from other neurons in their neighborhood through adjustable weighted sums and then apply a nonlinear transformation to introduce additional complexity to the circuit. The neurons are arranged in layers, with each neuron connected only to neurons in adjacent layers, ensuring that information flows in one direction, from earlier to later layers. However,

unlike biological neurons, these neurons always fire an output signal whenever an input signal is received.

## 1.3 Reservoir computing

Typical feed-forward neural networks, such as ANNs, are widely used for non-temporal problems. In feed-forward networks, information flows in one direction without any cycles or loops. This static nature makes them well comprehended and effective for problems where the input data is independent of time. However, this characteristic also restricts their ability to handle time-varying signals.

On the other hand, recurrent neural networks (RNNs) introduce feedback loops, allowing information to be fed back into the network, creating a form of internal memory. This memory enables RNNs to identify and process time correlations in sequential data, making them suitable for temporal problems. However, this feedback mechanism complicates the learning process, posing challenges in establishing a universal learning rule—a method used to train the neural network to perform specific tasks. Consequently, different rules have been developed for various tasks and topologies, thereby constraining their widespread applicability[18, 19].

To overcome this problem, Jaeger [20] and Maass et al. [21] introduced the concepts of Echo State Networks (ESN) and Liquid State Machines (LSM), respectively. These two models follow the same principle: inspired by the way neurons in the human brain are connected, they utilize a system with non-linear dynamics and high interconnection complexity that transforms the input to a higher dimensional space. This could be seen as an RNN with fixed weights in the interconnections between neurons and its internal state continuously changing over time. Following this mapping process, a simple readout layer is employed to extract the state of the reservoir and trained to produce the desired output, typically in the form of a linear regression. Theoretically, if the non-linear system is sufficiently complex, this structure should be capable of performing any computation. The evolution of this kind of architectures is what is known nowadays as Reservoir Computing (RC). A schematic illustration can be seen in figure 1.2

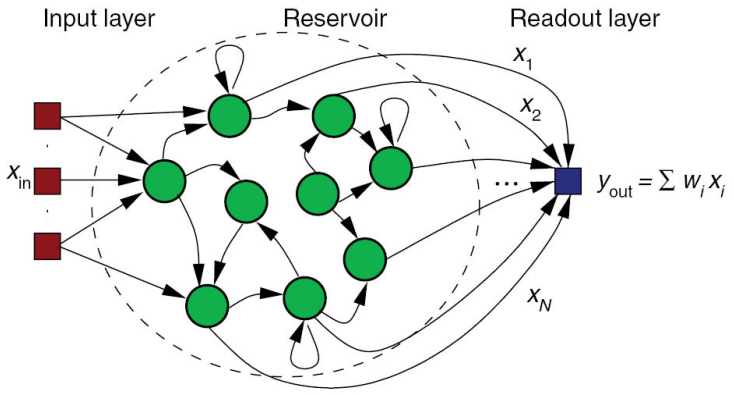


Figure 1.2: Reservoir computing architecture [4].

These architectures can be trained without requiring gradient optimization techniques, so the optimization process is efficient and fast. As it was mentioned before, the mapping to the non-linear system can be considered as a fixed RNN and thus, a training-free procedure. Regarding the readout stage, in this higher-dimensional space, a problem that originally required complex non-linear functions, becomes a linear problem that can be trivially solved. A representation of this concept is depcited in figure 1.3.

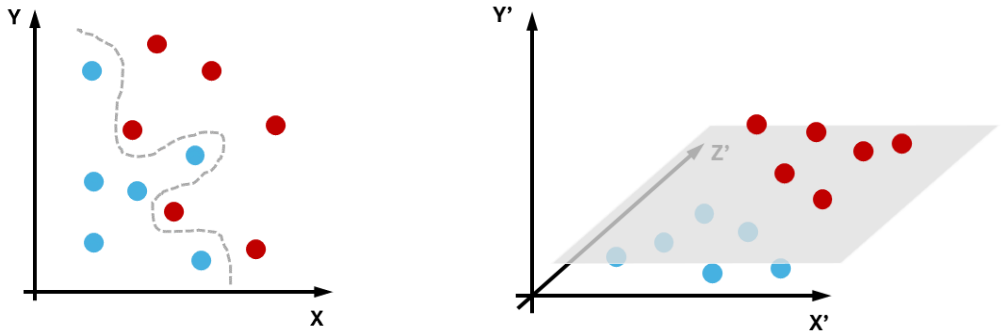


(a) (b)

Figure 1.3: Representation of how mapping to a higher dimensional space, from (a) to (b), turns a complex problem into a simple problem.

This allows the RC approach to achieve faster computational times with less parameter tuning compared to deep learning models, which rely on local optimization procedures. Applications of RC circuits are quite diverse and have demonstrated to be impactful in many fields of study such as signal classification, time series prediction, control of system dynamics and partial differential equations computation. In [22], M. Yan et. alia describe in detail the contributions performed by RC systems to such areas. Furthermore, their gradient-free optimization feature makes them perfectly suited for implementation in physical systems where tracking gradients can be challenging.

## 1.4 Photonic Neuromorphic Circuits and Reservoir Computing

Photonic Integrated Circuits (PICs) are advanced technology platforms that integrate multiple photonic components onto a single chip, enabling compact, high-performance optical systems. By consolidating functions such as light generation, modulation, and detection, PICs offer significant advantages in speed, energy efficiency, and miniaturization over traditional electronic systems [23]. These integrated circuits facilitate complex optical processes with reduced power consumption and enhanced reliability, making them crucial for applications in telecommunications [24], data processing [25], and sensing [26].

Photonic neuromorphic circuits combine the speed and efficiency of photonics with neuromorphic computing principles, enabling high-speed, low-energy calculations. While PICs are still in development and face challenges like

fabrication defects and simulation inaccuracies, neuromorphic architectures remains viable, specially reservoir computing schemes. Here, the PIC often acts as the static nonlinear system (the reservoir), meeting key requirements such as stationarity and nonlinear mapping, while the readout stage is performed in the electrical domain. The inherent randomness and fixed connectivity of reservoirs align well with current PIC technology, which is why reservoir computing is often implemented using PICs.

## 1.5 Literature Review

Various approaches have been explored for implementing photonic neuromorphic circuits across a wide range of tasks. Most of the works in this area could be categorized into two groups: spatially distributed reservoir circuits and reservoirs with delayed feedback loops. The former is a particularly popular approach, known for its intuitive implementation and versatility in topology configuration [4, 27]. The concept was first introduced in [19], marking the initial proposal of a photonic on-chip implementation for signal processing tasks using reservoir computing. In their work, the authors employed an architecture consisting of cascaded semiconductor optical amplifiers (SOAs) with splitters and combiners, both in feed-forward and back-looped configurations. Their objective was to perform a non-trivial classification task—specifically, distinguishing between rectangular and triangular signals by combining the weighted output from each SOA. Simulation experiments showed promising results, making this work the first step in photonic reservoir computing.

In a subsequent work, Vandoorne et. al proposed the "swirl" architecture [28]. This topology, depicted in figure 1.4, features a closed network of 4x4 nodes. The swirl configuration allows a richer mix of signals, especially in the central nodes. In a speech recognition benchmark task involving the classification of isolated spoken digits, the authors found that optimizing interconnection delay and phase shift between nodes could lead to better performance than traditional tanh reservoirs. However, these results were obtained through simulation.

The first experimental demonstration of reservoir computing on a SOI photonic chip was conducted by Vandoorne et. al in [29]. In this case, they used a completely passive swirl topology in which they dispensed with the use of SOAs. By processing the resulting output of each node after a certain delay via linear regression, they evaluated the architecture's performance in boolean operations, header recognition, and isolated digit speech recognition tasks. Notably, achieving a good performance hinged on the ratio of interconnection delay to bit delay, as illustrated in Figure 1.4. This implies that it would be feasible to speed up the signal up to 100Gbps, as requiring a ratio of 0.5 needs a delay of 50 ps (corresponding to a waveguide length of around 0.5 mm), which can be easily achieved.

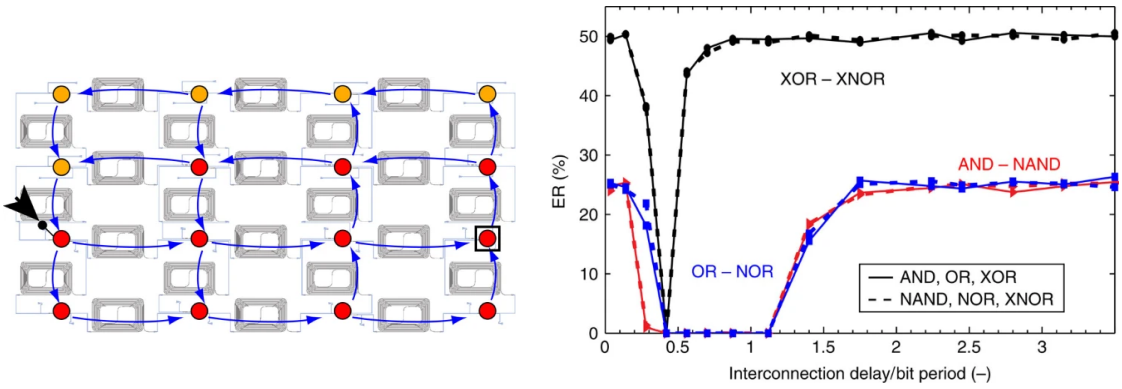


(a) (b)

Figure 1.4: (a) Passive 4x4 swirl topology [29]. (b) Error rate with respect to the interconnection delay of the architecture in (a) for various logic operations [29].

This architecture was further enhanced by introducing the "Four-port architecture," as presented in [30]. The 2x1 combiners used in the swirl topology exhibit intrinsic radiation losses due to their non-symmetric reciprocal nature. In contrast, the four-port topology utilizes 2x2 nodes, which do not have inherent losses. Additionally, increasing the number of interconnections improves the richness of the dynamics. An experimental demonstration was performed by Sckesyn et al. in [31, 32]. A 32-node four-port reservoir like the one shown in Figure 1.5 was used to perform signal equalization in presence of both linear and nonlinear distorsion. In all the conducted trials, the reservoir approach outperformed the Tapped Delay Line (TPL), a traditional equalization technique used as comparison, keeping the BER under $10^{-3}$ in every case, as illustrated in Figure 1.6.

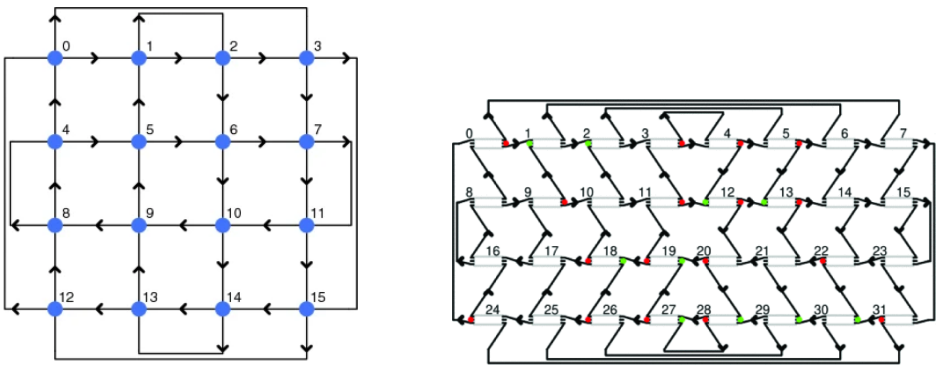

(a) (b)

Figure 1.5: Four-port architecture. In (a), the concept of the topology is depicted [30]. In (b), the specific implementation for the nonlinear fiber distorsion compensation is shown [31].

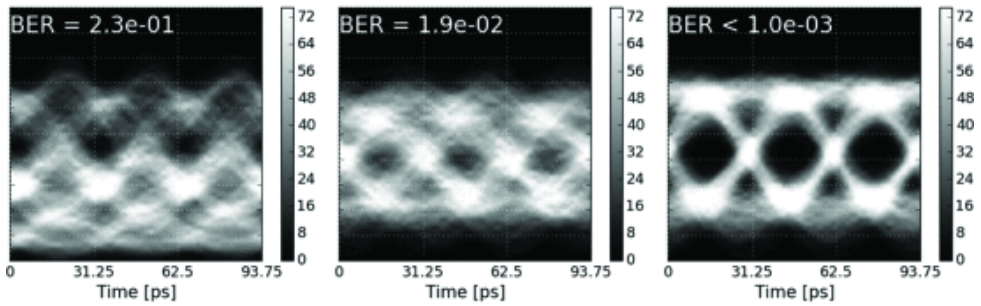


Figure 1.6: Results of the experiments from the architecture depicted in Figure 1.5. From left to right, the images correspond to the eye diagram of the signal without processing, with TPL and with the reservoir. [31]

In another attempt to mitigate radiation losses from combiners, the authors in [33] proposed using multimodal Y junctions as nodes. They optimized this component to maximize adiabaticity, thereby capturing more radiation in higher-order modes. Additionally, this multimodality enhances the reservoir's dynamics, which is also desirable. Their results showed a significant efficiency increase to 61%, compared to the 50% efficiency of single-mode junctions. This boost in efficiency, meaning reduced loss, allows signals to reach more distant nodes and persist longer within the reservoir dynamics, which is advantageous for scalability. They demonstrated improved performance by comparing multimodal and single-mode Y junctions in a 3-bit header recognition task through numerical and circuit simulations.

These types of reservoir circuits face limitations when designed compactly due to their short delay lines. In that case, rapid input and readout processes are demanded to match the high reservoir computation rate, which can be impractical and costly. However, in [34], they demonstrated that employing a binary modulating mask on the input signal, they reduced the sampling rate requirements by a factor of 40, offering an approach to overcoming this limitation.

Additionally, when designing such architectures, a crucial consideration is the selection of nodes to receive the input signal. A study detailed in [35] optimized a 16-node reservoir circuit, finding that utilizing all nodes as signal inputs enhances both performance and power efficiency. This fully connected approach harnesses richer internal dynamics and enables prolonged signal retention.

Choosing the appropriate operating point of the reservoir by tuning the system parameters is crucial for maximizing performance in complex tasks. In [36], it was demonstrated that setting a fixed point at the edge of stability increased the system's complexity, thereby enhancing the model's nonlinear computational capabilities.

Another intriguing approach involves implementing an all-optical readout scheme in the reservoir circuit. By maintaining the process entirely within the optical domain and avoiding optoelectronic conversions, the system leverages the inherent advantages of photonic platforms, including high-speed operation, minimal time delay, and reduced power consumption. Such system was proposed by M. Chonghuai et at. in [37]. The study

utilized heater-based Mach-Zehnder Interferometers (MZIs) as weighting elements, with the potential for significant power consumption reductions by using non-volatile materials like barium titanate (BTO). Experimental results showed that the system could successfully solve tasks like header recognition and the XOR task with low error rates. The real-time prediction signals closely matched the target signals, and the training process revealed how the network learned and adapted to recognize patterns. With its high-speed processing capabilities at a 20 Gbps bit rate, the system has significant potential for real-time data analysis and processing applications

Recently, in order to improve the dynamics and memory of these passive node-based architectures, the inclusion of external optical feedback was proposed in [38]. In this approach, the feedback is achieved with a single semiconductor laser, which is fed by the output of one of the nodes, and the amplified signal is reinserted into the reservoir, combined with the actual input signal. Numerical simulations demonstrate that this method significantly enhances the nonlinear computational capabilities, potentially improving performance in complex benchmark tasks.

In this context, silicon microring resonators (MRRs) are also of significant interest due to their non-linearities, rich dynamics, and memory capabilities, which can be exploited for reservoir computing [39]. Various topologies have been proposed, including the use of a single ring in an add-drop configuration as a compact reservoir with virtual nodes [40, 41]. This approach, first proposed by Appeltant et al. in [42], is considered a delay-based reservoir rather than a spatially distributed one.

To enhance the capabilities of MRR based reservoirs, some studies have included additional delay lines or utilized multiple microring resonators in spatial configurations. For instance, in [43], an external optical feedback was introduced to improve memory and provide a new degree of freedom in system dynamics control. Similarly, in [44, 45], a rainfall topology was used where each microring resonator input is fed by the drop port of the preceding ring. Feedback loops are incorporated to introduce recurrence and increase the network's memory, and the drop ports of the last column of microring resonators are used for readout.

There are also other MRR based reservoirs more similar to the ones discussed previously in this section, as it was presented in [46]. In this case, a 4x4 swirl topology configuration was proposed, where the microring resonators themselves serve as nodes, and the output signals for readout are extracted from the drop ports.

Another interesting approach consists of using nanophotonic crystal cavities to build the reservoir, as it was first proposed in [47]. In this work, the authors designed an architecture resembling that of artificial neural networks as they built layers of resonant cavities that provided for the required nonlinearities. They developed a training procedure and optimized the device to generate periodic complex-valued signals, outperforming the ESNs results.

More recently, a novel photonic crystal cavity design for reservoir computer on a silicon photonics chip was reported [48]. This new architecture exhibit exceptional mixing dynamics and was shown to have a memory up to 6 bits in header recognition tasks. The high-Q photonic crystal cavity ensures low losses, making the design also power efficient.

Free space optics has also been used to implement photonic spatially distributed reservoir computing schemes. For instance, in [45], the authors introduce and model a photonic system designed for rapid image identification using dispersive Fourier techniques. The system employs a photonic reservoir computing setup, utilizing the non-linear properties of randomly connected InGaAsP microring resonators. Trends in the most recent works combine the use of dispersive elements, non-linear nodes or scattering elements with arrays of light sources to generate the RNNs corresponding to the reservoir [49, 50, 51].

## 1.6 Objectives and outline

The goal of this project is to study, simulate, design, fabricate and measure a PIC that implements a tunnable spatially distributed reservoir computing architecture with an electrical readout using Silicon on Insulator (SOI) technology. This tunnability is achieved with phase shifters placed in the interconnections between nodes. In principle, being able to modify the circuit dynamics should improve the performance of the system compared to its fixed counterpart, so this project aims to characterize and quantify such improvement. To conduct this, the following secondary objectives have been pursued:

- Choose a proper problem that allows to test the performance of the system.
- Find the optimal dimensions of the reservoir, the type of nodes and the number and location of phase shifters for this specific problem.
- Study mathematically the performance of the reservoir for the chosen reservoir configuration.
- Generate the input and target signals needed to train and evaluate the system during simulations. Different types of distorsions in the input signals are desired to prove the reliability of the circuit.
- Simulate the chosen reservoir architecture using such self-generated signals, train the readout to extract the reservoir state, evaluate the results and compare them to higher-dimension reservoir architectures.
- Study the performance of the circuit when non-volatile phase shifters are used instead of regular phase shifters.
- Design the layout of the reservoir architecture for the optimal configuration.
- Fabricate the layout chip that has been designed.
- Carry out measurements on the actual chip to compare the real performance to the results obtained in the simulations.

The rest of the thesis is structured as follows: Chapter 2 provides an overview of the main concepts related to the project and their background. In Chapter 3, the problem is formulated, and a theoretical approach to solving it is

presented. This includes the optimal reservoir configuration, detailing both the dimensions and the number and arrangement of the phase shifters, as well as a comprehensive study of its behaviour, all described using mathematical formalisms. Chapter 4 covers the simulations of the reservoir and the training of the readout across various scenarios. It includes the generation of input and target signals, the simulation and training processes themselves using these signals, and a discussion of the results. Chapter 5 presents the layout design corresponding to the circuit discussed in the theoretical analysis, examining each physical component and matching it to its logical counterpart. Chapter 6 details the steps followed during the fabrication process. Finally, Chapter 7 presents the conclusions and key insights gained during the thesis, along with suggestions for future research directions.

# 2

# Theoretical framework

This chapter provides a comprehensive account of the theory needed to understand the main concepts used throughout this project. It covers the basics of the physical properties leveraged in the circuit design to create the tunable reservoir, the characteristics of the most important materials used for this purpose, the working principle of the components used in the system, the mathematical definition of reservoir computing itself, and the different distortions that could be encountered in non-ideal signals.

## 2.1 Phase shifters

### 2.1.1 Phase modulation with linear electro-optic effect

Modulation is defined as the variation of the physical properties of a wave, such as intensity, phase, frequency or polarization. In optics, there are two primary approaches to achieve modulation of an optical signal: direct modulation and external modulation. Direct modulation involves modulating the electrical source of the optical signal itself, i. e. the injection current. This technique permits easy and fast deployments but provokes the modulated signals to have chirp (continuous drift of phase and/or frequency), so they are mostly used in short range optical links. Alternatively, external modulation uses an optical modulator to alter the properties of light waves, which overcomes this problem. Electro-absorption (EA), electro-optic (EO), magneto-optic (MO), thermo-optic (TO) and acousto-optic (AO) effects are typical phenomena leveraged to create external modulators [52]. In this project, only EO effects have been used for modulation, so just further insights about this technology are provided in the following.

The EO effect involves the modification of a material's optical properties in the presence of an electric field that varies slowly compared to the frequency of light. Specifically, it enables phase modulation by modifying the refractive index of such material. A significant advantage of this technique is that this effect do not involve an absorption process, so there are no intrinsic losses during the modulation process. Several field effects that can implement this phenomena include plasma dispersion effect, Pockels effect, Kerr effect, Franz-Keldysh effect (FKE) and quantum-confined stark effect (QCSE) [53]. In order not to extend the explanation unnecessarily, only

those effects that intervene directly in our chip will be explained which, in this case, is the Pockels effect. Kerr effect is also happening but in presence of the Pockels effect can be considered negligible.

The Pockels effect, also known as the linear electro-optic effect, occurs when an electric field induces a change in the refractive index of a non-centrosymmetric crystal, meaning a crystal that lacks inversion symmetry [54]. According to Neumann's principle, the physical properties of a material must remain invariant under the symmetry operations of its point group. In centrosymmetric materials, where inversion symmetry is present, the Pockels effect is absent because the second-order nonlinearity is canceled out; the inversion symmetry forces the corresponding electro-optic tensor components to be zero. As a result, the Pockels effect only manifests in non-centrosymmetric materials, where this symmetry is broken, allowing non-zero electro-optic coefficients [54]. When the Pockels effect is present, it manifests as a change in the material's refractive index proportional to the applied static electric field:

$$\Delta \frac{1}{n_i^2} = \sum_j r_{ij} E_j + \text{Higher order EO effects} \tag{2.1}$$

In this equation, $n_i$ (where i=1,2,3) represents the refractive indices corresponding to the x, y and z components of the electric field, $E_j$ (where i=1,2,3) denotes the x, y and z directions of the applied electric field and $r_{ij}$ are known as the EO coefficients, which quantify the effect of the electric field on the optical properties along specific axes. As an example, the coefficient $r_{31}$ represents how much an electric field applied in the x direction affects the refractive index in the z direction [52]. It can be observed in the expression above that the Pockels coefficients are proportional to the electric field, indicating a linear dependence. Moreover, the third-order nonlinearity, which is part of the higher-order effects, corresponds to the Kerr effect. The magnitude of the Pockels effect is typically around $10^{-12} m V^{-1}$, while the Kerr effect has a magnitude of aprproximately $10^{-15} m^2 V^{-2}$. Therefore, Kerr effect, along with the rest higher-order terms, are often considered negligible when Pockels effect is present [54].

However, the linear electro-optic effect cannot be directly implemented on SOI substrates, as silicon is centrosymmetric unless its crystal symmetry is intentionally broken [55]. Alternatively, plasma dispersion effects can be leveraged or EO materials compatible with the SOI platform can be deposited on top to enable modulation. In this project, the latter approach was chosen, with lead zirconate titanate (PZT) selected as the EO material to act as the phase shifters that tune the reservoir dynamics.

### 2.1.2 Performance metrics for EO modulators

The figures of merit (FOMs) of a modulator are the key metrics that allow us to quantify and compare the performance of the device. In this project, no in-depth characterization of the modulators has been carried out, but certain FOMs have been used to evaluate the system capabilities. For EO modulators, which are the ones that have been implemented, the metrics typically used include:

1. Extinction ratio (ER). It measures the intensity difference between the "on" (maximum intensity) and "off" (minimum intensity) states of the modulated signal. This ratio is crucial for ensuring signal clarity and reducing bit error rates in long-distance communication, as well as for maintaining high receiver sensitivity.

$$ER = 10 \log(\frac{I_{max}}{I_{min}}) \tag{2.2}$$

   - $I_{max}$: Intensity of the optical signal in the "on" state.
   - $I_{min}$: Intensity of the optical signal in the "off" state.

2. Insertion loss (IL). It quantifies the optical power loss introduced by the modulator. It is defined as the logarithmic ratio of the input optical intensity to the maximum output optical intensity.

$$IL = 10 \log \frac{I_{max}}{I_0} \tag{2.3}$$

   - $I_0$: Intensity of the optical signal at the modulator input
   - $I_{max}$: Maximum intensity of the optial signal at the modulator output

3. Modulation efficiency. Modulation efficiency is a measure of how effectively the modulator converts an electrical signal into an optical phase shift. It is defined by the product of the voltage required to achieve a $\pi$ radian phase shift ($V_\pi$) and the length of the modulator ($L_\pi$). Lower values of $V_\pi L_\pi$ indicate higher modulation efficiency, meaning less voltage and/or shorter length is needed to achieve the desired phase shift.

4. Electro-optical bandwidth. The electro-optical bandwidth is the frequency range over which the modulator can effectively operate, typically defined as the frequency at which the optoelectronic response falls to -3 dB (or 50% of its maximum power). This bandwidth indicates how quickly the modulator can respond to electrical signals without significant loss, directly influencing the data transmission rate.

5. Optical bandwidth. The optical bandwidth, also known as the spectral width, is the range of wavelengths over which the modulator can operate effectively. A broader optical bandwidth allows for more flexibility in the choice of operational wavelengths and can support wavelength-division multiplexing (WDM) systems.

6. Maximum data rate. The maximum data rate, measured in bits per second (bits/s), is the highest rate at which the modulator can transmit data. It is determined by the modulator's bandwidth and its ability to switch between states rapidly.

7. Footprint size. The footprint size refers to the physical area occupied by the modulator on a chip. A smaller

footprint is advantageous for integrating multiple modulators into compact photonic circuits and reducing the overall size of optical systems.

8. Power consumption. The power consumption measures the energy utilized to generate the modulated signal.

### 2.1.3 Lead zirconate titanate (PZT)

As mentioned in Section 2.1.1, modulating signals propagating through silicon waveguides is not possible via the linear electro-optic effect due to silicon's point group symmetries. However, modulation can still be achieved through other approaches, such as heating or depositing a different material on top of the waveguide that couple part of the light and can be modulated. This is the approach we take in the project with PZT.

Lead zirconate titanate (PZT) is a ceramic compound with the chemical formula [56]:

$$Pb[Zr_xTi_{1-x}]O_3 \tag{2.4}$$

where

$$0 \leq x \leq 1 \tag{2.5}$$

PZT is notable for its remarkable piezoelectric [56] and electro-optic effects [57]. It exhibits a high refractive index ($\sim 2.4$) and a linear electro-optic effect ranging from 110 to 240 pm/V, particularly when deposited on silicon with an ultrathin lanthanide film (5 - 15 nm) [58]. This intermediate layer facilitates a highly textured and preferential (100) crystallographic orientation of the PZT, i.e. ensuring that the PZT crystals are aligned in a specific direction, which is crucial for displaying its electro-optic properties. Additionally, it prevents unwanted elements from the substrate from diffusing into the PZT layer, resulting in purer PZT films with improved structural properties, including density, uniformity, and crack-free, highly oriented layers.

Furthermore, PZT is known for its low loss and flat wavelength response for modulation purposes [58], making it an ideal candidate for silicon nanophotonics electro-optic modulators. In fact, authors in [59] first demonstrated a TE/TM Pockels modulator on a hybrid PZT/Si platform, specifically implementing a Mach-Zehnder modulator (MZM) with this technology. In subsequent work [60], they reported enhanced device capabilities, including an efficiency of $V_\pi L = 2Vcm$ and an in-plane effective Pockels coefficient of $\sim 225pm/V$. Subsequent studies [61, 62] have further validated this technology for electro-optic modulation, proving its reliability in various applications.

However, one might question why PZT is preferred for phase modulation over silicon modulators utilizing plasma dispersion effects or alternative materials with electro-optic properties, such as lithium niobate ($LiNbO_3$) [63],

organic compounds [64], or barium titanate (BTO) [65]. Plasma dispersion effect modulators can introduce unwanted amplitude modulation and often suffer from high insertion loss. Organic materials may suffer from stability issues, while integrating $LiNbO_3$ and BTO into systems requires costly bonding techniques. In contrast, PZT offers advantages that address these issues, making it a promising candidate for future reservoir implementations [60]. Moreover, PZT could potentially provide for a non-volatile electro-optic behaviour, so if demonstrated, it could be directly tested it in the designed circuit without having to fabricate a whole new device.

### 2.1.4 Non-volatile phase shifters

Having memory in any programmable computing system is essential for efficiently building complex models and architectures. Taking electronics as a reference, systems like computers depend on non-volatile technology to store programs, archives and operating systems, among others.

Although photonics could benefit from hybrid integration with electronic components that handle memory tasks, this approach would not solve all the challenges. For instance, using phase shifters in a neuromorphic architecture requires a constant voltage to maintain specific behavior. Even if the voltage value could be stored, it would still require continuous power consumption.

Achieving non-volatile components in the photonic domain would significantly enhance the efficiency of creating systems with this technology, taking programmable analog computing to the next level. This would greatly reduce electricity costs, opening up new opportunities to improve the sustainability of information systems across all domains.

Progress in this direction has already been made, as shown in [66]. Utilizing resonator structures, the authors demonstrate non-volatile phase shifting in ferroelectric BTO by stabilizing different ferroelectric domain configurations within the material. When an electric field is applied, the polarization of these domains, which are aligned along the c-axis, can be partially reversed, leading to a change in the effective Pockels coefficient. This change, in turn, alters the refractive index of the BTO layer. By applying short voltage pulses, the system can achieve and maintain various refractive index states, enabling stable non-volatile operation without the need for continuous power input. However, this non-volatility is limited by the physical properties of the material, making it challenging to achieve much more stable states. Additionally, the states have been shown to remain constant for a period of 10 hours, after which the phase shifters begin to alter their behavior. While this technology is still far from mature, it demonstrates promising progress in the field of photonic computing.

## 2.2 Waveguides

Waveguides are fundamental components in PICs that confine and guide light within a specified path on a chip. Their primary function is to channel optical signals from one point to another with minimal loss and distortion.

The working principle of waveguides relies on the phenomenon of total internal reflection. Light is confined within the waveguide due to a difference in refractive indices between the core and the surrounding cladding material. The core has a higher refractive index, ensuring that light traveling through it is reflected back into the core, thus maintaining the light within the waveguide structure.

Waveguides are designed with specific dimensions and materials to support a specific number modes of light propagation. The width, height, and refractive index of the waveguide core determine the supported modes and their confinement. By carefully engineering these parameters, waveguides can be optimized for different applications, such as signal routing, filtering, and modulation.

In this project, waveguides are fabricated using SOI technology and are designed to confine a single mode, with a geometry of 220 nm in height and 500 nm in width.

## 2.3 Grating couplers

Grating couplers are crucial components in photonic integrated circuits used to interface between optical fibers and on-chip waveguides. They function by converting guided light from a waveguide into free-space radiation or vice versa. This conversion is achieved through a periodic structure, known as a grating, which creates diffraction at specific angles to match the propagation modes of the waveguide and the fiber.

The design of grating couplers involves tuning the grating's periodicity, shape, and dimensions to achieve efficient coupling with minimal loss. Typically, the grating's periodicity determines the wavelength of light that is efficiently coupled, while the grating's geometry affects the coupling efficiency and direction. By optimizing these parameters, grating couplers can facilitate effective light transfer between photonic circuits and external optical components, ensuring seamless integration in photonic systems.

## 2.4 Multi mode interferometers

Multimode interferometers (MMIs) are crucial components in integrated photonics, used for functions such as splitting, combining, and routing optical signals. They operate by utilizing interference among multiple optical modes within a waveguide.

An MMI consists of a waveguide segment designed to support several modes, where light entering the device excites these modes. The modes interact and interfere within the multimode region, creating a specific distribution of light at the output ports. However, this distribution is just influenced by the phase difference caused by the different velocities of the modes, there is no exchange of energy between them. Thus, the output distribution is influenced by the dimensions of the MMI - determining the number of excited modes - and the effective indices of the modes. Figure 2.1 shows an example of multiple nodes being excited within an MMI.

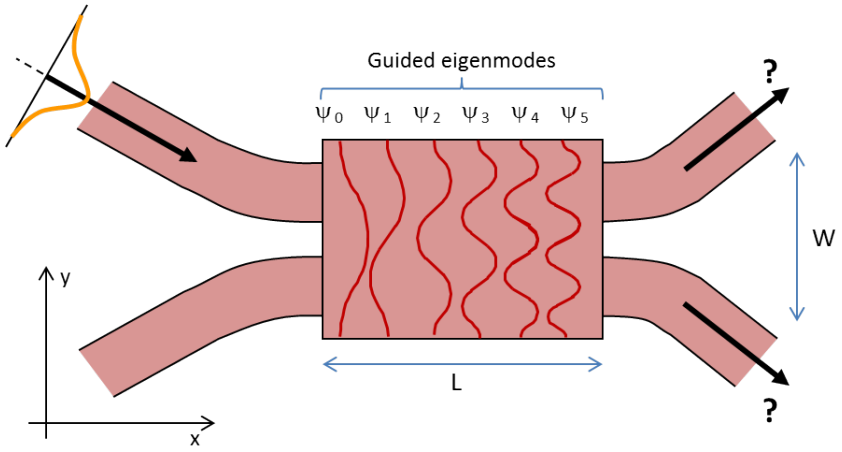


Figure 2.1: Modes excited in an MMI [67].

By carefully designing the MMI's length and waveguide dimensions, specific splitting ratios or combining efficiencies can be achieved. The ability to control these parameters allows MMIs to be customized for various photonic applications, making them versatile tools in optical circuit design. [67]

## 2.5 Photodetectors

Photodetectors are devices used in photonic integrated circuits to convert optical signals into electrical signals. They operate based on the photoelectric effect, where incoming photons are absorbed by a semiconductor material, generating electron-hole pairs. These charge carriers are then collected to produce an electrical current proportional to the intensity of the incoming light.

In this project, photodetectors are used to convert the reservoir state into the electrical domain, where the readout performs a linear combination of the reservoir signals to generate the desired output. Simulations employ a simplified ideal model, where detection is implemented by measuring the squared modulus of the light wave, which corresponds to its intensity. This method is known as direct detection.

## 2.6 Revisiting reservoir computing: training linear models

As mentioned in chapter 1, reservoir systems transform the input signal into a higher dimensional space, which can be expressed as $f : \mathbb{R}^l \rightarrow \mathbb{R}^k$ with $k > l$. Describing this architecture using the mathematical formalisms of recurrent neural networks results in two distinct expressions [27]: one representing the recurrent stage, corresponding to the reservoir where the static non-linear mapping occurs, and the other representing the readout stage, where the states are extracted and evaluated:

$$\begin{cases} x[n+1] = \sigma(W^{res}x[n] + W^{in}u[n]) \\ \hat{y}[n] = W^{out}x[n] \end{cases} \tag{2.6}$$

Here, $x[n] \in \mathbb{R}^k$ represents the reservoir states at discrete time $n$, $u[n] \in \mathbb{R}^l$ is the input to the reservoir, and $\hat{y}[n] \in \mathbb{R}^m$, is the output of the readout stage. The function $\sigma$ denotes the non-linearities within the reservoir. The matrices $W^{res} \in \mathbb{R}^{k \times k}$, $W^{in} \in \mathbb{R}^{k \times l}$ and $W^{out} \in \mathbb{R}^{m \times k}$ represent the weights between reservoir states, from the input signal to the reservoir, and from the reservoir the output as a readout stage, respectively.

To optimize the model for a specific task, the reservoir parameters $\sigma$,$W^{res}$ and $W^{in}$ are first determined and fixed. Then, given a training sequence that passes through the reservoir $X = \{x[1], x[2], \ldots, x[N]\}$, and a target output $Y = \{y[1], y[2], \ldots, y[N]\}$, also known as ground truth, the weights of the output matrix $W^{out}$ are tuned to minimize a cost function. A common choice is:

$$\begin{aligned} J(w) &= ||y - Xw||_2^2 + \beta||w||_2^2 = (y - Xw)^\intercal(y - Xw) + \beta w^\intercal w \\ w^* &= \underset{w}{\text{argmin}} J(w) \end{aligned} \tag{2.7}$$

Here, $w$ represents $W^{out}$ with a simplified notation, $w^*$ is the optimal value of $w$, and $\beta \in [0, 1]$ [22]. The cost function used in this context is the squared error with L2 regularization, which is a standard choice for linear regression tasks. The squared error term measures the discrepancy between the predicted and actual values, penalizing larger deviations more heavily. This ensures that the model's predictions closely match the observed data.

The L2 regularization, also known as Ridge regularization, adds a penalty proportional to the square of the magnitude of the model's coefficients. This helps prevent overfitting by discouraging the model from relying too heavily on any single feature, especially when dealing with high-dimensional data. By balancing the fit to the training data with the simplicity of the model, L2 regularization promotes a solution where the model generalizes better to unseen data, making it a robust choice in many linear regression scenarios.

Note that $J$ is a convex function meaning that for any two points $w_1$ and $w_2$ (with $w_1 \neq w_2$), and two arbitrary constants $\alpha, \beta \in \mathbb{R}$:

$$J(\alpha w_1 + \beta w_2) \leq \alpha J(w_1) + \beta J(w_2) \tag{2.8}$$

This implies that any other value of $J$ resulting from a linear combination of points $w_1$ and $w_2$, will lie on or below a straight line connecting these points. Therefore, the optimal value of $w$ is found when the left and right

sides are equal, meaning that no lower values exist; thus, the line connecting the points would be completely horizontal. In other words, an explicit solution can be found by applying $\frac{\partial J}{\partial w} = 0$ [16]. We can calculate $\frac{\partial J}{\partial w_i}$ as:

$$\frac{\partial J}{\partial w_i} = -2 \sum_{j}^{N} (y - x_j w) x_{ij} + 2\beta w_i \tag{2.9}$$

Now, defining $\frac{\partial J}{\partial w}$ as:

$$\nabla_w J = \begin{bmatrix} \frac{\partial J}{\partial w_0} \\ \frac{\partial J}{\partial w_1} \\ \vdots \\ \frac{\partial J}{\partial w_N} \end{bmatrix} \tag{2.10}$$

we can apply the condition for optimal $w$ as:

$$\nabla_w J = 2X^\intercal (Xw - Y) + 2\beta w = 0 \tag{2.11}$$

Finally, by rearranging the terms, we can derive the explicit solution:

$$w^* = (X^\intercal X + \beta I)^{-1} X^\intercal Y \tag{2.12}$$

This model is known as Ridge Regression or Tikhonov regularization, and its ridge estimator (or explicit solution) is obtained through the Moore-Penrose pseudo-inverse [68].

## 2.7 Signal distortions

This section aims to deepen into the theory behind the main distortions present in the reservoir input signals during the simulations, which have been carried out in Chapter 4. The transmission setup is comprissed by a laser as light source, a MZM, a 25 km fiber and a linear amplifier. However, since the modulation process is ideally implemented during the generation process, only the impact of the other devices is discussed.

### 2.7.1 Laser distortions

In lasers that generate one single frequency, both intensity and phase errors can be observed. These noises are mostly caused by two main sources of error: quantum effects and technological limitations [69, 70, 71]. On the

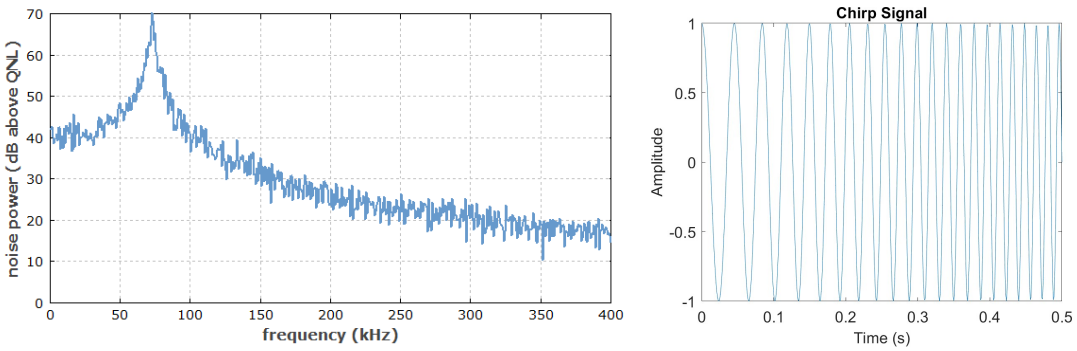


(a) (b)

Figure 2.2: (a) Intensity noise spectrum of a solid state laser [69]. (b) Example of a chirped signal generated by a laser.

one hand, the laser gain caused by spontaneous emission, and the resonator losses are quantum processes, with all that this implies. The accuracy with which these values can be predicted at every instant of time has a limit intrinsic to their quantum nature. On the other hand, vibrations, fluctuations of the pump source, temperature variations, etc. can also affect both intensity and phase. Additionally, it is also common to see coupling from intensity noise to phase noise, which limits the minimum linewidth that is achievable in single-frequency lasers [71].

It is important to note that, typically, phase noise caused by the aforementioned effects, translates into an almost continuus frequency drift rather than phase jumps because of the large number of particles involved in the process. Therefore, it could be considered as frequency noise (continuus variations of the instantaneous frequency). Figure 2.2 shows an example of these intensity and phase effects caused by a laser.

### 2.7.2 Amplifier distortions

The fluctuations found in phase-insensitive optical amplifiers like raman amplifiers show a similar behaviour as laser amplifiers, where the quantum effects and the technological limitations cause intensity and phase errors. Regarding the quantification of the intensity noise, a typical measure in this kind of amplifiers is the Noise Factor (F), which determines the amount of excess noise added by the it. This excess noise refers to the extra unwanted noise included by the amplifier, apart from the noise that was alredy present in the signal. The higher the input noise, the less relevant is the excess noise added by the amplifier. When the input noise is comparable to the excess loss, we can express F as:

$$S_{out} = FGS_{in} \tag{2.13}$$

where $S_{in}$ and $S_{out}$ are the intensity noise power spectral density at the input and output of the amplifier, respectively, and $G$, the amplification factor. The Noise Figure (NF) can then be defined as the 10 logarithm of

the F:

$$NF = 10 \log (F) \tag{2.14}$$

In optical amplifiers, the predominant source of noise factor is the shot noise. Shot noise is the random fluctuation in the signal due to the discrete nature of photons and electrons. It's an intrinsic property of light and becomes evident in detection and amplification processes. Therefore, a certain amount of this kind of noise is always present.

Phase-sensitive amplifiers like parametric amplifiers have not been considered during this study.

### 2.7.3 Fiber distortions

#### Absorption

To identify the noisy fluctuations added by the fiber, it is necessary to understand the main abosorption processes that take place during the propagation. Considering a silica waveguide, and not taking into account bend losses and discontinuities in the fiber (connectors, splices...), the two predominant loss mechanisms are the intrinsic absoprtion of the fiber and the Rayleigh scattering.

As it happened with the resonator loss, the quantum nature of the fiber abosorption process brings a certain amount of variability. However, in silica and for typical telecomunications wavelengths ($\lambda = 1.55\mu m$), this kind of absorption is very low, so the variability introduced might be low as well [72].

In this frequency range, the predominant source of loss is the Rayleigh scattering [72], as Figure 2.3 shows. The Rayleigh scattering is an elastic scattering (there is no transference of energy, i.e. the wavelength remains the same) that occurs when light propagates in a medium with defects or density fluctuations with much smaller size than the wavelength of light. The scattering particles or fluctuations are randomly placed along the fiber and the propagation described by the scattered light is different from the non-scattered, which can be translated into intensity and phase errors. Additionally, this effect is proportional to the fourth power of the inverse of the wavelength ($\propto \frac{1}{\lambda^4}$), so variations of the instantaneous frequency of the incoming signal might imply different scattering behaviours, again contributing to the intensity and phase fluctuations [73].

When the power of the input signal to an optical fiber is high, other scattering effects, such as Raman scattering and Brillouin scattering, become significant. These are inelastic processes, meaning they involve a change in wavelength. Raman scattering happens when light interacts with the vibrations of the material in the fiber, while Brillouin scattering occurs when light interacts with sound waves inside the fiber. Both types of scattering contribute to the intensity and phase noise of the signal, affecting the overall performance of the optical fiber communication system [73].

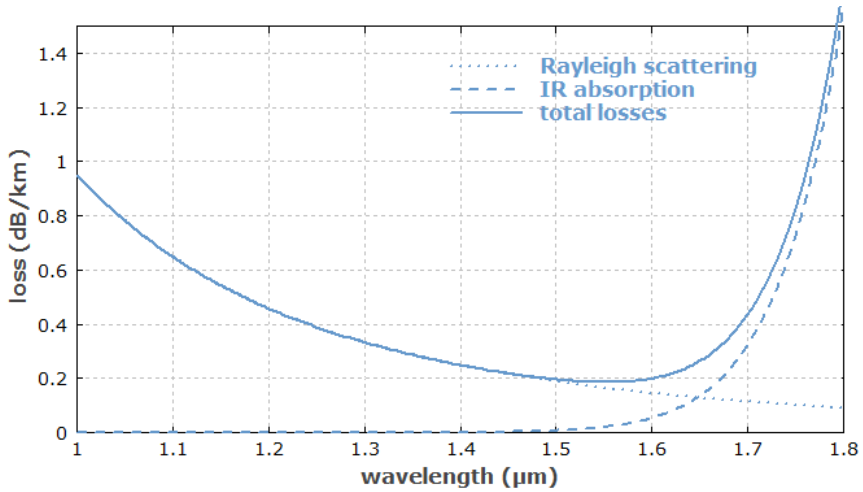


Figure 2.3: Loss contributions of near-infrared abosrption and scattering processes in glass silica optic fibers at telecom wavelengths [72].

#### Chromatic dispersion

Chromatic dispersion is a property of optical materials that causes different colors (or frequencies) of light to travel at different speeds through a medium. This effect occurs because the phase velocity (the speed of the light wave peaks) and the group velocity (the speed of the overall light pulse) vary with wavelength, leading to the material affecting each frequency differently. This dispersion causes two main issues: it spreads out a light pulse over time (pulse broadening), due to the variations in the group velocity, and introduces phase errors, caused by the different phase velocities.

We can describe chromatic dispersion using a mathematical expansion of the wave number $k(\omega)$ in terms of frequency $\omega$:

$$k(\omega) = k_0 + \frac{\partial k}{\partial \omega}(\omega - \omega_0) + \frac{1}{2}\frac{\partial^2 k}{\partial^2 \omega}(\omega - \omega_0)^2 + \dots \tag{2.15}$$

- The zeroth order term ($k_0$) represents a normal phase shift.
- The first-order term ($\frac{\partial k}{\partial \omega}$) is related to the inverse of the group velocity ($\frac{1}{v_g}$), indicating the delay of each frequency component.
- The second-order term ($\frac{\partial^2 k}{\partial^2 \omega}$) is known as group delay dispersion (GDD), which is measured in $s^2/m$. This term is primarily responsible for pulse broadening.

Higher-order dispersion effects become relevant with a broad optical spectrum, so they might not have a significant impact in our case of study. Regarding the pulse broadening effect, we can differentiate between two types:

- Normal Dispersion: Higher frequency components travel slower, resulting in a positive chirp (the pulse frequency increases over time).
- Anomalous Dispersion: Higher frequency components travel faster, resulting in a negative chirp.

Being able to find these two kinds of dispersive media allows for engineering combinations of fibers that compensate for each other's dispersion effects.

For the case of an ideal gaussian beam of duration $\tau_0$, the amount of resulting broadening considering only a second-order dispersion effect ($D_2$), can be quantified using the following expression:

$$\tau' = \tau_0 \sqrt{1 + (4ln2 \frac{D_2}{\tau_0^2})^2} \approx 4ln2 \frac{D_2}{\tau_0} \tag{2.16}$$

Additionally, although chromatic dispersion changes the phase of the light pulse components, it doesn't change the overall spectral shape (the power distribution across frequencies). However, if chromatic dispersion occurs along with optical nonlinearities (such as high-input power situations), it can indirectly affect the spectral shape by altering the pulse shape [74].

In our experiments, we only considered the chromatic dispersion caused by the optical fibers, as the dispersion introduced by the in-circuit waveguides was negligible in comparison.

#### Kerr effect

The Kerr effect is a nonlinear optical phenomenon that can happen when light travels through various materials like crystals, glasses, or even gases. It's basically a change in the material's refractive index caused by an electric field. There are two main types of Kerr effect: the Kerr Electro-optic Effect and the Optical Kerr Effect.

- Kerr Electro-optic Effect (DC Kerr Effect). This type of Kerr effect happens when a slowly changing electric field is applied to a material, like a piece of glass with electrodes on it. When light passes through this material, its phase changes depending on the electric field strength. This effect can even make a material that normally doesn't change the polarization of light (birefringence) do so. Essentially, the piece of glass can act like a waveplate (an adjustable optical device) controlled by electricity.
- Optical Kerr Effect (AC Kerr Effect). This version of the Kerr effect doesn't need an external electric field. Instead, it occurs due to the electric field of the light wave itself. When a high-intensity light beam travels through a material, it can change the refractive index of that material instantly. This change depends on the intensity of the light.

Hence, even with the absence of an external electric filed, the kerr effect still shows up in the optical fibers, especially for high intensity signals. This can cause unwanted effects like pulse broadening, positive and negative

chirping or self-phase modulation (change in the phase of the light beam itself, often leading to broadening of the pulse's spectrum), among others [75].

## 2.8 Coherence

Coherence is a crucial concept used in optical telecommunication systems. It refers to the existence of a fixed phase relation between different points of an optical wave, either in space or time. We call it partial coherence when this phase relation is not perfect but still holds with some variability; in this case, there is some degree of correlation. Figure 2.4 shows how this coherence is visualized for a laser Gaussian beam in different degrees [76].

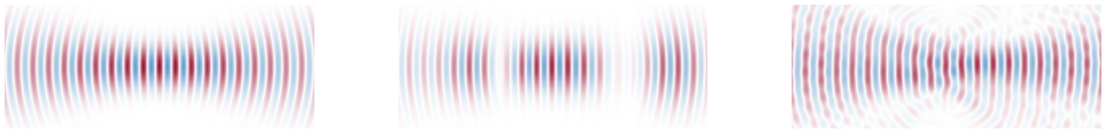

(a) (b) (c)

Figure 2.4: (a) Gaussian laser beam with both good temporal and spatial coherence. (b) Gaussian laser beam with poor temporal coherence and good spatial coherence. (c) Gaussian laser beam with good temporal coherence and poor spatial coherence [76].

Single-frequency lasers, like the ones used in this project, have very high temporal coherence. Moreover, the smaller the linewidth, the higher the temporal coherence and it has chosen to be ideal. However, high phase noise can drastically reduce such temporal coherence. This could not represent a threat since, depending on the specific application, either long or short temporal coherence may be of interest. For the specific case of this project, which is based on interferometry between signals, higher temporal coherence leads to better and more predictable results so the aforementioned distortions could negatively affect the performance of the reservoir circuit. How much this noise affects to the results as well as the minimum coherence requirements will be discussed during Chapter 3 and Chapter 4

# 3

# Methodology

In this chapter, the description of the designed photonic reservoir circuit by different levels of abstraction is explained in detail. It starts with the problem formulation, followed by an explanation of the physical implementation. Then, a mathematical analysis of the problem is shown and finally, the theoretical solution for the ideal case is shown.

## 3.1 Problem formulation

The task being adressed in this chapter consists of calculating the XOR between consecutive bits of a given input bitstream using a spatially distributed photonic reservoir and an electrical readout. Such a bitstream is generated by on-off keying modulation, an intensity modulation technique illustrated in Figure 3.1. After propagating through the reservoir, the output is converted to the electrical domain by direct detection, and the final result is obtained through a linear combination of the detected signals. Further details of the architecture will be given in the next section.

The XOR is a two-bit boolean operation that outputs a logic value '1' if the input bits are different, and a '0' if they are equal. Although it may seem like a trivial problem, solving it has interesting implications. It is a non-linear classification problem, which means that, given just the two input features (the two bits), it is not possible to determine whether the output should be zero or one just with a linear function, see figure 3.2. Hence,

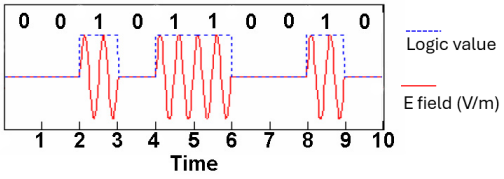


Figure 3.1: On-off keying modulation. It is a form of intensity modulation where the presence or absence of a carrier wave represents binary data, typically with the presence indicating a "1" and the absence indicating a "0.", achieving an efficiency of one bit per symbol [77].

the electrical readout is not enough by itself to calculate the XOR, so we need to find the appropiate reservoir configuration that makes the problem linearly separable.

Additionally, in real environments, noise and distortion effects must be taken into account when testing the actual device, so the task is far from being trivial. During the simulations, we considered both the case where the input signal is ideal, and real cases where the input signal includes fiber distortion, noise, high power effects and chromatic dispersion, which will be described in the simulation section.

Moreover, this problem is particularly convenient due to its low memory requirements. Calculating the XOR operation only requires two bits, which enables the construction of small circuits with a low number of parameters. This simplicity is especially useful when studying new architectures or exploring variations of existing ones.

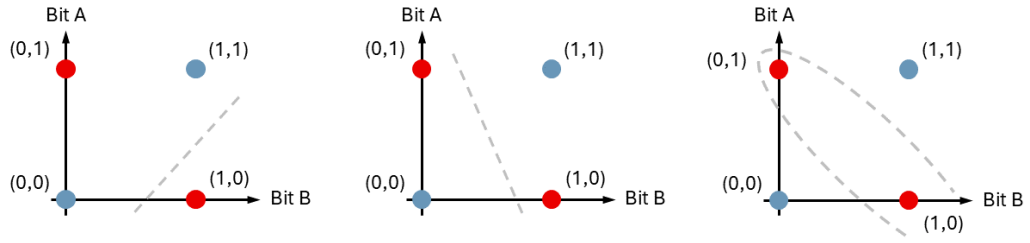


Figure 3.2: Interpretation of the XOR computation between two bits as a classification problem. Classifying with linear regression can be visualized with an hyperplane that discriminates the points corresponding to different classes. Points (0,1) and (1,0) correspond to class 1 (output XOR(0,1) = XOR(1,0) = 1), in red. Points (0, 0) and (1, 1) points correspond to class 0 (output XOR(0,0) = XOR(1,1) = 0), in blue. Linear functions are not able to discriminate correctly the classes, as seen in right and central figures, whereas the nonlinear function from the left figure is able to do it.

The objective of this task is to determine the optimal parameters $\theta$ and $\phi$, which correspond to the reservoir parameters and linear weights, respectively, such that, given an input bitstream $U = (u[1], u[2], \ldots, u[N])$, the generated output $\hat{Y} = (\hat{y}[1], \hat{y}[2], \ldots, \hat{y}[T])$ is the analog computation of the XOR logic gate between consecutive bits of the input $U$. In other words:

$$\hat{Y} = g_\theta \circ f_\phi(U) = XOR(U) \tag{3.1}$$

Here, $g_\theta(\cdot)$ represents the reservoir stage, where the recurrent dynamics take place. This recurrence is expressed as follows:

$$g_\theta : x[n+1] = \sigma(W^{res}x[n] + W^{in}u[n]) \tag{3.2}$$

In this equation, $u[n]$ denotes the input signal at discrete time $n$, $x[n]$ represents the state of the reservoir, which includes the signals at all of its nodes, and $x[n+1]$ indicates the state of the reservoir at the next time step. The terms $W^{in}$, $W^{res}$ and $\sigma$ model the reservoir dynamics, where $W^{in}$ and $W^{res}$ perform the transformations $W^{in} : \mathbb{R} \rightarrow \mathbb{R}^m$ and $W^{res} : \mathbb{R}^m \rightarrow \mathbb{R}^m$, respectively. This reflects how the reservoir maps the temporal series into a higher-dimensional space. Details on which physical property corresponds to which parameter will be discussed later. However, it is important to note that, unlike traditional reservoirs where every parameter is fixed and set randomly, the dynamics of this reservoir can be modified. In this work, the set of variable parameters, denoted as $\theta$, only includes $W^{res}$.

The $f_\phi(\cdot)$ term represents the readout linear stage, described by the following expression:

$$f_\phi : \hat{y}[n] = W^{out} x[n] \tag{3.3}$$

This equation represents a linear regression, where $x[n]$ is the reservoir state, $\hat{y}[n]$ is the readout output, and $W^{out}$ denotes the linear weights. In this expression, the transformation performed by $W^{out}$ maps the reservoir state from the higher-dimensional space $\mathbb{R}^m$ to the output space $\mathbb{R}$, specifically described as $W^{out} : \mathbb{R}^m \rightarrow \mathbb{R}$. Furthermore, in this kind of reservoir architectures, not necessarily the expected output is achieved just when the new bit is inserted into the circuit. The dynamics need to process the signal with the new information, so a delay $\tau$ before computing the linear regression also needs to be optimized. It can be directly computed using the Moore-Penrose pseudo-inverse [68]:

$$W^{(out)} = (X^\intercal X + \beta I)^{-1} X^\intercal Y \tag{3.4}$$

where $Y = (y[1], y[2], \ldots, y[N])$ denotes the target value of the reservoir output $\hat{Y}$, $X$ is the vectorial notation for the reservoir state $x[n]$, and $\beta \in [0, 1]$ is a regularisation term. The demonstration for this expression is provided in Section 2.6. The set of variable parameters $\phi$ includes the weight matrix $W^{out}$, whose size depends on the number of dimensions obtained from the reservoir stage, as well as the delay $\tau$ and the normalization term $\beta$. These are the parameters typically adjusted during the optimization process in reservoir computing schemes.

Optimizing the entire circuit can be done using gradient-based algorithms like stochastic gradient descent (SGD) during simulations, where the state of the circuit is fully observable at every moment. Gradient descent works by computing the gradient of a loss function with respect to each parameter, indicating how to adjust the parameters to reduce the loss. This process involves iteratively updating the parameters in the direction that minimizes the loss function. However, in physical systems, tracking intermediate values and computing these gradients is difficult because the system's state is not always accessible or easily measurable. Therefore, alternative methods are employed in physical implementations. Instead, in this case, the parameters from sets $\theta$ and $\phi$ can be determined

through a two-step process. First, the values of $\theta$ are chosen such that the problem becomes separable by the linear stage. Subsequently, the values of $\phi$ are optimized to correctly perfrom the linear regression. The former can be obtained through black box optimization techniques like bayesian optimization or genetic algorithms, among others, while the latter can be obtained just with a grid search, as the computational requirements of calculating the pseudoinverse are low. However, this work focuses on studying how variations in the reservoir's internal parameters affect its dynamics. Therefore, instead of using black-box optimization techniques, grid search is employed to observe the circuit's response. Additionally, rather than iterating until convergence— which would be the most efficient approach— the process is carried out for a fixed maximum number of iterations to better capture the dynamics' variations. As a result, the target output is the response of the circuit rather than the optimal configuration of the reservoir. This procedure, referred to as reservoir parameter sweep, and the optimization of the linear regression weights, are detailed in Algorithm 1.

**Algorithm 1** Algorithm for the reservoir parameter sweep $(W^{res})$ and the optimization of the readout parameters $(\beta, \tau, W^{out})$. Superscript denoted by $A^*$ refers to the optimal value of the parameter $A$.

Initialize $W^{res}, W^{out}, \beta, \tau$
Initialize error_record $\leftarrow [\,]$
**for** iteration = 1 to max_iterations **do**
    $W^{res} \leftarrow$ GridSearch$(W^{res})$
    Initalize $\beta^*, \tau^*$
    Initialize best_linear_error $\leftarrow \infty$
    **for** each $\beta, \tau$ in grid **do**
        $W^{out} \leftarrow$ LinearRegression$(W^{res}, \beta, \tau)$
        error $\leftarrow$ EvaluationFunction$(W^{res}, \beta, \tau, W^{out})$
        **if** error $<$ best_linear_error **then**
            $\beta^* \leftarrow \beta$
            $\tau^* \leftarrow \tau$
            best_linear_error $\leftarrow$ error
        **end if**
    **end for**
    $W^{out} \leftarrow$ LinearRegression$(W^{res}, \beta^*, \tau^*)$
    error $\leftarrow$ EvaluationFunction$(W^{res}, \beta^*, \tau^*, W^{out})$
    error_record.append(error)
**end for**
**return** error_record

## 3.2 Physical implementation

To model the system described above, the approach taken during this project involved designing a tunable photonic reservoir circuit using PZT electro-optic modulators as variable parameters on a Silicon on Insulator (SOI) platform. The goal was not to implement a fully optical reservoir circuit, but rather an opto-electronic circuit with weights both in the electrical and optical domain, allowing control over the reservoir's dynamics to perform the desired operation. The chosen topology is a 2x2 swirl architecture, where the nodes are 3x3 structures formed by either cascaded 2x2 balanced MMIs, which results in an unbalanced, asymmetrical node, or 3x3 balanced MMIs, with an electrical readout, as illustrated in Figure 3.3. An MMI is balanced if it equally distributes the input power among all its output modes, ensuring uniform signal distribution across its ports. We can represent the splitting ratio of these devices using the S-matrix formalism, which describes the relationship between waves at the input and output ports of a network. Therefore, considering an ideal case where no loss or reflections occur, the transmitted power of the balanced nodes can be expressed as:

$$|S|^2 = \begin{bmatrix} 0.62 & 0.33 & 0.05 \\ 0.33 & 0.33 & 0.33 \\ 0.05 & 0.33 & 0.62 \end{bmatrix} \tag{3.5}$$

These ratios are based on the actual S-parameters of the 3x3 MMIs used in the circuit simulations. For the case of unbalanced nodes, the splitting ratios can be expressed as:

$$|S|^2 = \begin{bmatrix} \frac{1}{2} & \frac{1}{2} & 0 \\ \frac{1}{4} & \frac{1}{4} & \frac{1}{2} \\ \frac{1}{4} & \frac{1}{4} & \frac{1}{2} \end{bmatrix} \tag{3.6}$$

These values can be easily obtained using two ideally balanced 2x2 MMIs connected like in Figure 3.3. In these matrices, the element $|s_{ij}|^2$ represents the ratio of the power at output port *out i* to the power at input port *in j*. The two external input and output ports of each node are used to connect the circuit, while the central input port and the central output port are utilized to couple light into and out of the reservoir, respectively. There are two main reasons for choosing these types of nodes:

- Reduced Radiation Loss: Using MMIs instead of Y junctions/splitters helps to avoid the excessive radiation loss of the Y junctions caused by their reciprocity.
- Enhanced Interaction Richness: MMIs exhibit intrinsic richness of interactions because of their multimode nature, which improves the dynamic capabilities of the system.

In principle, the performance of the circuit when unbalanced nodes are used is superior to using balanced nodes

because they often provide more diverse and richer dynamics, so the results obtained from studying the worst case would cover both scenarios. Additionally, it is much easier to provide a reliable S-matrix model for the 3x3 MMI nodes since it is a unique component, so it was decided to run the simulations with these type of devices. Regarding the design and fabrication of the actual chip, the 2x2 MMIs have alredy been tested and optimized in the UGent cleanroom before this study, both in design and fabrication processes, which is not the case for the 3x3 MMIs. For that reason, it was decided to use the cascaded 2x2 devices instead in the chip.

The interconnections between nodes include a delay of exactly one bit period, ensuring that when a bit is injected into one node and propagates through the interconnection lines, it arrives at the next node just as another bit is injected, allowing for interaction between them [29]. However, this constraint limits the design to a specific data rate. Therefore, if a different bit rate is required, a new circuit must be fabricated.

The phase shifters, which, as mentioned before, are in charge of modifying the circuit dynamics, are placed in every interconnection line between nodes, so 8 of them are required. This allows to fully control the reservoir dynamics by covering all phase variations within the reservoir connections.

In the readout stage, after passing through the photodetectors, the four signals are combined by weighted sum. These weights are implemented electrically, allowing for arbitrary values to be set to optimize performance.

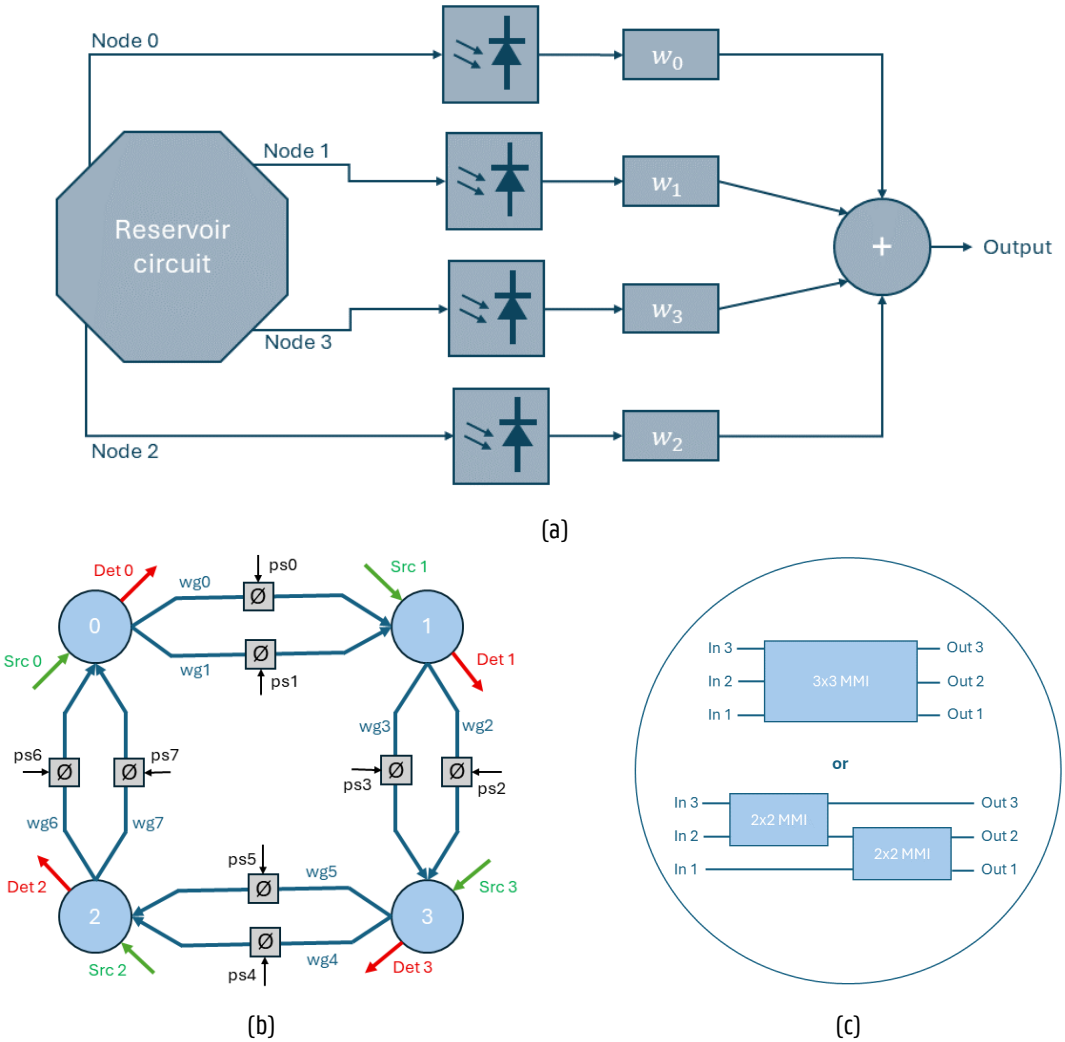


Figure 3.3: In (a), the overall system architecture is depicted, highlighting its key components. The diagram clearly shows two primary sections: a reservoir stage, where the signal undergoes processing, and, following the photodetectors, a stage where a linear combination of the signals from the reservoir nodes is performed within the electrical domain. In (b), a detailed schematic of the reservoir circuit architecture is provided, illustrating its swirl topology. This topology is characterized by the unidirectional flow of signals, where each node is connected sequentially to the next, ensuring continuous signal propagation. Each node in the network has the capability to couple light into and out of the reservoir. Additionally, every interconnection between nodes is equipped with a phase shifter, which allows for precise tuning of the network's behavior. In (c), an example of one of the nodes is shown. The node architecture follows a 3x3 configuration, which can be constructed using either cascaded 2x2 MMIs or 3x3 MMIs. It is important to note that all four nodes share an identical structure, and there is no mixing of balanced and unbalanced nodes within the same circuit.

Hence, matching with the equations from the previous section, the parameters used for the linear regression

$W^{out}$ correspond to the electrical weights from the readout stage, while the parameters from the reservoir, $W^{in}$, $W^{res}$, correspond to the phase shifts of the signals propagating into and within the reservoir, respectively. As previously mentioned, only $W^{res}$ is adjustable, and this tunability is achieved through the use of phase shifters. The transformations performed by the reservoir $g_\theta$ can be thus expressed as $W^{in} : \mathbb{R} \rightarrow \mathbb{R}^4$ and $W^{res} : \mathbb{R}^4 \rightarrow \mathbb{R}^4$, and the ones from the linear regression $f_\phi$ can be expressed as $W^{out} : \mathbb{R}^4 \rightarrow \mathbb{R}$.

## 3.3 Mathematical analysis

### 3.3.1 Interference of optical waves

This phase control over the signals propagating within the reservoir is essential in modelling how the signals "interact" with each other. In reality, the electromagnetic waves themselves do not interact, but the interference pattern observed at the detector varies with the phase mismatch between the received signals when their polarization states are not orthogonal. The detector measures the intensity of the total field in such region, which is the time-averaged energy density $< U(r,t) >$ and it is calculated as:

$$I = I(r,t) =< U(r,t) >= \epsilon < E(r,t)E(r,t) > \tag{3.7}$$

with

$$< U(r,t) >= \frac{1}{T}\int_0^T U(r,t)dt \tag{3.8}$$

Thus, when a single wave $E_n(r,t) = A_n \cos(\omega_n t - k_n \cdot r + \phi_n(t))$ is propagating, the intensity displayed is a constant value equal to the halved squared modulus, which can be easily calculated:

$$\begin{aligned} I_n &= \epsilon < E_n(r,t)E_n(r,t) >= \epsilon < |A_n|^2 \cos^2(\omega_n t - k_n \cdot r + \phi_n(t)) > \\ &= \frac{\epsilon}{2}|A_n|^2 < 1 + cos(2[\omega_n t - k_n \cdot r + \phi_n(t)]) > \\ &= \frac{\epsilon}{2}|A_n|^2 \end{aligned} \tag{3.9}$$

However, when multiple waves are propagating through the same media, the total field is the result of the superposition between all the waves. In the case of a two wave superposition, in terms of intensity, it appears to be an interference and this is shown as a beating, an additional oscillatory term which depends on the phase difference. This is taken into account always that the frequency of both waves are similar. Hence, given two optical waves

$E_1(r,t) = A_1 \cos(wt - k_1 r + \phi_1(t))$ and $E_2(r,t) = A_2 \cos(wt - k_2 r + \phi_2(t))$, the total intensity of their superposition is:

$$\begin{aligned} I &= \epsilon < (E_1(r,t) + E_2(r,t)) \cdot (E_1(r,t) + E_2(r,t)) > \\ &= \epsilon < (E_1(r,t))^2 > + \epsilon < (E_2(r,t))^2 > + 2\epsilon < E_1(r,t) E_2(r,t) > \\ &= \epsilon \frac{A_1^2}{2} + \epsilon \frac{A_2^2}{2} + \epsilon A_1 A_2 < \cos((w_1 - w_2)t + (k_1 - k_2)r + \phi_1(t) - \phi_2(t)) > \\ &+ \epsilon A_1 A_2 < \cos((w_1 + w_2)t + (k_1 + k_2)r + \phi_1(t) + \phi_2(t)) > \\ &= I_1 + I_2 + 2\sqrt{I_1 I_2} < \cos((w_1 - w_2)t + (k_1 - k_2)r + \phi_1(t) - \phi_2(t)) > \end{aligned} \tag{3.10}$$

where the $\cos((w_1 + w_2)t + (k_1 + k_2)r + \phi_1(t) + \phi_2(t))$ term is zero because $T >> \frac{1}{\omega_1 + \omega_2}$. If $\omega_1 = \omega_2$. In this case, as we are using a source with (ideally) a single frequency, the frequency of both waves is the same, $w_1 = w_2$, so the phase difference can be expressed as $\Omega = Kr + \Delta\phi(t)$, with $K = k_1 - k_2$ and $\Delta\phi(t) = \phi_1(t) - \phi_2(t)$. As these waves are propagating within the same medium, which is assumed not to be birefringent, and in the same direction, we can consider as well $K = 0$. Accordingly, $\Delta\phi(t)$ can be considered stationary under these conditions, i. e. the phase difference remains constant because the two waves are mutually coherent. However, due to the stochastic nature of the phase error sources, we should also include an extra term that models such variability, which increases in importance with the level of distortion and can be represented as $\delta(t)$:

$$I = I_1 + I_2 + 2\sqrt{I_1 I_2} \cos(\Delta\phi + \delta(t)) \tag{3.11}$$

Thus, it is clear now why a phase shifter is relevant. Modifying the phase difference of the waves can alter the intensity measured in the detector, ranging from $I_1 + I_2 - 2\sqrt{I_1 I_2}$ to $I_1 + I_2 + 2\sqrt{I_1 I_2}$ in the case of a two-wave interference. This can be leveraged for computing, as it allows the output value to be adjusted based on the selected phase shifts.

For the case of multiple wave interference, the same reasoning can be followed so, for a general case of $N$ waves superposition, the total field can be expressed as:

$$E(r,t) = \sum_{n=1}^{N} E_n(r,t) \tag{3.12}$$

with

$$E_n(r,t) = A_n \cos(\omega_n t - k_n \cdot r + \phi_n(t)) \tag{3.13}$$

for fields with colinear polarization. This assumption can be done consistently as for the waveguides used, only the ground TE mode is propagating, so there should be no mismatch.

Accordingly, the resulting intensity at the detector is:

$$I = \sum_{n=1}^{N} I_n \sum_{n=1}^{N} \sum_{m=1, m\neq n}^{M} \sqrt{I_n I_m} \cos\left(\Delta\phi_{n,m} + \delta_{n,m}\right) \tag{3.14}$$

Notes from the 'Microphotonics' course were used for this demonstration [78].

### 3.3.2 Study of feasibility

A simplified version of the circuit has been employed for an analytical evaluation of the system, which can provide insights on how to solve the task, identify limitations, determine acceptable tolerances to maintain performance, establish the minimum required complexity, and evaluate the role of the reservoir when phase shifters are present. To achieve this, the formalisms and expressions explained in the previous section regarding wave interference at the detector between multiple signals with the same frequency and colinear polarization will be used. This was initially studied for the ideal case where no distortions are present and, during the simulation chapter, the impact of these distortions on the output will be discussed. It is important to note that, in this scenario, only the signals corresponding to the two consecutive bits used to calculate the XOR are relevant. Any other interaction with signals unrelated to those bits can be considered as noise, as they are independent and should not affect the output.

Thus, given the architecture presented in the previous section, the first decision to be made is which nodes (if not all) will be used as sources to input the signal into the circuit. It is important to remember that, given the ideal nature of the signal, it is not possible to solve the XOR task with just linear regression. Therefore, using only one node as input implies that the interference would be only between the phase variations of the same bit (due to the different waveguide paths between consecutive nodes), which does not provide the necessary transformations to achieve the desired output. Signals from prior and subsequent cycles do not necessarily provide useful interactions, as we assume the signal to be ideal (especially with no chromatic dispersion). This can be seen as merely scaling the values of the on states of the bits, without changing the data distribution. The off states are zeros in terms of intensity, so the output in this case is always 0. It is then evident that the interaction of the bits in consecutive nodes is needed to achieve a certain level of performance. This explanation holds for the current case of study where the interconnections between nodes have a delay equal to one bit period.

In machine learning tasks, the minimum complexity that yields the expected output is always preferred over more complex models with the same performance for several reasons. The intermediate operations within the network are more easily interpretable, which is crucial for determining which features are relevant for the task.

For instance, in medical image processing, being able to analyze which parts of the tissue are most relevant to the diagnosis is fundamental to truly assist doctors. Lower complexity models also have a reduced risk of overfitting. As complexity increases, the model can identify more complex patterns and distributions, but this might mean that for a simpler task, the architecture is too specialized for the training dataset and cannot generalize to unseen data, decreasing the overall performance. Additionally, inference time and delay increase with larger complexity models, as more operations are required to solve the task. During model optimization, finding the optimal parameters is easier and faster in a low complexity model. Although we are using a reservoir computing architecture, the utilization of phase shifters can be considered as the network parameters, making this topic relevant during model design, even if only a few of them are being used.

Hence, the configuration that allows for the desired performance while maintaining the lowest possible complexity involves using nodes 0 and 1 as inputs to the network, as shown in figure 3.4. This approach permits the interaction between consecutive bits in node 1, enabling the XOR computation with a proper configuration of phase shifters in waveguides 0 and 1. Nodes 2 and 3, as well as the feedback signal from the recurrence of the model itself, will be neglected for this part of the analysis.

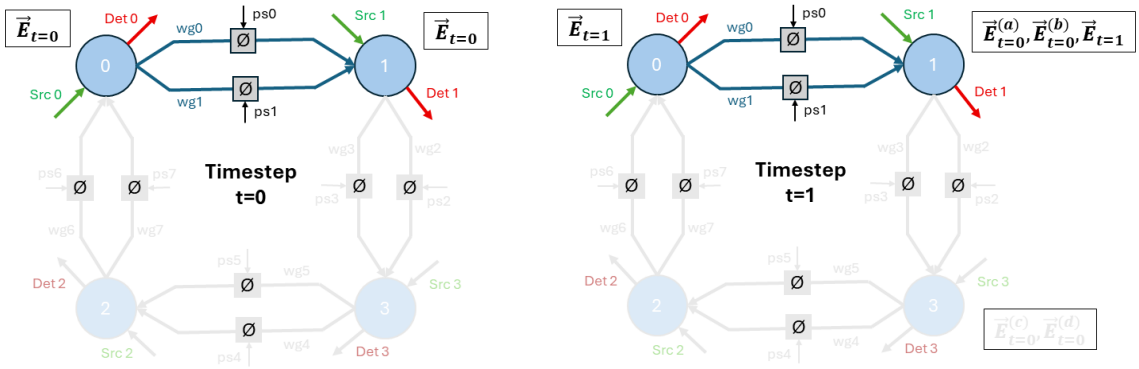


(a) (b)

Figure 3.4: Signal interference in each detector of the reservoir at various instants of time. Each tick represents a bit cycle, meaning every increment of the time variable t by 1 corresponds to the arrival of a new bit to the circuit, while bits already within the circuit move to the next node. This section focuses on the first two nodes, they are the only ones receiving new signals, while the rest of the circuit is ignored. With each propagation between nodes, the number of signals from that instant doubles due to the different waveguide paths. These signals are distinct because they arrive with random, independent phases, resulting in them being out of phase.

To study such a system, an interpretation from a classification point of view can provide a clearer understanding of the problem. The goal of this architecture is to solve a regression task which, given two input bits, should output a value of one when those bits are different, and a value of zero when these bits are equal, as previously explained. However, in bit-related tasks, the important thing is that the actual resulting value is above or below

a certain threshold, as we are working with discrete elements; the critical aspect is the logical value. Thus, this is equivalent to a classification problem where, instead of looking at the exact computed value, we care about whether it meets the threshold criteria.

The process of calculating the electrical weights of the readout by linear regression involves establishing the linear relation that best relates the reservoir states to the corresponding output. For a two-node system, the linear relation corresponds to a plane in a three-dimensional space, with two axes representing detected signals from the nodes, and the third representing the output value of the linear regression itself. In a higher dimensional space, this is represented as a hyperplane. Translated to our specific problem, to achieve the XOR computation, we must design the circuit such that the transformation performed by the reservoir allows us to linearly separate the data points that have different outputs, which is a projection to a smaller dimensional space from the original regression problem. A representation of these two concepts are depicted in figure 3.5. This assures that it is possible to perform a linear regression that effectively separates the two kind of outputs, by leaving the bit combinations that should be zero under the threshold, and the ones that should be one, over it.

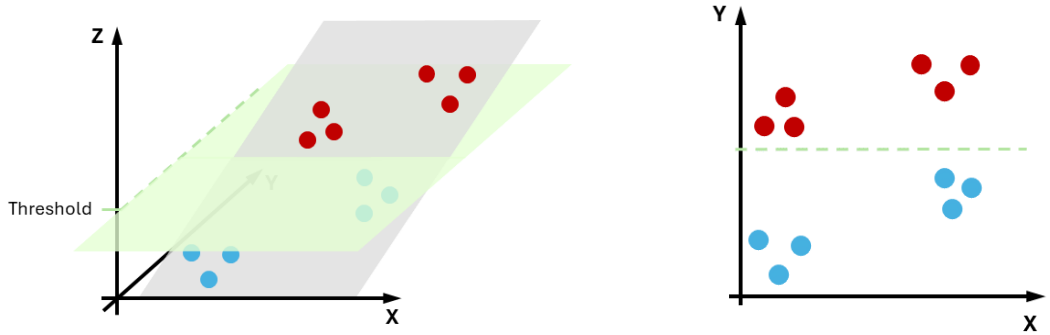


(a) (b)

Figure 3.5: In (a), the linear regression problem for a two input and two node system is depicted. It is a 3 dimensional space, where the plane maps such linear relation from the X and Y axis, that contain the input features, to the Z axis, that represents the output. Figure in (b) shows how this 3D problem can be translated to a 2D classification problem, projecting the intersection of the threshold plane with the plane found by linear regression as a straight line in the XY plane.

Therefore, to reach that condition, we have to analyze the effect of modifying the two phase shifters when two consecutive bits are introduced into the network. In this case, the detector at node 0 is receiving the signal from the bit at timestep 1, whereas the detector at node 1 is receiving the interference between bits at timesteps 0 and 1. The latter corresponds to an interference of three signals, two coming from the node 0 by different waveguides, and one being injected directly into the node 1. The splitting coefficients for balanced 3x3 MMIs as nodes are the ones shown in the S-matrix 3.5. Approximating $0.33$ to $\frac{1}{3}$, the resulting intensity can be expressed follows:

$$I = \frac{1}{3}(I_{t=1} + I_{t=0}\frac{2}{3}x(1 + \cos(\Delta\phi_0)) + \sqrt{I_{t=1}I_{t=0}}\frac{2}{\sqrt{3}}\sqrt{x}(\cos(\Delta\phi_1) + \cos(\Delta\phi_2))) \quad (3.15)$$

In this equation, $I_{t=1}$ and $I_{t=0}$ are the intensities of the bit signals at timesteps 1 and 0, respectively. The phase values within the cosine terms $\Delta\phi_0$, $\Delta\phi_1$ and $\Delta\phi_2$ represent the phase difference between the three interfering signals. $\Delta\phi_0$ represents the phase difference between the two signals coming from node 0, while $\Delta\phi_1$ and $\Delta\phi_2$ represent the phase difference between these signals with respect to the one injected at node 1. These three values are dependent on each other, so there are actually two variables and not three. For example, $\Delta\phi_0$ could also be expressed as $\Delta\phi_1 - \Delta\phi_2$. The $x$ term denotes the transmission loss caused by the waveguides, i. e. $x = e^{-\alpha L}$. The resulting outputs of nodes 0 and 1 after evaluating all possible bit combinations at timestep 1 are shown in Table 3.1. Note that the intesity has been multiplied by 3 to remove the prefactor from Equation 3.15, since the relations between the different cases are equivalent and the expressions get simplified.

| **Input intensity** | | **Output normalized intensity** | |
|---|---|---|---|
| **t=1** | **t=0** | **Node 0** | **Node 1** |
| 0 | 0 | 0 | 0 |
| 0 | 1 | 0 | $\frac{2}{3}x(1 + \cos(\Delta\phi_0))$ |
| 1 | 0 | 1 | 1 |
| 1 | 1 | 1 | $1 + \frac{2}{3}x(1 + \cos(\Delta\phi_0)) + \frac{2}{\sqrt{3}}\sqrt{x}(\cos(\Delta\phi_1) + \cos(\Delta\phi_2))$ |

Table 3.1: Simplified intensities resulting from the interference of all posible bit configurations.

Graphically, it can be depicted as in figure 3.6. It can be seen that, to reach the desired separability, the following condition must hold:

$$1 + \frac{2}{3}x(1 + \cos(\Delta\phi_0)) + \frac{2}{\sqrt{3}}\sqrt{x}(\cos(\Delta\phi_1) + \cos(\Delta\phi_2)) < 1 \quad (3.16)$$

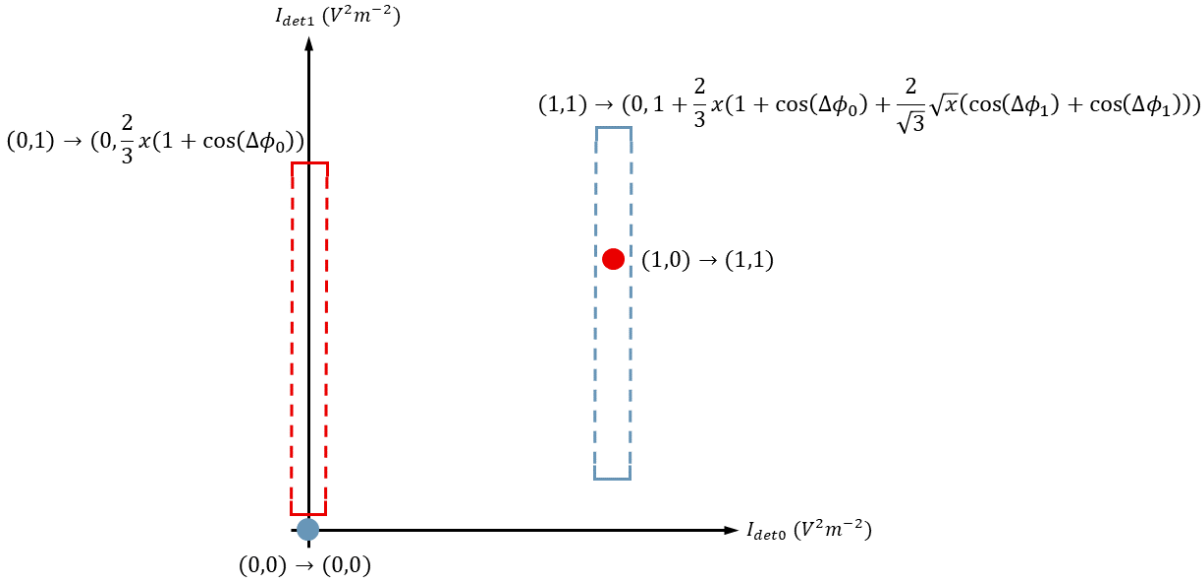


Figure 3.6: Transformed space after observing the output of nodes 0 and 1 at timestep 1. It is clearly visible how the proper use of the phase shifters, allow to find the separability condition by shifting the transformed state corresponding to an input bit sequence of (1,1) below the state found when the input bit sequence is (1,0).

from here, several conclusions can be extracted. First, an interesting case worth studying is the one in which the phase shifters have values $\Delta\phi_0 = 0$, $\Delta\phi_1 = \pi$ and $\Delta\phi_2 = \pi$. Although these are not necessarily optimal for each specific case of losses $x$, they do allow us to reach the following conclusion:

$$\begin{aligned} 1 + \frac{4}{3}x - \frac{4}{\sqrt{3}}\sqrt{x} &< 1 \\ \frac{4}{3}x - \frac{4}{\sqrt{3}}\sqrt{x} &< 0 \\ x &< 3 \end{aligned} \tag{3.17}$$

Which means that, for an ideal case where only such signals are present and the possibility of setting an arbitrary value of the phase shifters, a solution that works for any amount of waveguide loss can be found. The lowest possible loss for passive components is represented with $x = 1$, so the upper bound $x < 3$ always holds. The plot in figure 3.7 exemplifies this result and provides more insights on the system behaviour.

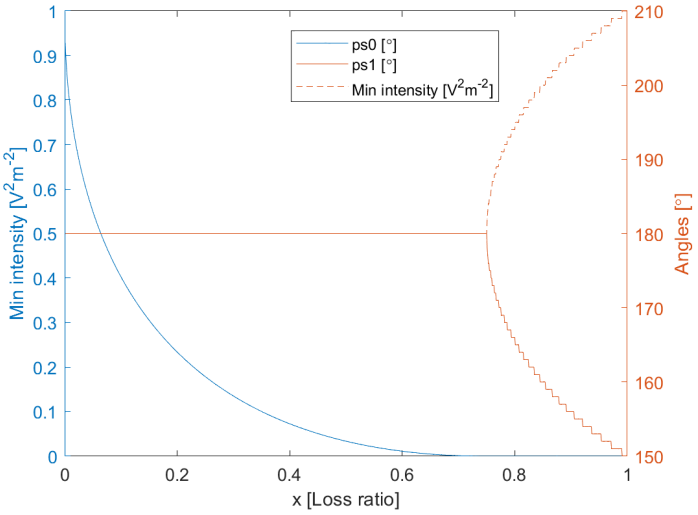


Figure 3.7: Minimum achievable intensity for the state obtained by the input sequence (1,1), based on equation 3.15. On the x axis, the linear waveguide loss is swept. On the left y axis, in blue, the minimum achievable intensity is represented, while along the right axis, in red, the $\Delta\phi_1$ and $\Delta\phi_2$ required values for such minimum intensity are shown. It can be appreciated that for a loss of $x = 0.75$, both phase differences must be equal to $\pi$ to reach the minimum.

It is also relevant to study, given a specific loss $x$ that matches the one that will be then used during the circuit simulations, which is the range of $\Delta\phi_0$, $\Delta\phi_1$ and $\Delta\phi_2$ values that still keep the state generated by the sequence (1,1) under the threshold defined in equation 3.16. Therefore, as it is described in Chapter 4, the waveguide loss is considered to be $2dB \cdot cm^{-1}$ with a waveguide length between nodes of $L_{wg} = 2.292mm$, so that the propagation time is exactly one bit period for a data rate of 32Gbps and an $n_g = 4.088$. Therefore, the loss term has a value of $x = 0.8998$. Now, doing a sweep over the different possible values of the phase shifters by modifying $\Delta\phi_1$ and $\Delta\phi_2$, we obtain the behaviour shown in figure 3.8.

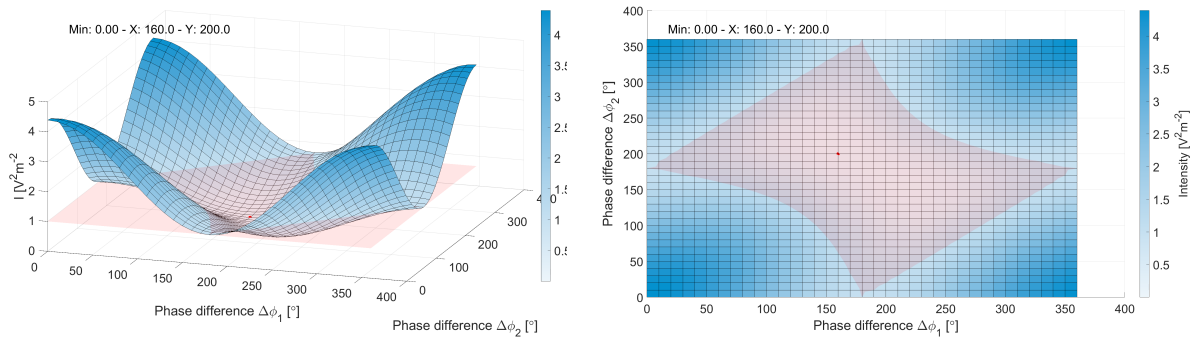


(a) (b)

Figure 3.8: Instensity measured in node 1 with respect to all the posible combination of values of $\Delta\phi_1$ and $\Delta\phi_2$. Two alternative views are provided in (a) and (b). As was shown in Equation 3.16, the intensity should be under 1 to match the separability condition, and this threshold is defined by the red plane. Every part of the surface that lay below the threshold can be separable through linear regression. The values at which the minimum value is achieved as well as this minimum value are also indicated in both figures as an annotation. The red dot laying on the surface graphically shows such minimum.

Continuing with this approach, more conclusions can still be drawn. On the one hand, if we fix the losses to the case study, it is possible to identify the range of phase error that is admissible to maintain a correct operation of the system. Graphically, it is possible to observe that the point that has a higher tolerance to these variations is $\Delta\phi_1 = \pi$ and $\Delta\phi_2 = \pi$, as it is the furthest from the closest point where the system is not linearly separable. The maximum permissible error can approximately be calculated considering the diagonal of the figure, with $\Delta\phi_2 = \Delta\phi_1$, and taking the limit from equation 3.16:

$$\begin{aligned} 1 + \frac{2}{3}x(1 + \cos(\Delta\phi_1 - \Delta\phi_2)) + \frac{2}{\sqrt{3}}\sqrt{x}(\cos(\Delta\phi_1) + \cos(\Delta\phi_2)) = 1 \\ \frac{4}{3}x + \frac{4}{\sqrt{3}}\sqrt{x}\cos(\Delta\phi_1) = 0 \\ \Delta\phi_1 = \arccos(-\sqrt{\frac{x}{3}}) = 2.1504rad = 123.21° \end{aligned} \tag{3.18}$$

This means that, to make sure that the output is always bounded within the working range, and in case that such critical point is achievable by tuning the phase shifters, the phase difference between signals from node 0 and the signal from node 1 should have a maximum variation of $\pm 56.79°$.

On the other hand, we can also determine what minimum resolution is required when using non-volatile phase shifters so that we can still make the system work. To give an approximate value for a lower bound, we can

determine the maximum admissible phase variability on the opposite axis to the one calculated before, which is the most tolerant axis for the worst case. From that, we can specify the largest admissible difference between the phase shifter states, considering a constant variation. This case corresponds to the state where $\Delta\phi_2 = \Delta\phi_1 + 180°$. Comparing the central points on top left and bottom right edges which are $(90°, 270°)$ and $(270°, 90°)$, we can see that $d_{min} = \sqrt{(\Delta\phi_1 - \Delta\phi_2)^2 + (\Delta\phi_2 - \Delta\phi_1)^2} = 180°$ so the minimum number of non-volatile states need to be:

$$n_{states} = \lceil \frac{360}{d_{min}} \rceil = 3 \tag{3.19}$$

Note that taking $n_{states} = 2$ would provide phase shifter configurations at the edge of the working region, so we considered $\lceil 2 \rceil = 3$. It can be better understood looking at figure 3.9. In this graph, we have plotted the possible states that two 3-state non-nvolatile phase shifters are capable of generating for specific initial conditions. It can be seen that, no matter how much the grid is shifted or rotated, there is always a point that stays within the area of interest, so that with a device of these characteristics it would be possible to make it work. But this is for the ideal case. If we considered the phase errors, the tolerance would be much lower, so this needs to be improved if these kind of devices are used. During the simulations, it will be possible to see how a more complex modelling of the system afects the performance, how the non ideal conditions degrade the results and how the reservoir can be uesd to increase the tolerance of the system.

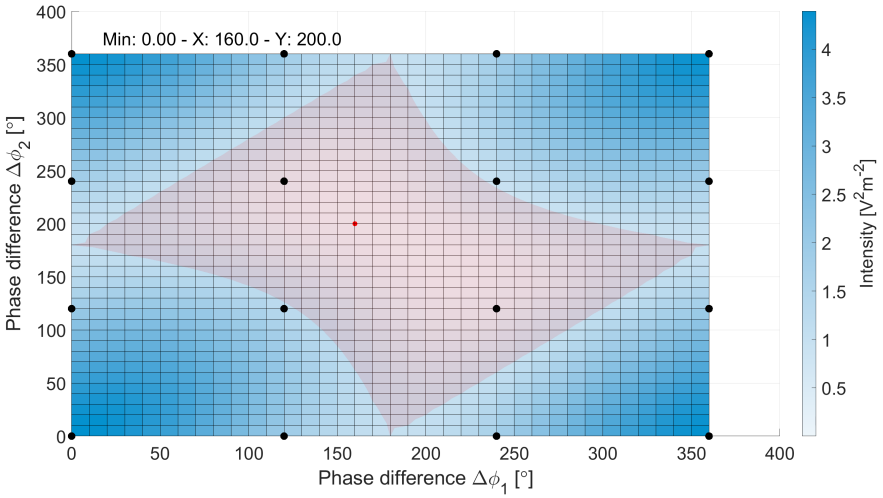


Figure 3.9: Sweep from Figure 3.8, but with overlapping black dots showing the operating states that would be possible to achieve with 3-state non-volatile phase shifters.

# 4

# Circuit simulation

In this chapter, we show and discuss the simulations that have been carried out to evaluate the performance of the circuit, sizing its capabilities and testing different hypotheses. Moreover, the generation process of the bitstreams used during these simulations is also shown, together with an analysis of such signals.

## 4.1 Description of the tools

To generate the input bitstream used during the simulations to train and evaluate the reservoir, the VPIphotonics framework [79] has been utilized. This comprehensive simulation platform offers advanced tools for the modeling, analysis, and optimization of photonic components, systems, and networks. By supporting the design and performance evaluation of complex photonic devices, VPIphotonics enables the simulation of optical signals, nonlinear effects, and signal processing within photonic systems, making it well-suited for the specific needs of this project.

To simulate the signal propagation within the reservoir, the open-source Python-based library Photontorch [80] was used. Photontorch is specifically designed for simulating and optimizing photonic circuits, allowing users to model and refine optical components and photonic systems. Leveraging PyTorch's machine learning framework, it facilitates gradient-based optimization tasks in photonics. Although gradient-based optimizations were not employed in this project, Photontorch remains a powerful tool for conducting the necessary temporal simulations, effectively capturing the dynamic behavior of the reservoir system.

In this project, devices in Photontorch are modeled using the Scattering Matrix (S-matrix) formalism, where Scattering parameters (S-parameters) describe the relationship between incoming and outgoing signals in a multiport network. This formalism is particularly effective for characterizing passive devices, as it provides a complete description of how energy is distributed or scattered within the device. Given that the reservoir is entirely passive, the S-matrix formalism offers a comprehensive way to capture its behavior, ensuring all interactions within the

device are accurately represented through these parameters.

## 4.2 Signal generation

The input bitstream for the reservoir was simulated as an OOK (On-Off Keying) telecommunications signal, an intensity-modulated signal that propagates through several kilometers of fiber before reaching its destination. Not all distortions involved in the process have been considered in the generation, but a selection of the most important and typical effects has been. A schematic of the setup used in the signal generation is shown in Figure 4.1.

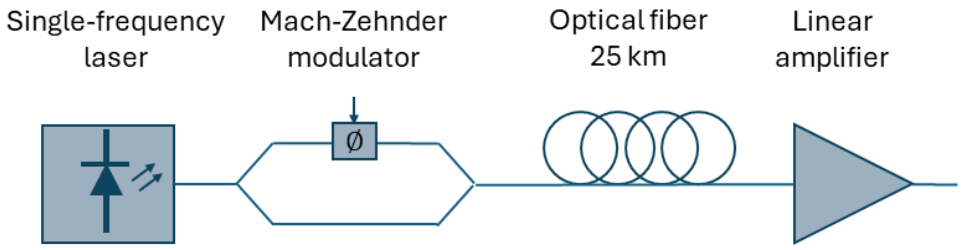


Figure 4.1: VPI simulation setup used to generate the simulation signals.

Each component in this configuration introduces various distortions that impact both the intensity and phase of the signal, thereby degrading the quality of the transmitted bits. These effects are detailed in Chapter 2. To analyze the influence of these distortions on the performance of the designed architecture, different parameter configurations were used in the signal generation process. Table 4.1 provides an overview of the key fixed and variable parameters in the transmission system.

| Parameter category | Parameter | Value |
|---|---|---|
| General parameters | Number of symbols per set of data (training, validation, test) | 1024 |
| | Samples per symbol | 16 |
| Source parameters | Carrier frequency | 193.1 THz |
| | Transmitted power | 3/18 dBm |
| | Optical signal to noise ratio | 27 dB |
| | Linewidth | 0 Hz |
| Modulator parameters | Symbol rate | 32 Gbps |
| Fiber parameters | Length | 25 km |
| | Chromatic dispersion compensation | Yes/No |
| Amplifier parameters | Noise | Yes/No |
| | Noise Figure | 4 dB |
| | Bandwidth | 4 THz |

Table 4.1: Summary of the main transmission setup configuration parameters used during the simulations.

Note that three of the parameters alternate between two possible values, from which five different configurations were used to generate the signals for the simulations: all four combinations of transmitted power and amplifier noise variables when chromatic dispersion compensation is employed, and the case without chromatic dispersion compensation, low transmitted power, and no amplifier noise. Chromatic dispersion alone is sufficient to significantly degrade the system's performance, so testing other combinations with additional distortions is unnecessary. In Figure 4.2, an example of these signals is depcited, as well as the ideal case where no distortions are present. To easily identify which signals correspond to which parameter configuration, the auxiliary table 4.2 provides for these relations.

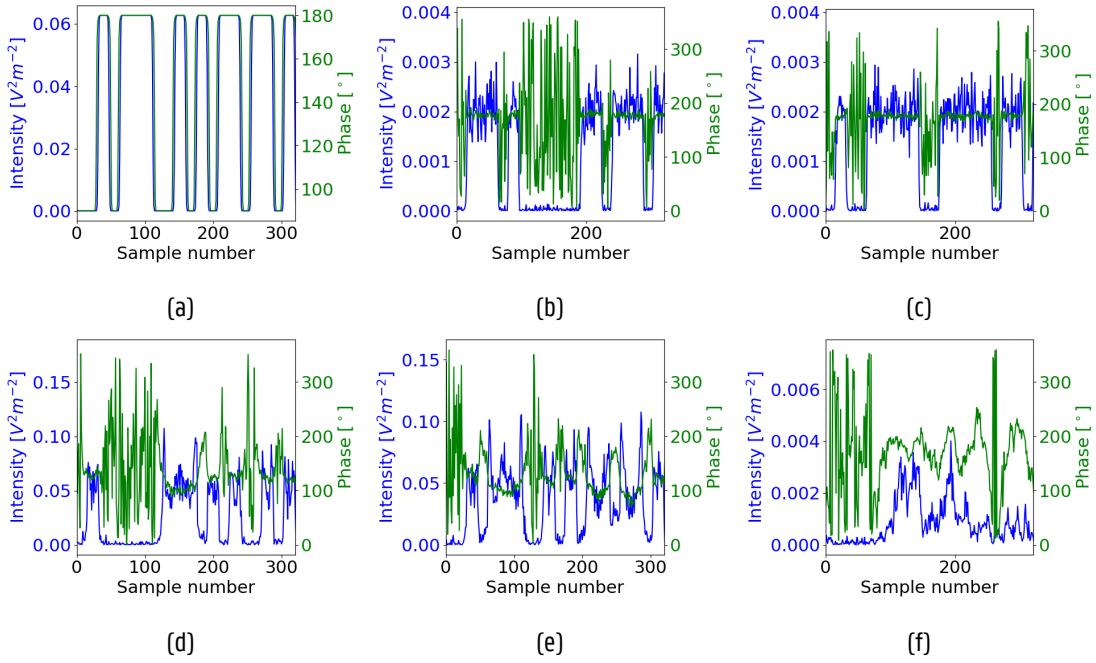


Figure 4.2: Signals generated by 6 different configurations of setup parameters summarized in Table 4.2. In all of them, intensity and phase of light at constant sampling intervals are depcited. The phase appears constant in the 'on' state because the lower sampling rate leads to plotting the baseband representation of the optical carrier, where high-frequency oscillations are not visible. In the 'off' state, the phase is shown as zero because it is undefined in the absence of the carrier signal.

| Figure | Chromatic dispersion compensation | Signal power | Amplifier noise |
|---|---|---|---|
| **a** | Ideal signal | | |
| **b** | Yes | 3 dBm | No |
| **c** | Yes | 3 dBm | Yes |
| **d** | Yes | 18 dBm | No |
| **e** | Yes | 18 dBm | Yes |
| **f** | No | 3 dBm | No |

Table 4.2: Configurations used by the transmission setup to generate the simulation signals.

Looking at the figures above, it is worth noting that, except for the signal with chromatic dispersion, the 'on' and 'off' states of the signal, representing logical '1' and '0' respectively, can be identified by observing the intensities. Additionally, for the 'on' states the phase shows partial coherence, i.e. there is some correlation between phase values of nearby bits. These two observations indicate that the study performed for the ideal case might hold, yet with more noisy results. As shown in the theoretical study, the case where two consecutive 'ones' are found

is the critical point that has to be tuned. Hence, if both bit intensities stay bounded over the average intensity of the 'off' state, and the phase error is lower than the theoretical limit shown before (56.79°), the separability condition should be achievable in most of the cases. To better visualize these observations, a boxplot analysis of the different signal states has been carried out, as shown in Figures 4.3 and 4.4, which represent intensity and phase, respectively. The orange line represents the average value, the box limits denote the first and third quartiles (the 25th and 75th percentiles), and the bottom and top whiskers represent the 5th and 95th percentiles, respectively.

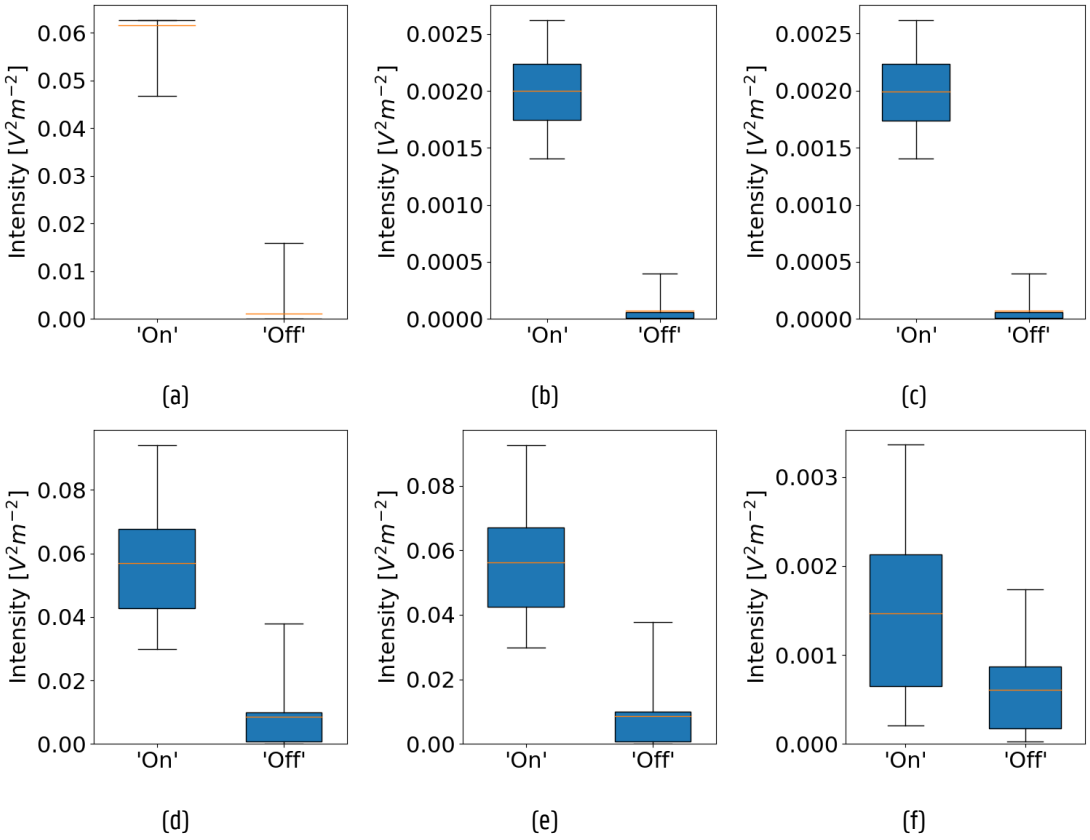


Figure 4.3: Boxplot representing the intensity of the 'On' state (when a logic '1' is transmitted) and the 'Off' state (when a logic '0' is transmitted) from the signals indicated in Table 4.2.

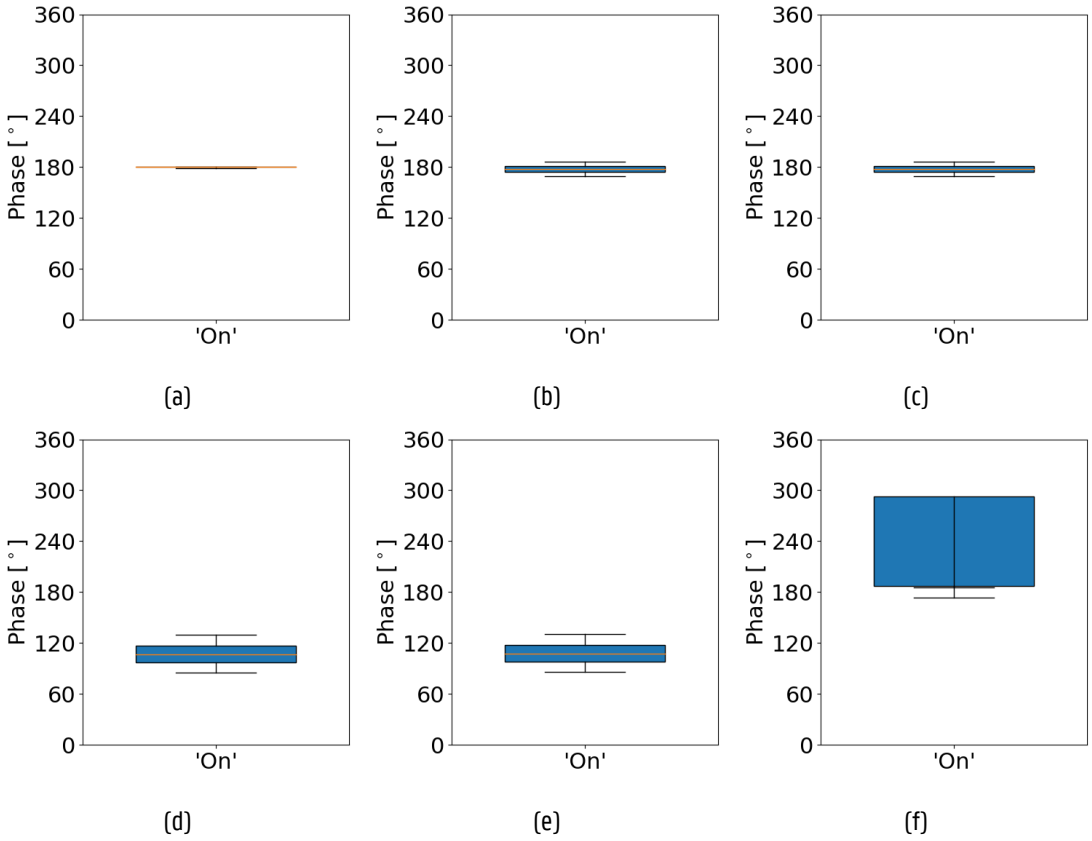


Figure 4.4: Boxplot representing the phase of the 'On' state (when a logic '1' is transmitted) from the signals indicated in Table 4.2. Only this case is relevant because the interactions between consecutive bits is the most important for the theoretical study.

Observing the statistics shown in the figures above reinforces the previously stated hypothesis. When no chromatic dispersion is involved, the average intensity of the 'on' state remains higher than the intensity of the 'off' state with a high probability, as evidenced by the clear separation between their respective boxplots. Additionally, the phase value of the 'on' state remains mostly constrained within a range lower than the threshold determined in the theoretical study (phase tolerance of $56.79°$), suggesting that the coherence should be sufficient for the system to operate as expected in most cases. However, in the presence of chromatic dispersion, the intensity variation may cause the 'on' and 'off' states to overlap, indicating that the theoretical approach with two nodes might not be sufficient to achieve optimal performance.

## 4.3 Simulation experiments

When we refer to the concept of "experiment," we mean the set of simulations conducted with various phase shifter configurations used to compute the XOR between consecutive bits for a specific source signal and circuit

setup. In this project, as it was mentioned several times, such parameters correspond to the values of the phase shifters. To study their effect through simulations, we can either find the optimal configuration that provides for the best posible outcome, or analyze the response and sensitivity of the circuit to the parameter variation.

The former is a good option for identifying whether the problem is indeed solvable with the designed complexity. This could be achieved using a two-step optimization procedure based on black-box optimization algorithms, like the one described in Section 3.1. However, since we proved a general solution in the previous chapter that works for cases without chromatic dispersion—and in a more interpretable way—this approach may not be as compelling.

Regarding the latter, sweeping over all the parameters to analyze the response of the circuit could provide intuition about the sensitivity of the circuit to these variations. However, the parameters of the network have continuous values that range from $0$ to $2\pi$, so testing all the cases is obviously impossible. A way of fixing this issue could be discretizing the space of values and just evaluating the model in an equispaced limited set (e. g. for 36 values, the set would look like $\{0, \frac{1}{36}2\pi, \frac{2}{36}2\pi, \ldots, \frac{35}{36}2\pi\}$). In this case, there would still be an issue; the space of configuration parameters scales exponentially with the number of phase shifters. In other words, if we consider that every phase shifter has 36 possible values, when n phase shifters are used, there would be $36^n$ possible states of the circuit. This is untractable to simulate, analyze, visualize or anything related to the purpose of the parameter sweep for almost any n because the simulations are not parallelizable, so it seems not to be a good option neither. However, again referring to the theoretical analysis, we saw that using two nodes, a solution to the problem could be achieved. Hence, just using two nodes as input and sweeping the parameters directly related to the studied interactions could give a very good image of how the circuit is performing. The effect of the rest of the circuit and its recurrency in terms of pure performance could be analyzed in a more coarse way with a Monte Carlo approach, by trying different seeds for every experiment. Using enough seeds could give an approximation of the general response without the need of trying all the configurations.

Table 4.3 summarizes the most important parameters used in the experiments corresponding to the vanilla 2x2 reservoir architecture, though some parameters may vary depending on the specific setup. Following the minimum complexity criteria discussed in Chapter 3, only nodes 0 and 1 from Figure 3.3 are used to input the bitstream into the reservoir, and only phase shifters 0 and 1 are evaluated. Thirty-six values per phase shifter is considered to provide sufficient reliability and resolution while keeping computation time tractable, resulting in 1296 simulations per seed. The error values are visualized using a heatmap, offering a clear representation of performance across all parameter configurations. Both multi-seed and single-seed experiments are conducted to evaluate different architectures and scenarios.

Additionally, the inclusion of non-volatile phase shifters, as opposed to regular phase shifters, is assessed in every experiment. The implications and limitations of using this technology are discussed in the subsequent sections.

| Parameter | Value |
|---|---|
| Dimensions | 2x2 |
| Input nodes | 0 and 1 |
| $n_{eff}$ | 2.498 |
| $n_g$ | 4.088 |
| Waveguide loss | 2 dB/cm |
| MMI insertion loss | 2 dB |
| Interconnection delay | 1 bit period |
| Values per phase shifter | 36 |
| Tunnable phase shifters | 0 and 1 |

Table 4.3: General reservoir parameters used in the simulations.

## 4.4 Experiments pipeline

The parameter sweep process is outlined in Algorithm 1. The maximum number of iterations is set to 1296, corresponding to all possible combinations of the selected phase shifters. The evaluation function uses the bit error rate (BER), which measures the percentage of bits incorrectly computed out of the total number of bits assessed.

To optimize the readout weights for computing the XOR in each circuit configuration and evaluate performance using the BER, three datasets are utilized: training ($\mathcal{D}$train), validation ($\mathcal{D}$val), and test ($\mathcal{D}$test). Each dataset consists of 1000 symbols generated from one of the source signals listed in Table 4.2, along with their corresponding target labels, which are calculated as the XOR between consecutive bits of the bitstream. Each dataset is structured as $\mathcal{D} = \{(x_1, x_2, \ldots, x1000), (y_1, y_2, \ldots, y_{1000})\}$.

The algorithm starts by randomly initializing the phase shifts of the circuit's interconnections, mimicking the random phase shifts observed in the actual chip due to fabrication errors. Next, the first set of values for the selected phase shifters is applied, and the $\mathcal{D}$train bitstream is propagated through the reservoir. The linear regression weights are then determined using the expression from Equation 3.4, where $X$ represents the reservoir output after propagating $\mathcal{D}$train. The BER is subsequently calculated for the $\mathcal{D}_{\text{val}}$ dataset using these weights.

The configuration of the $\beta$ and $\tau$ parameters from Equation 3.4 that yields the lowest validation error is selected to determine the final linear weights, which are recalculated using $\mathcal{D}$train. Finally, these weights are used to compute the BER for the test set ($\mathcal{D}$test), which characterizes the circuit configuration. This process is repeated

until the maximum number of iterations is reached, at which point the heatmaps are completed.

## 4.5 Single seed experiments

To optimize the use of computational resources, initial experiments using a single seed were conducte, which helps to filter out experiments that do not provide additional insights about the reservoir system for the subsequent multi-seed experiments.

### 4.5.1 Qualitative analysis

Figure 4.5 shows the test BER heatmaps of the single-seed experiments. By examining and comparing these heatmaps, we can identify patterns and variations in the circuit's behavior, which helps in understanding the effects of different configurations and input signals.

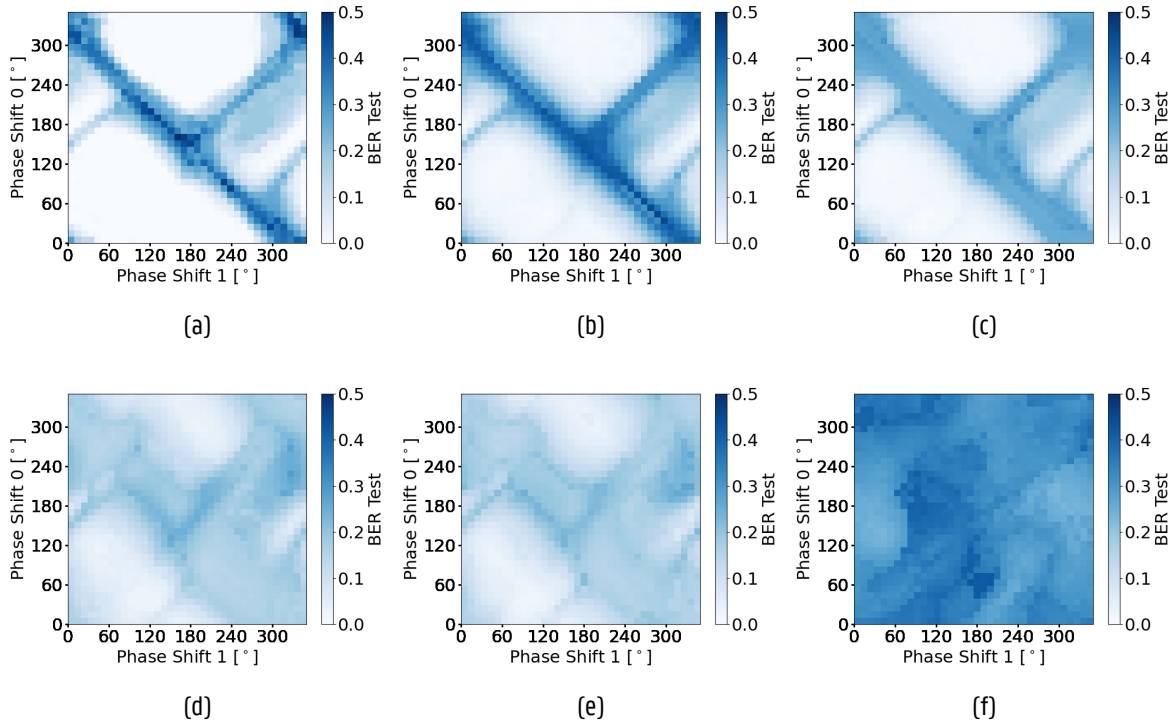


Figure 4.5: Test BER heatmaps for every experiment from table 4.2.

First, we observe that the behaviour of the system stays pretty much constant regardless of the kind of distortion present in the source except when chromatic dispersion is present, which agrees with the theoretical analysis and the evaluation of the input signals. The phase error, as long as it is mantained bounded within certain limits

and still allows some coherence between consecutive bits (specially for the case where two ones are recieved consecutively), the interactions of the network will still provide the desired outcome, the computation is feasible. Hence, the most robust configurations, which are the white points that stay furthest from the blue points, will still provide the expected behaviour. The chromatic dispersion modifies excessively the input signal, so the complexity of the network is not large enough to handle this kind of data. Nevertheless, certain improvement can still be observed.

In traditional reservoir architectures, all the phase shifts of the interconnections between nodes are completely random. Therefore, if that was the case, the heatmaps would be representing all the possible values that the circuit could obtain with respect to phase shifts in waveguides 0 and 1. This is a critical observation because it implies that the network, for this specific configuration (2x2 reservoir, input signal in nodes 0 and 1, SOI technology...), would be providing either good results or bad results, just depending on the fabrication errors. This justifies the need for configurable parameters, since modifying a small subset of variables can lead to drastic performance improvements.

Additionally, we can see that the lower the amount of distortion, the lower the minimum error, as expected. The regions of minimum error are also larger in size, making it easier to achieve optimal performance. However, in configurations where performance is not optimal, the bit error rates are lower for higher distortion signals, especially in cases of high transmission power, which is very interesting. The behavior of the reservoir is more altered by phase noise than by intensity noise, but this adds enough richness to the circuit to improve error in configurations that theoretically would not calculate the XOR well, which is a positive outcome. Thus, if the interconnections were completely random, certain signals might be preferred over those with lower distortions, because the average outcome might show lower error and have less variance. Even if performance is not optimal, we could ensure generally better performance with higher tolerance for error. In contrast, with configurable parameters, less noisy signals are preferred, as the risk of falling into regions of poor performance is minimized, and the optimal configuration achieves lower error.

But using tunable components could be somewhat opposite to the idea of reservoir computing, one could say. These architectures, as conceived until now, are completely random so there is no need to waste any kind of energy to carry out the task, which is one of their main advantages. In contrast, regular phase shifters require a constant electrical tension in order to fix their polarization point, so they would be continuously utilizing energy, which is an important drawback. Alternatively, using non-volatile phase shifters would overcome this problem. These devices would just need to be configured once, so the amount of electrical power needed is negligible. However, to the best of our knowledge, the number of fixed states offered by these devices is limited, which restricts the network's capabilities. In figure 4.6, we show an example of the values that a 6-state non-volatile phase shifter could provide. Ideally, 36 equidistant points would conform the space of all the states that can be configured, coming from all the combinations of two 6-state non-volatile phase shifters. The goal of this part is to check if just with a fixed amount of states, we could achieve a comparable performance to the results obtained

with traditional phase shifters. If that was the case, we would demonstrate a tunable reservoir circuit that uses almost no power. The choice of 6 states per non-volatile phase shifter was decided by convenience. This value is lower than the highest reported amount of states from non-volatile phase shifters, still high enough to give consistent results and fits well with the number of simulations done to make the splits.

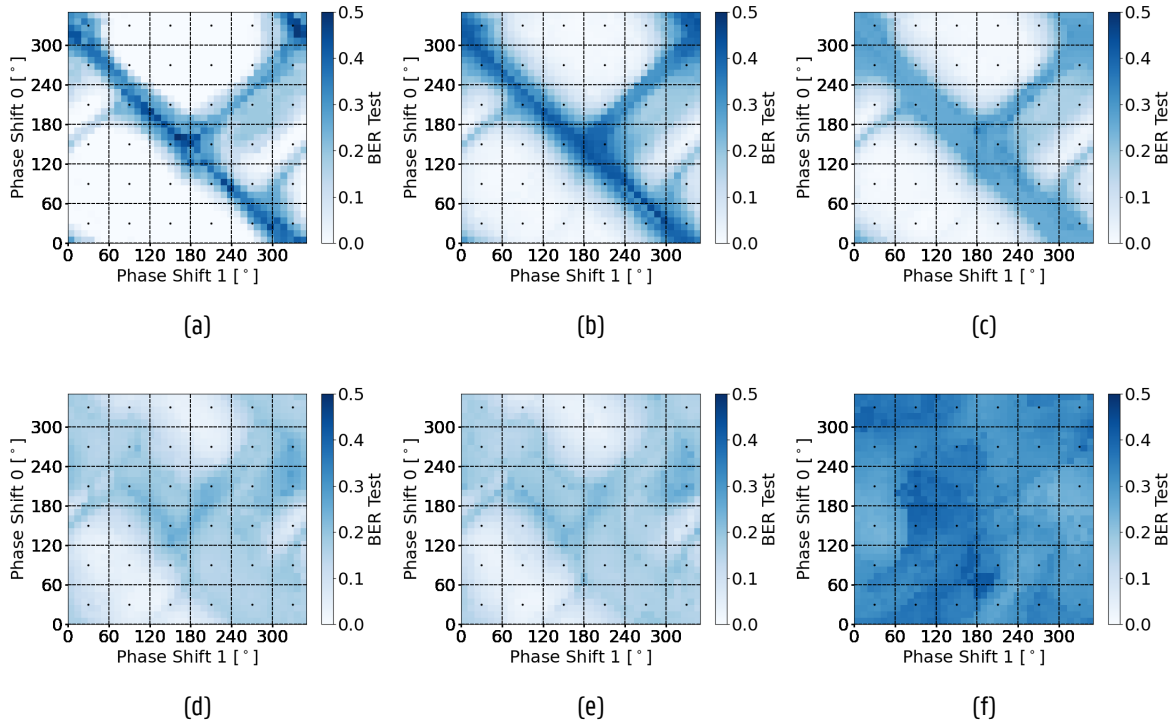


Figure 4.6: Test BER heatmaps of reservoirs with 6-state non-volatile phase shifters for every experiment from table 4.2. Each black dot correspond to a possible configuration.

The points plotted on the heatmaps of Figure 4.6 indicate the different possible configurations of the non-volatile network. Although the results seem to be good, it is difficult to determine visually whether they depend on choosing a good starting point to build the mesh or if they are inherently consistent. Hence, to provide a reliable interpretation of the results and enable comparison between different experiments, a statistical description of the heatmaps is given in the quantitative analysis.

In this context, another debate arises about whether this architecture is the best option when phase shifters are used, since just a certain amount of interactions are needed to achieve good results. This is a large topic, so it has not been fully addressed in this thesis, but the first steps have been taken. In Figure 4.7, we observe which simulations provide the lowest error when the signal has propagated through only one cycle, i.e., when the delay of the linear regression is zero symbols ($\tau = 0$), and nodes 0, 1, and 3 are the only ones containing relevant information related to the XOR computation. The heatmaps are the same as the ones from figure 4.5,

and the red mask identify those simulations with 0 symbol delay. This implies that the optimal values might have been obtained with the interference and regression described in the theoretical analysis. However, as mentioned before, also node 3 contains useful information for the linear regression so, to make sure that these interactions indeed happen in the simulations, Figure 4.8 shows two low-error examples extracted from red regions.

In these heatmaps, we can also observe that other regions that do not correspond to the first cycle offer good results. This means that the additional complexity (nodes) improves the average performance of the model. This may not be so relevant in case of using common phase shifters, but if a completely random architecture or non-volatile phase shifters are used, this can make a difference, since having more regions with low error, will make the system to perform better. However, it is not clear that recurrence is necessary for this problem when chromatic dispersion is not present. In that case, not so much memory is needed, only the information from two bits, so considering information from instants before may not be the best option. This is explored in the multi-seed experiments.

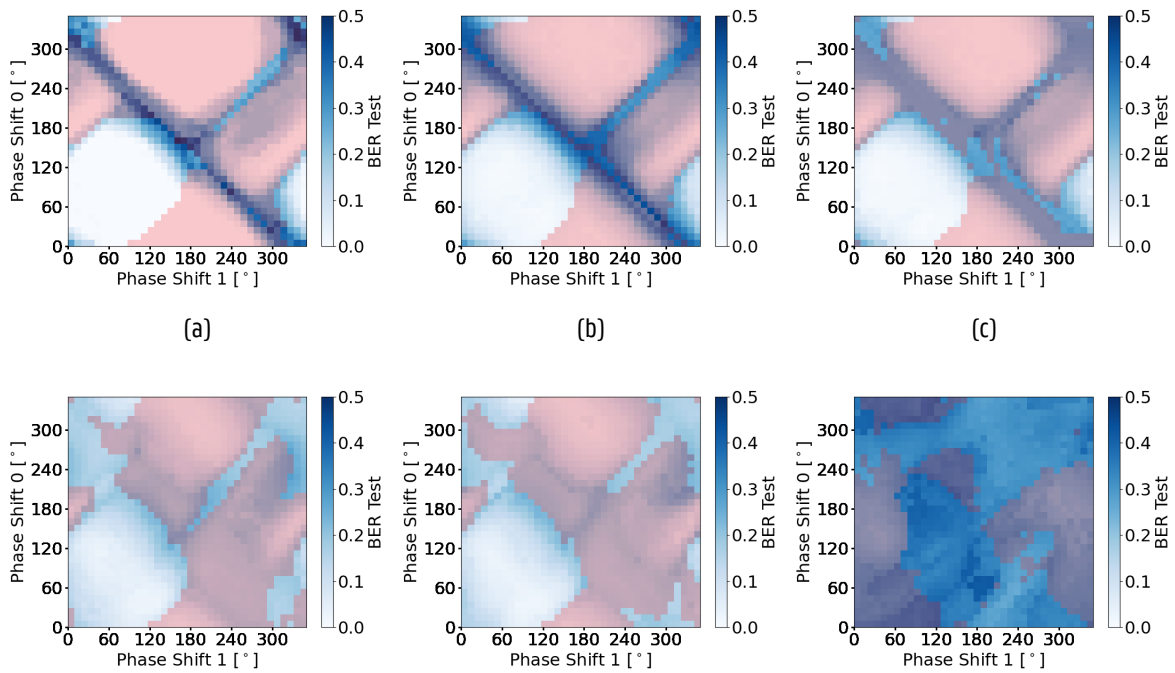


Figure 4.7: Masked test BER heatmaps for every experiment from table 4.2.

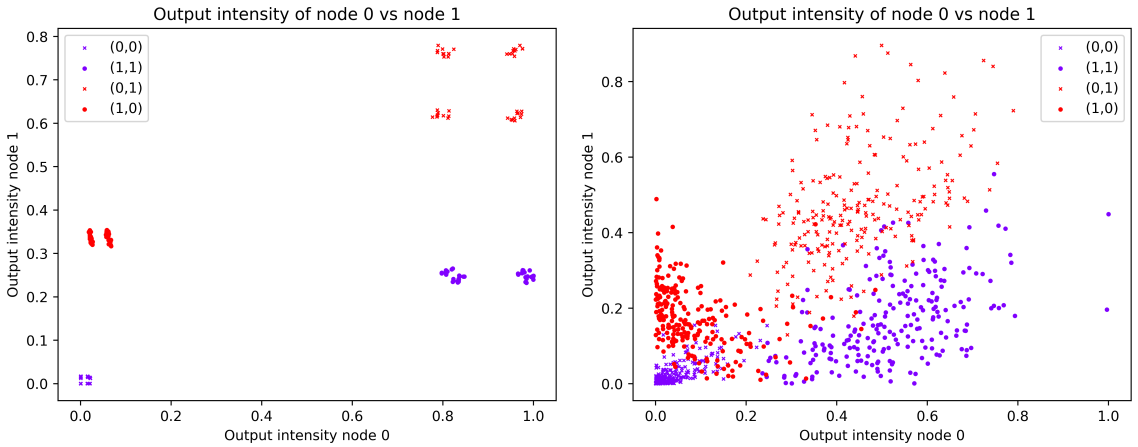


(a) (b)

Figure 4.8: Output normalized intenisty of nodes 0 and 1 with respect to each other. It is possible to observe that the separability condition shown in Figure 3.6 (mostly) holds for both ideal (a) and noisy (b) experiments for the same phase shifter configuration. Note that in (a), using only the output from node 1 could allow for the separation of the two classes, meaning that the computation would occur entirely in the optical domain.

To examine how these low-error configurations perform the XOR computation, Figure 4.8 shows both the predicted and target values from the reservoir over a specific time interval for the two simulations depicted in Figure 4.9.

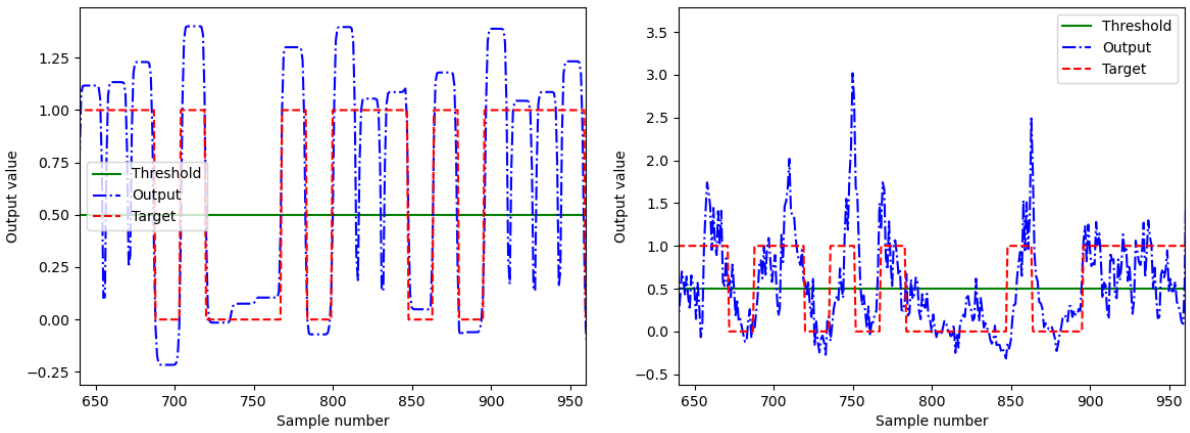


(a) (b)

Figure 4.9: Prediction of the XOR by the reservoir system and its target. (a) and (b) correspond to the same simulations from Figure 4.8

### 4.5.2 Quantitative analysis

Table 4.4 and Table 4.5 offer typical relevant statistic metrics about the experiments like maximum or minimum value, error average and standard deviation as well as some custom metrics that were found to be very explanatory. The metrics column refers to the metrics used to analyze the whole heatmaps. The quantized metrics column refers to the metrics used to analyze the dezimated heatmaps (with 6-state non-volatile phase shifters). In this last one, to improve the robustness of the results, the values shown have been obtained doing the mean and standard deviations for all the possible equispaced meshes of points, depending on the offset position of the first point (if it is in the center, in the corner...). Therefore, 36 different cases were considered.

Regarding the custom metrics, the ratio measures the quotient between the maximum and minimum error values, while the effective ratio compares the minimum value with the rest of the values in the heatmap, and extracts statistics from these ratios. This allows, on the one hand, to observe the maximum gain that can be obtained in the circuit and, on the other hand, to analyze on average how much the network improves when using this type of configurable parameters.

| **Experiment** | **Metrics** | | | | |
|---|---|---|---|---|---|
| | **Error** | **Worst** | **Best** | **Ratio** | **Effective ratio** |
| **a** | $0.1064 \pm 0.1272$ | 0.4880 | 0.0 | inf | inf |
| **b** | $0.1543 \pm 0.1308$ | 0.4560 | 0.0021 | 215.0 | $72.8082 \pm 61.6737$ |
| **c** | $0.1326 \pm 0.1017$ | 0.3464 | 0.0011 | 326.6535 | $125.1353 \pm 95.8403$ |
| **d** | $0.1417 \pm 0.0570$ | 0.2821 | 0.0244 | 11.5652 | $5.8138 \pm 2.3331$ |
| **e** | $0.1393 \pm 0.0552$ | 0.2712 | 0.0201 | 13.4594 | $6.9178 \pm 2.7346$ |
| **f** | $0.3218 \pm 0.0406$ | 0.4252 | 0.2309 | 1.8414 | $1.3939 \pm 0.1754$ |

Table 4.4: Metrics quantifying the performance of the reservoir architecture for the different signals shown in Table 4.2.

| Experiment | Quantized metrics | | | |
|---|---|---|---|---|
| | Worst | Best | Ratio | Effective ratio |
| **a** | $0.4020 \pm 0.0539$ | $0.0 \pm 0.0$ | inf | inf |
| **b** | $0.4089 \pm 0.0218$ | $0.0064 \pm 0.0022$ | $73.8673 \pm 32.9528$ | $28.4067 \pm 28.1531$ |
| **c** | $0.2917 \pm 0.0143$ | $0.0058 \pm 0.0021$ | $69.3732 \pm 63.7417$ | $32.3869 \pm 43.6101$ |
| **d** | $0.2422 \pm 0.0141$ | $0.0325 \pm 0.0042$ | $7.5776 \pm 1.0645$ | $4.5330 \pm 1.8245$ |
| **e** | $0.2346 \pm 0.014$ | $0.0300 \pm 0.0056$ | $8.1367 \pm 1.7966$ | $4.9265 \pm 2.1058$ |
| **f** | $0.4061 \pm 0.0103$ | $0.2411 \pm 0.0065$ | $1.6859 \pm 0.0629$ | $1.3455 \pm 0.1655$ |

Table 4.5: Quantized metrics quantifying the performance of the reservoir architecture for the different signals shown in Table 4.2.

First, we will focus on the metrics of the complete heatmaps presented in the tables above. The qualitative description provided earlier is corroborated by these statistics. High-error regions across the experiments are evident from the worst configurations in each case. Less distorted signals generally result in lower minimum bit error rates, but this does not always translate to better average performance. In fact, while the mean error rates are similar, the variance is higher, which is undesirable. As observed earlier, the worst-case errors are significantly higher for less distorted signals, but their best-case errors are lower. The ratio and effective ratio metrics demonstrate that parameter tuning provides substantial gains in all cases except when chromatic dispersion is present, underscoring the importance of having configurable parameters. Moreover, this gain is more pronounced in signals with lower distortion, as the performance gap between well-performing and poorly-performing configurations is greater compared to more distorted signals.

Then, focusing on the metrics when non-volatile phase shifters are considered, the results look very promising. It is expected that the worst case would be better than the largest overall error because 36 values are being averaged. However, the most remarkable feature of this section is the mean error and standard deviation of the best-case scenario. In all experiments, the mean is very close to the overall minimum value obtained with the full heat map and also shows a low variance. Moreover, the ratio and the effective ratio, although both are lower than the previous case, still give a high performance in all experiments, which is enough to justify the use of this type of phase shifters. We will see in the next section that these conclusions (do not) hold in the case of multiple seeds.

## 4.6 Multiple-seed experiments

To consistently evaluate the reservoir architecture studied in this project and its variations, several experiments were conducted. Each experiment used five different seeds for initializing the reservoir's tunable parameters,

while maintaining consistency across experiments, resulting in a total of 6480 simulations per experiment. A summary of these multiple-seed experiments is presented in Table 4.6.

| Experiment | Setup | | | Signal | | |
|---|---|---|---|---|---|---|
| | Circuit size | Input signal nodes | Tunnable | Chromatic dispersion compensation | Signal power | Amplifier noise |
| 1 | 2x2 | [0,1] | Yes | Ideal signal | | |
| 2 | | | | Yes | 18 dBm | Yes |
| 3 | | | | No | 3 dBm | No |
| 4 | 2x2 | All | Yes | Ideal signal | | |
| 5 | | | | Yes | 18 dBm | Yes |
| 6 | | | | No | 3 dBm | No |
| 7 | 2x2 | [0,1] | Yes | Ideal signal | | |
| 8 | | | | Yes | 18 dBm | Yes |
| 9 | | | | No | 3 dBm | No |
| 10 | 2x4 | All | No | Ideal signal | | |
| 11 | | | | Yes | 18 dBm | Yes |
| 12 | | | | No | 3 dBm | No |
| 13 | 2x4 | [1,2,5,6] | No | Ideal signal | | |
| 14 | | | | Yes | 18 dBm | Yes |
| 15 | | | | No | 3 dBm | No |
| 16 | 4x4 | All | No | Ideal signal | | |
| 17 | | | | Yes | 18 dBm | Yes |
| 18 | | | | No | 3 dBm | No |
| 19 | 4x4 | [5,6,9,10] | No | Ideal signal | | |
| 20 | | | | Yes | 18 dBm | Yes |
| 21 | | | | No | 3 dBm | No |

Table 4.6: Summary of the multiple-seed experiments.

We can see that, for every setup, three experiments corresponding to three kinds of signals are carried out. As it was mentioned before, the simulation of all posible phase shifter combinations implies a total of 1296 simulations, which is computationally expensive. For this reason, just the three most representative signals from the previous section were chosen: the ideal signal, the one with largest distortion without chromatic dispersion and the signal with chromatic dispersion. With these we can characterize the different setups sufficiently well and compare them with each other without the need to test all combinations.

The two new 2x2 setups consist of a network where all four nodes are used for input and a reservoir without recurrence (by removing the interconnections from node 2 to node 0). Using all four nodes as inputs increases the interaction richness but also introduces higher-intensity symbols unrelated to the XOR computation, which may be considered interference. Thus, it is important to evaluate whether this setup performs better than using only nodes 0 and 1. Regarding the absence of recurrence, as previously mentioned, it is unclear whether information from previous cycles provides useful interactions or just acts as interference, particularly when no chromatic

dispersion is present, so this aspect has also been examined in the multiple-seed experiments.

Another notable observation from Table 4.7 is the inclusion of circuits with more than four nodes. These experiments aim to determine whether a smaller tunable reservoir circuit can achieve results comparable to larger non-tunable reservoir circuits. If successful, especially with non-volatile phase shifters as tunable parameters, it would demonstrate the potential to miniaturize these architectures with minimal power consumption, which would be an impactful and promising discovery. This means that the higher order reservoirs only perform one simulation per seed, since the phase shifts of the interconnections are fixed, so the computational cost of these experiments is low. These additional architectures are depicted in figures 4.10 and 4.11.

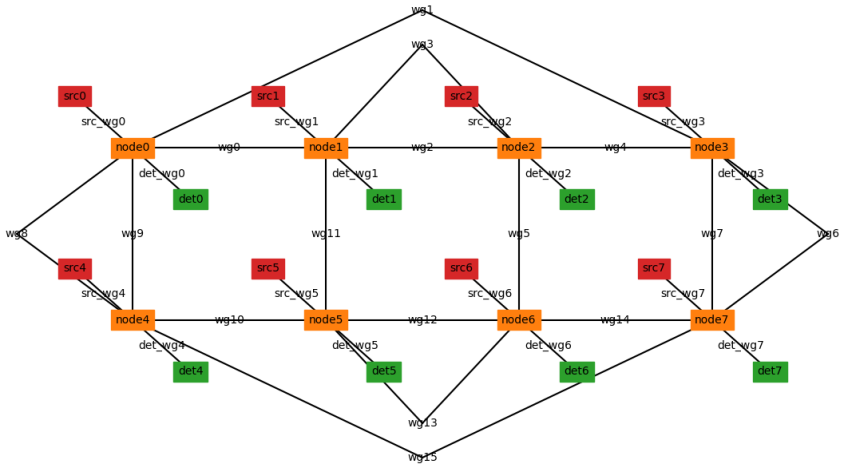


Figure 4.10: Reservoir architecture with 2x4 nodes. Automatically generated with Photontorch.

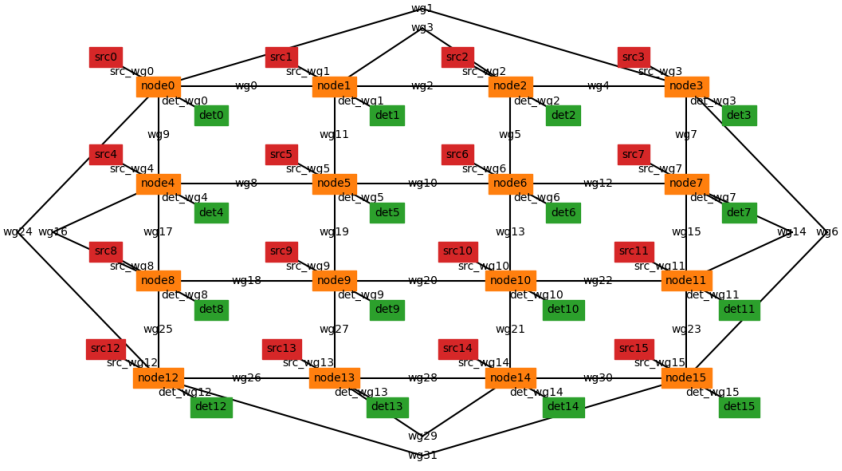


Figure 4.11: Reservoir architecture with 4x4 nodes. It corresponds to the four-port architecture. Automatically generated with Photontorch.

### 4.6.1 Qualitative analysis

This section includes all generated heatmaps and masked heatmaps from the multi-seed experiments and provides a qualitative analysis of the results. Each figure corresponds to a single experiment, representing a sweep of all possible configurations of phase shifters 0 and 1 for each seed for a specific input signal. The quantized heatmaps are only discussed in the quantitative evaluation. Their qualitative interpretation could depend on the mesh of points chosen and, therefore, lead to erroneous conclusions. The larger simulated reservoirs (2x4 and 4x4) are compared as non-tunnable devices, i.e. an error heatmap has not been generated from them, so their discussion is not included in this part either.

#### Vanilla 2x2 reservoir setup

First, the most relevant experiments from section 4.5 were repeated with multiple seeds to enable a proper statistical comparison.

Figure 4.12 shows all the conducted simulations with an ideal input signal. The results are consistent with the single-seed experiments, since the heatmaps clearly display both error-free and high error regions. Regarding the masked heatmaps, the model's behavior also remains constant. Most of the low-error regions are achieved with a symbol delay of $\tau = 0$, but in all the simulations, there is at least one low-error region achieved with a higher $\tau$, underscoring the importance of adding extra nodes to the network.

In Figure 4.13, the input signal includes amplifier noise and non-linearities caused by high input power. As happened in the single-seed experiments, the parameter configurations that yield the best results are the same as in the ideal case. The performance at the optimal phase shifter configuration is worse w.r.t. an ideal signal, while in the worst-case, the performance is better. Additionally, the phase error causes the low-error regions to shrink, limiting the capabilities of non-volatile phase shifters, but the overall performance is more stable. The masked heatmaps are also consistent with the results from Section 4.5. Similar to the ideal case, the lowest error regions are obtained with the first cycle interactions. The improvement provided by the network's additional complexity is more significant with non-ideal signals, as expected.

In Figure 4.14, the test error of the 2x2 reservoir with chromatic dispersion is depicted. None of the seeds allowed proper computation of the XOR task, reinforcing the idea that the circuit lacks the necessary complexity and memory to handle this type of problem. Moreover, the masked heatmaps indicate that achieving the best results in the first cycle is less frequent with chromatic dispersion present compared to chromatic dispersion-free signals. This highlights the even greater importance of the additional complexity in the network.

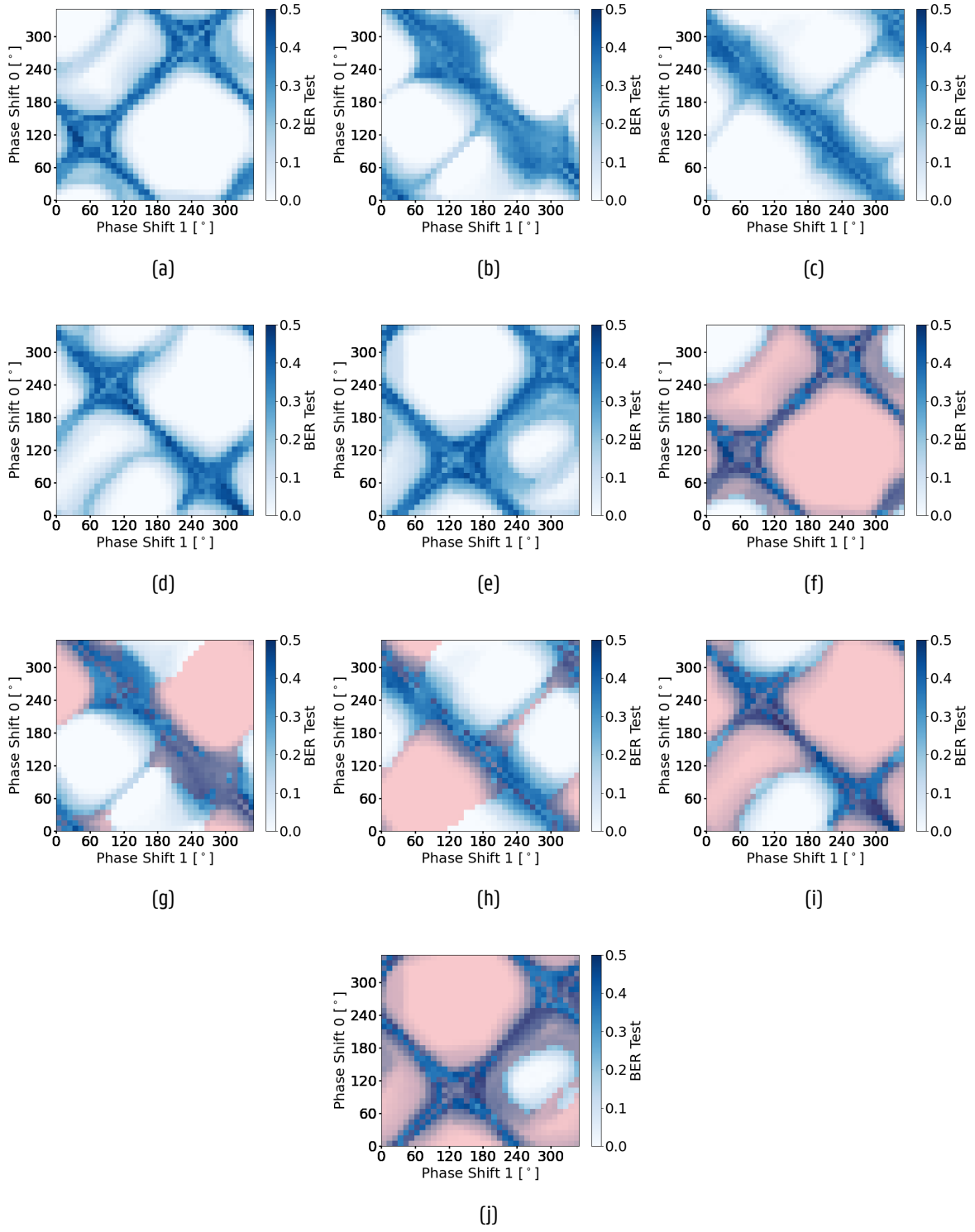


Figure 4.12: Heatmaps representing the test error of the reservoir circuit for all the configurations from phase shifters 0 and 1 with 5 different seeds - (a) to (e) - when the input signal is ideal. From (f) to (j), the masked version of the heatmaps representing the interactions happening in the first cycle of a symbol pair is shown for every seed.

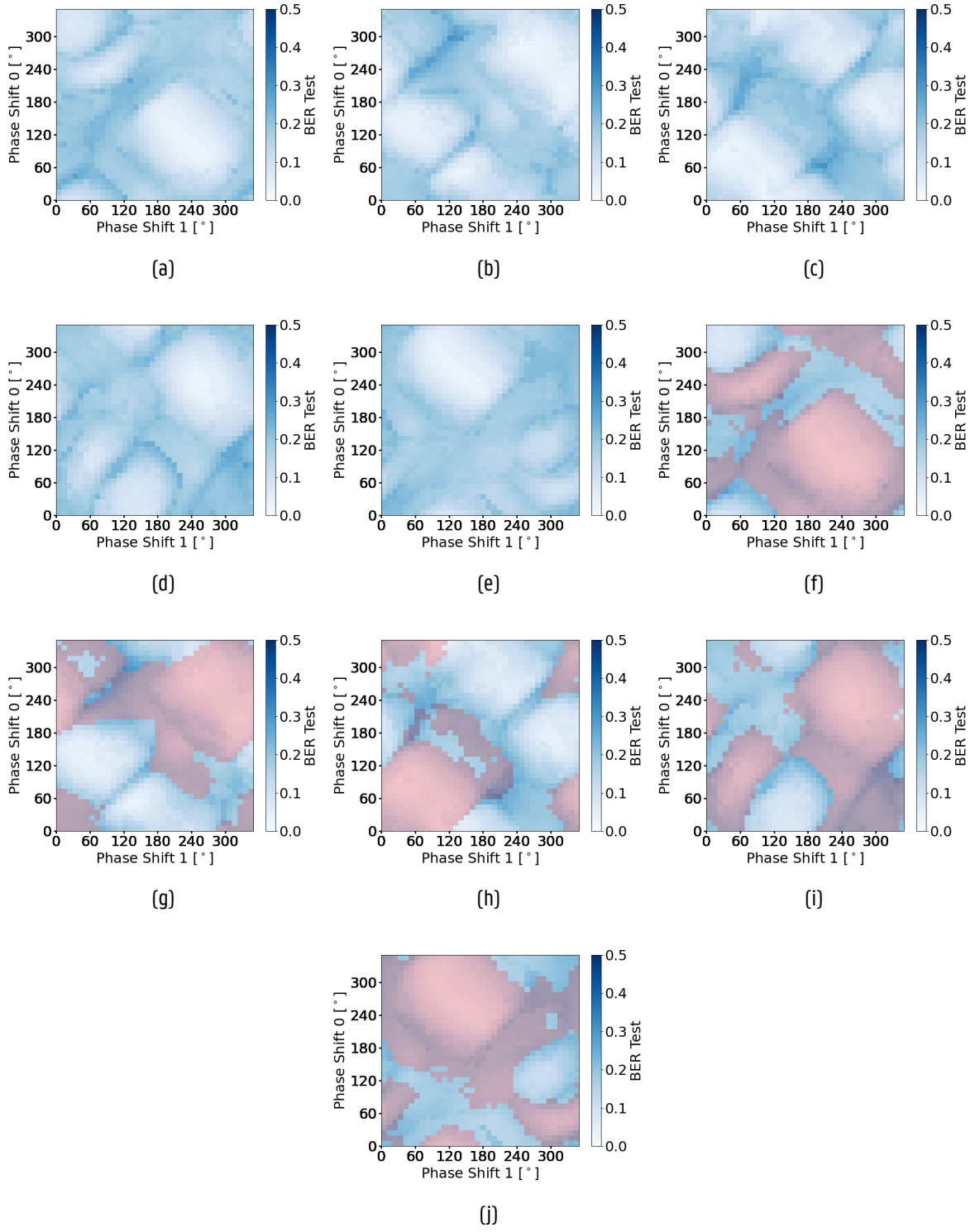


Figure 4.13: Heatmaps representing the test error of the reservoir circuit for all the configurations from phase shifters 0 and 1 with 5 different seeds - (a) to (e) - when the input signal is distorted with amplifier noise and non-linear effects caused by a high input power. From (f) to (j), the masked version of the heatmaps representing the interactions happening in the first cycle of a symbol pair is shown for every seed.

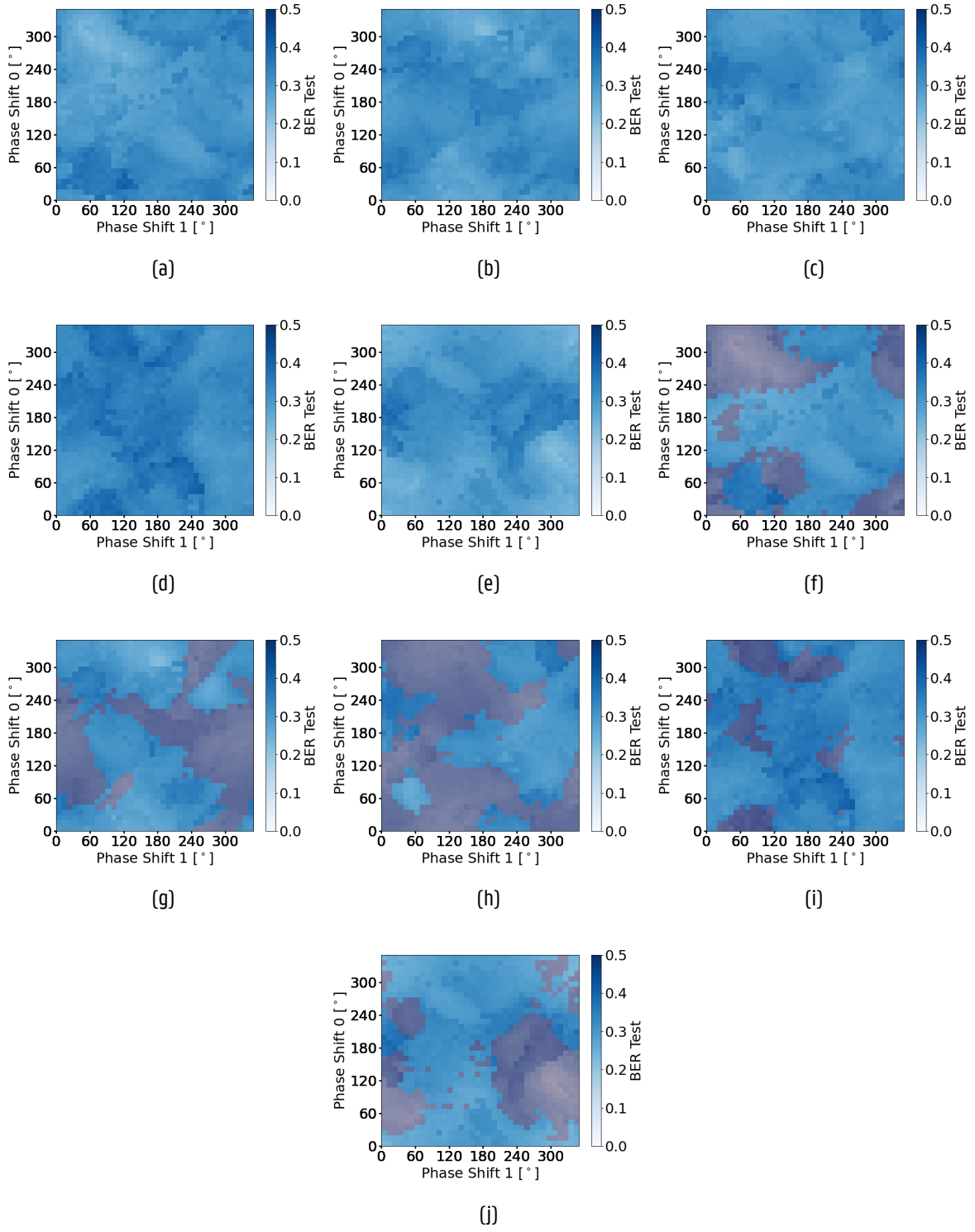


Figure 4.14: Heatmaps representing the test error of the reservoir circuit for all the configurations from phase shifters 0 and 1 with 5 different seeds - (a) to (e) - when chromatic dispersion is present in the input signal. From (f) to (j), the masked version of the heatmaps representing the interactions happening in the first cycle of a symbol pair is shown for every seed.

**All-input 2x2 reservoir setup**

Figure 4.15 shows the error heatmaps for the all-input node configuration and an ideal input signal. Compared to the vanilla case, the results show greater variability between seeds in terms of average error. This inconsistency is due to the fact that, in this case, interactions between symbols with relevant information occur in all nodes at the same time, but only one circuit arm is controlled, making the outcomes more dependent on initialization, which is undesirable.

Using all four nodes as input emphasizes the importance of first-cycle interactions, as shown in the masked heatmaps. These interactions, which previously took place in one node, now occur simultaneously in four nodes, increasing the likelihood of achieving the desired response. However, this also increases the intensity of noisy interferences in subsequent cycles, reducing the chances of obtaining good results in those cases.

Figure 4.16 shows the experimental results of the four-input circuit with a signal distorted by amplifier noise and high power non-linearities. Again, the results are less consistent and the performance is worse compared to when just two nodes are used as input. Moreover, it is notable that the best performing phase shifter configurations do not correspond to the ones from the ideal case, adding to the unpredictibility of this system. Just as happend with the ideal case, the masked heatmaps reveal that for the majority of the configurations, the best performance is achieved in the first cycle interactions, i. e. when $\tau = 0$.

Figure 4.17 show the four-input node configuration for an input signal with chromatic dispersion. As well as it happens with the two-input node configuration, the task is not completely solved. The enhaced richness does not provide the necessary interactions and memory for a two phase shifter sweep to properly calculate the XOR, and it does not really improve the previous attempt. The masked heatmaps show a slightly higher relevance of the first cycle than in the two-input node case, but as the computation is not being really achieved and it is not consistent across the seeds, these results do not yield additional information about the reservoir behaviour.

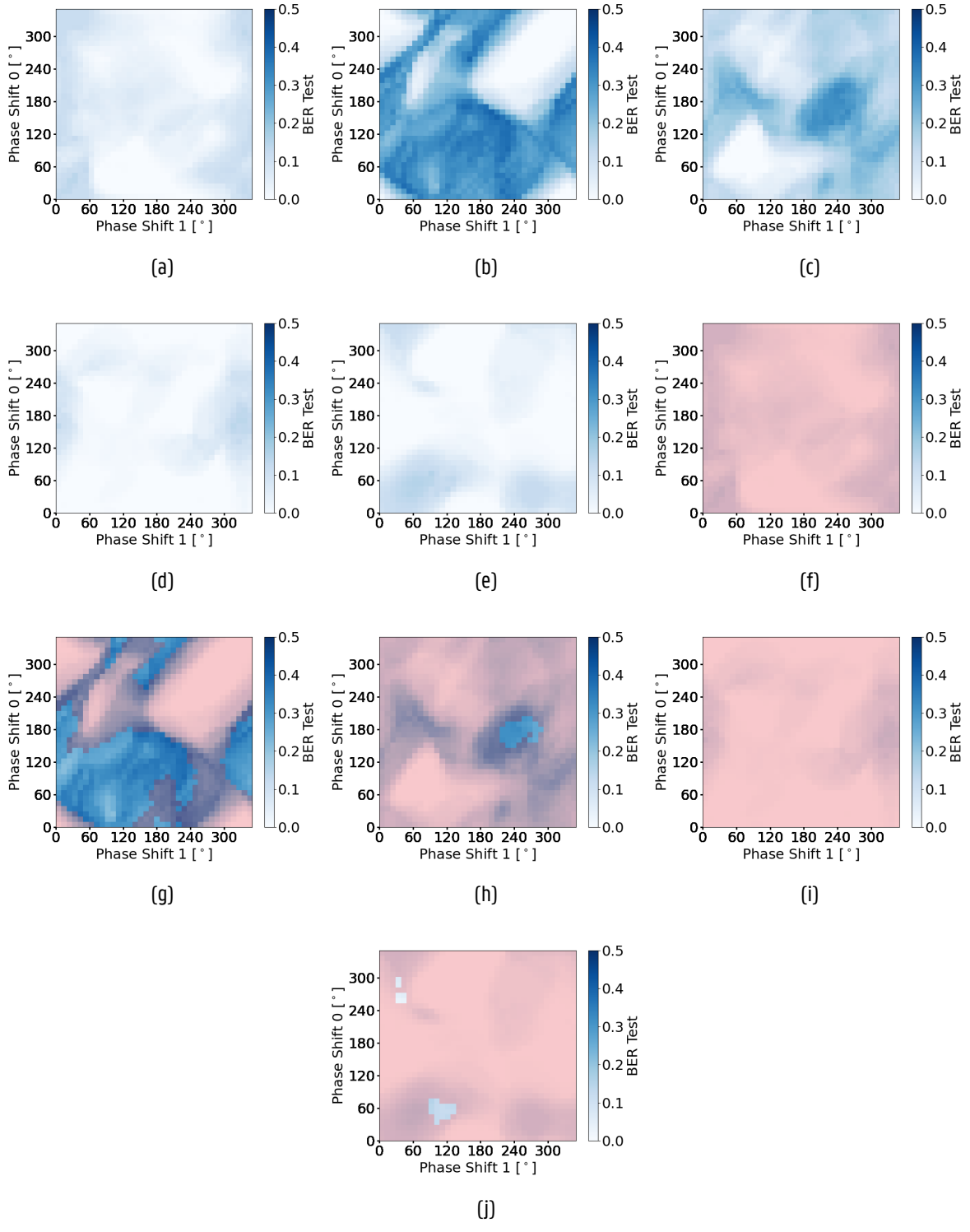


Figure 4.15: Heatmaps representing the test error of the reservoir circuit for all the configurations from phase shifters 0 and 1 with 5 different seeds - (a) to (e) - when the input signal is ideal. In this case, all for nodes as used to input the signal. From (f) to (j), the masked version of the heatmaps representing the interactions happening in the first cycle of a symbol pair is shown for every seed.

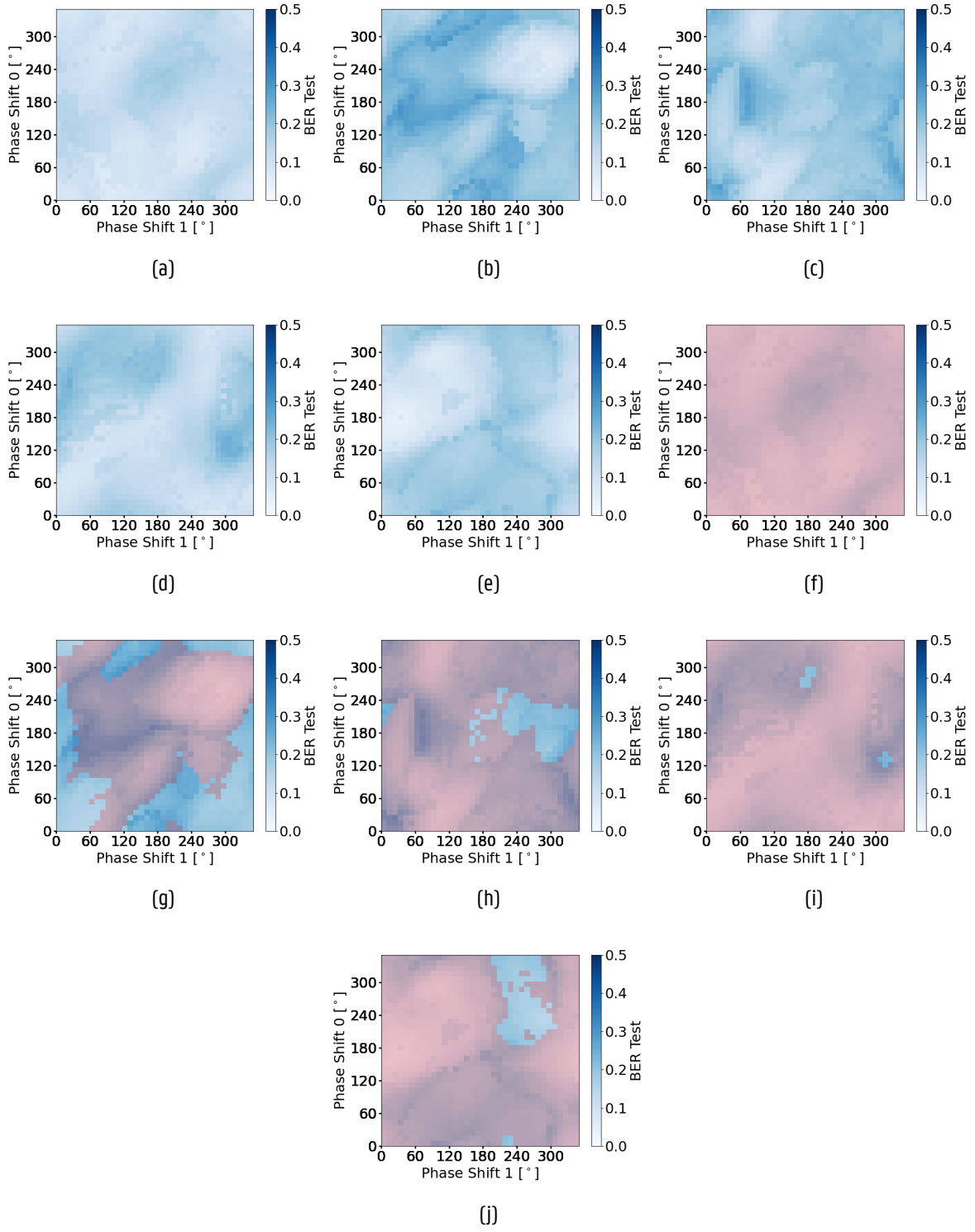


Figure 4.16: Heatmaps representing the test error of the reservoir circuit for all the configurations from phase shifters 0 and 1 with 5 different seeds - (a) to (e) - when the input signal is distorted with amplifier noise and non-linear effects caused by a high input power. In this case, all for nodes as used to input the signal. From (f) to (j), the masked version of the heatmaps representing the interactions happening in the first cycle of a symbol pair is shown for every seed.

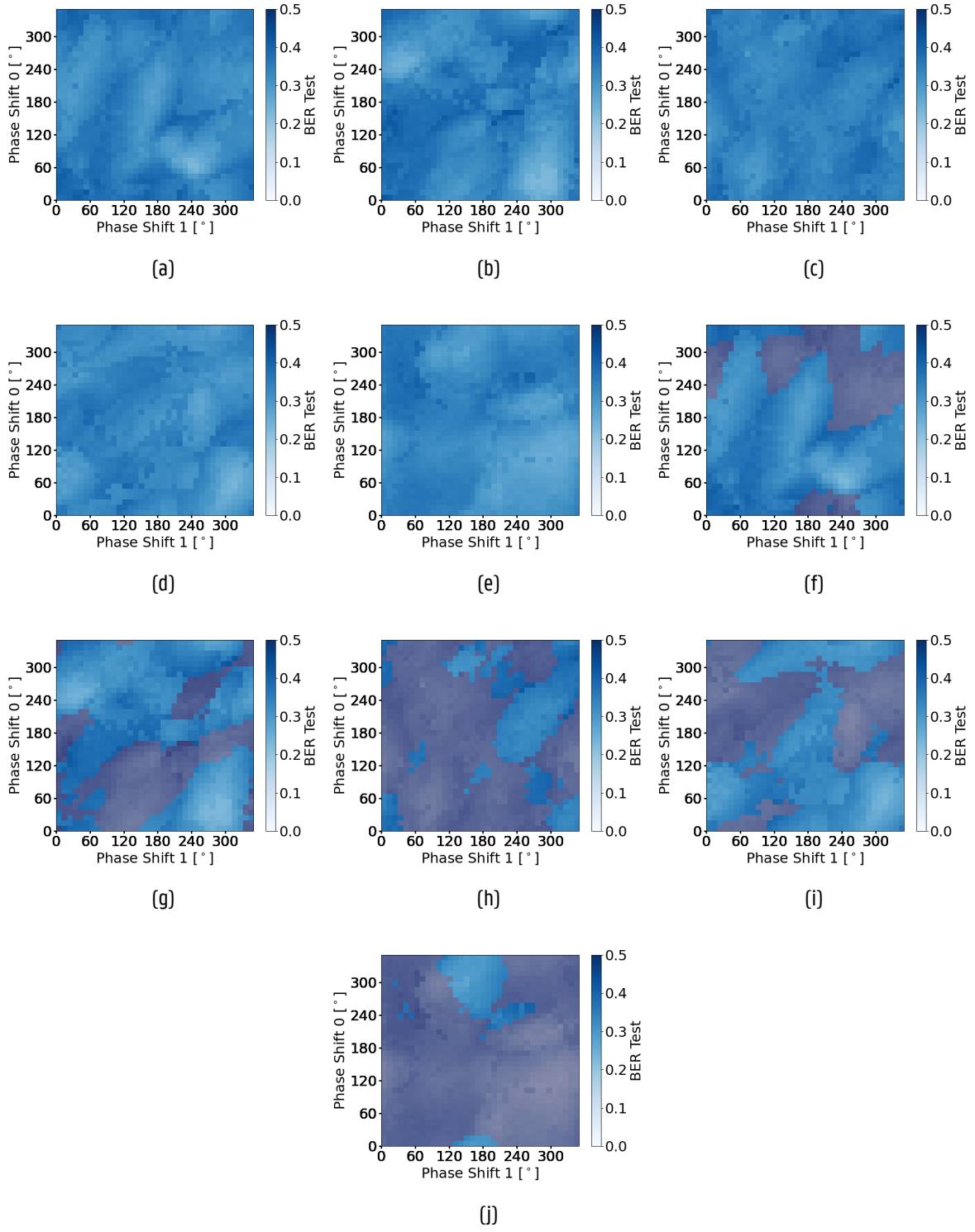


Figure 4.17: Heatmaps representing the test error of the reservoir circuit for all the configurations from phase shifters 0 and 1 with 5 different seeds - (a) to (e) - when chromatic dispersion is present in the input signal. In this case, all for nodes as used to input the signal. From (f) to (j), the masked version of the heatmaps representing the interactions happening in the first cycle of a symbol pair is shown for every seed.

**No-recurrent 2x2 reservoir setup**

Figure 4.18 shows the ideal case for a no recurrent reservoir, with nodes 0 and 1 used as input. The results greatly outperform all the previous attempts when ideal signals are considered. This demonstrates that the interactions of the symbols corresponding to the bits of interest are sufficient to compute the XOR. Information from other bits worsen the results if no intensity or pahse errors are present. Additionally, all heatmap values were achieved for a delay of $\tau = 0$, which remarks the importance of phase shifters 0 and 1 in the performance of the model. These results are the closest to the theoretical analysis that have been seen until now, since just three nodes contain useful information and no other signals from previous symbols are interfering.

Figure 4.19 depicts the same no-recurrent circuit configuration, but the input signal is distorted by amplifier noise and high power non-linearities. In contrast to the ideal case, when these distortions are present, not having recurrency degrades the performance compared to when recurrency is considered. The optimal phase shifter configurations provide a higher test error, and the regions where these can be found are smaller. Now, the maximum delay $\tau$ that we implement in linear regression is limited to 3 symbols because the signal is not travelling further than that, so it is consistent that most of the best error results are colored in red in the masked heatmaps.

Figure 4.20 represents the no-recurrent circuit with an input signal with chromatic dispersion. The performance is the worse among all the cases where chromatic dispersion is considered. Chromatic dispersion expands the pulses in the time dimension, so it makes sense that the circuit does not perform well when the available memory is not large enough to cover the entire expanded pulse. However, we have seen that including recurrence does not solve the problem completely either, so right now the issue is more in the number of nodes than in the way they are interconnected. This does not imply that the best solution requires recurrence, but with this setup has not been possible to obtain conclusive results. Regarding the masked heatmaps, as it happens every time that there is chromatic dispersion, the circuit lacks complexity to obtain good results, so they do not provide useful information.

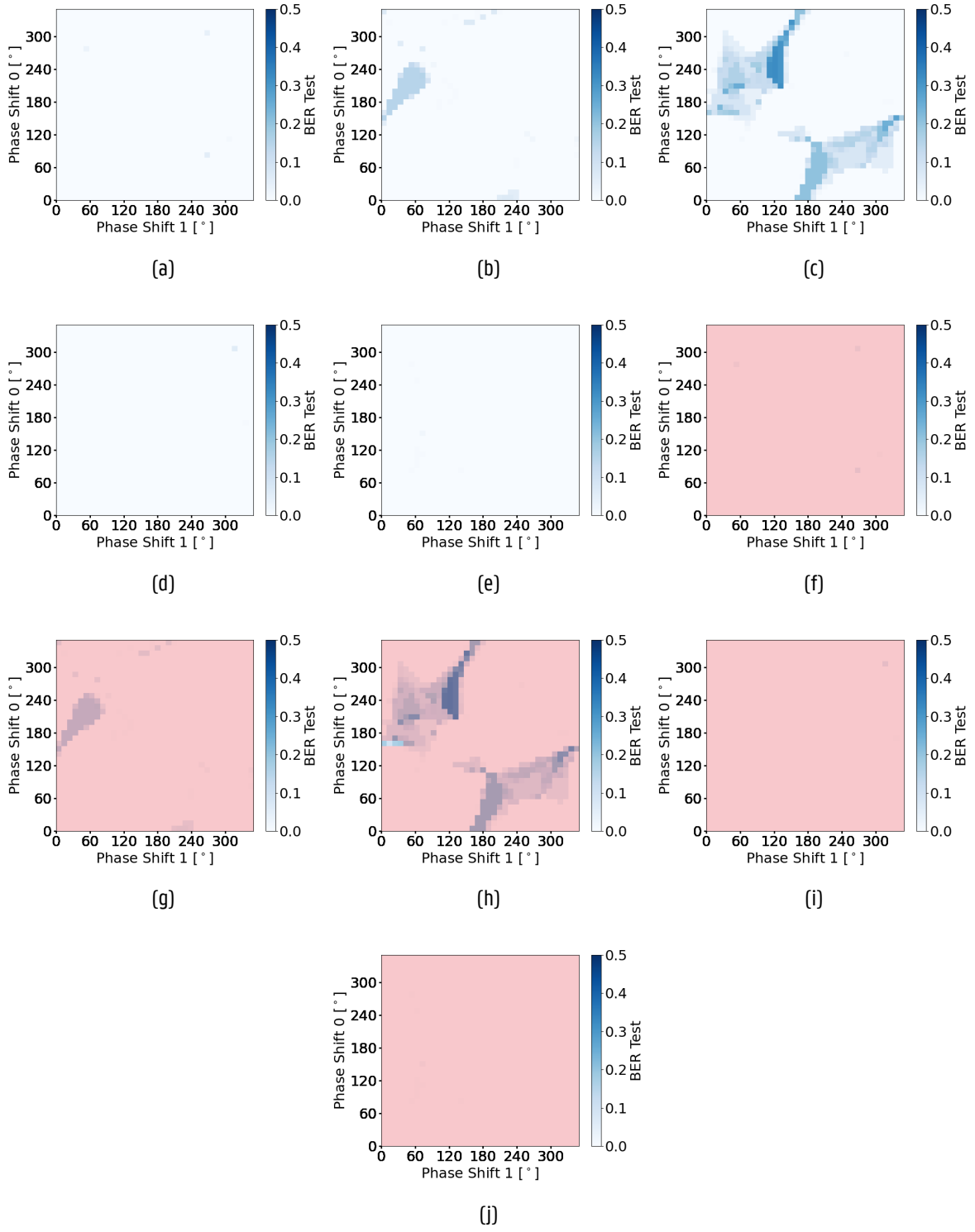


Figure 4.18: Heatmaps representing the test error of the reservoir circuit for all the configurations from phase shifters 0 and 1 with 5 different seeds - (a) to (e) - when the input signal is ideal. In this configuration the recurrency is disabled. From (f) to (j), the masked version of the heatmaps representing the interactions happening in the first cycle of a symbol pair is shown for every seed.

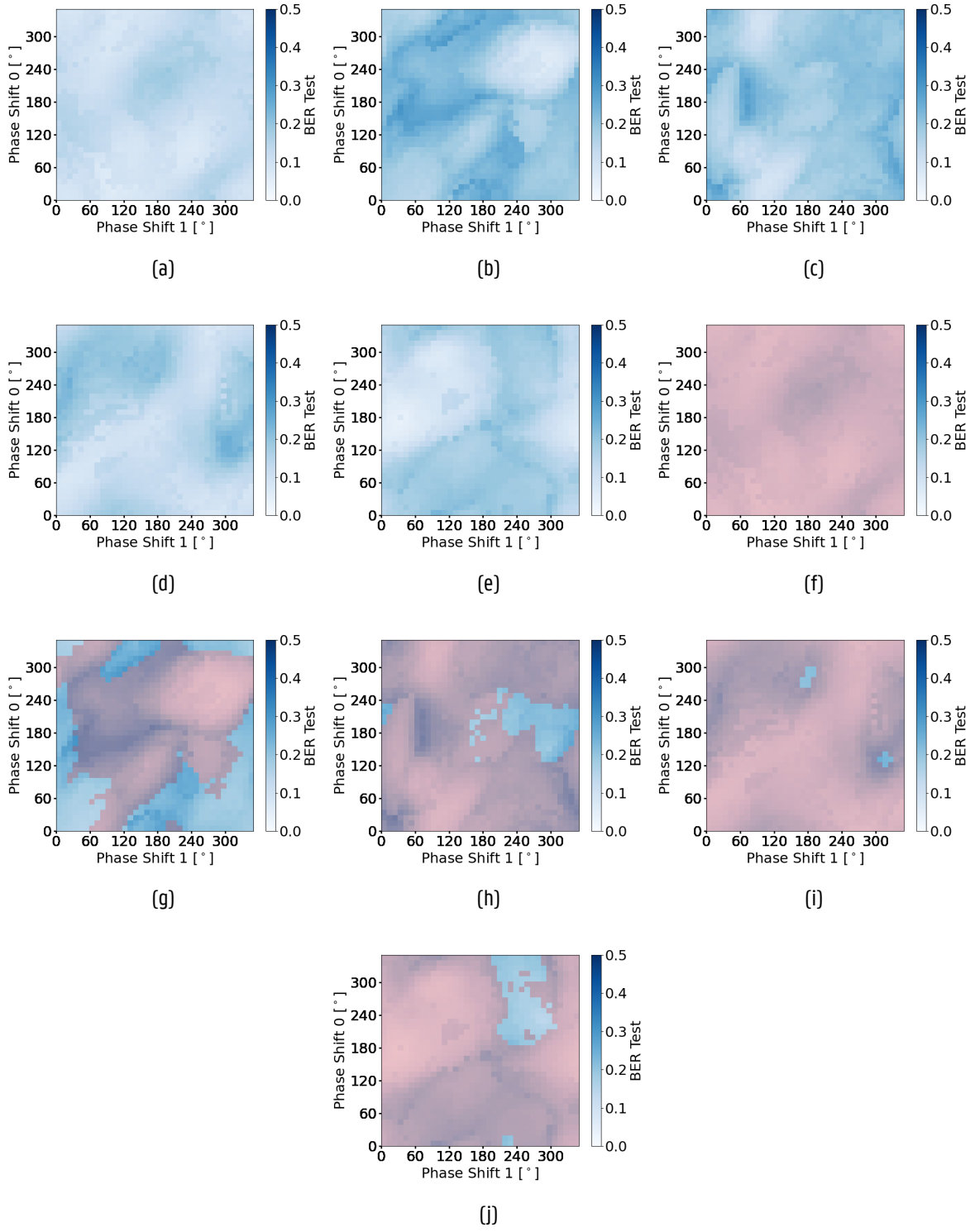


Figure 4.19: Heatmaps representing the test error of the reservoir circuit for all the configurations from phase shifters 0 and 1 with 5 different seeds - (a) to (e) - when the input signal is distorted with amplifier noise and non-linear effects caused by a high input power. In this configuration the recurrency is disabled. From (f) to (j), the masked version of the heatmaps representing the interactions happening in the first cycle of a symbol pair is shown for every seed.

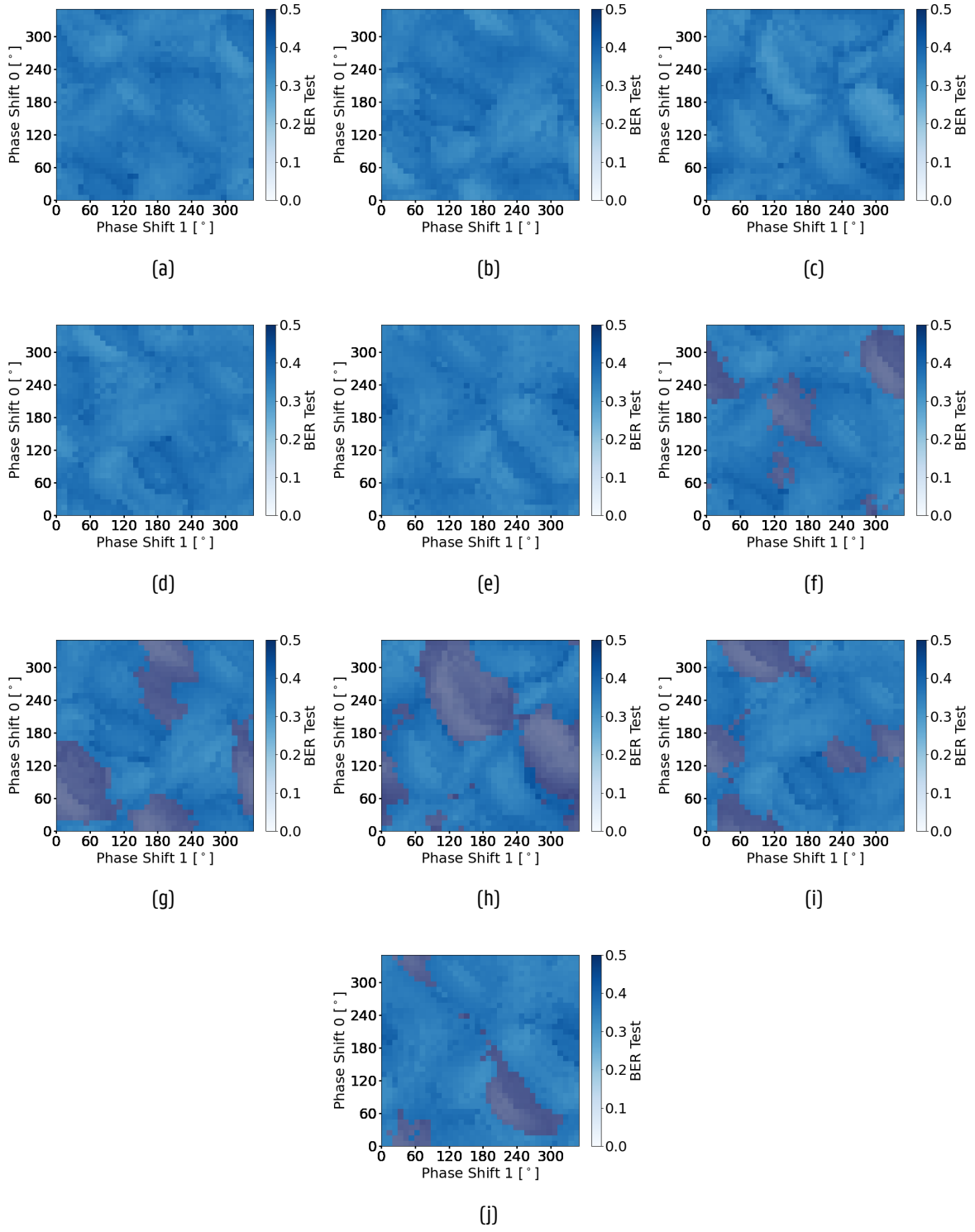


Figure 4.20: Heatmaps representing the test error of the reservoir circuit for all the configurations from phase shifters 0 and 1 with 5 different seeds - (a) to (e) - when chromatic dispersion is present in the input signal. In this configuration the recurrency is disabled. From (f) to (j), the masked version of the heatmaps representing the interactions happening in the first cycle of a symbol pair is shown for every seed.

### 4.6.2 Quantitative analysis

In this part, a quantification of the results shown in the quailtative analysis is provided along with a discussion of the results. All four blocks of experiments are covered in this study: the vanilla 2x2 reservoir, the no recurrent 2x2 reservoir, the 2x2 reservoir with all nodes as input and the higher dimensios reservoirs. Table 4.7 and Table 4.8 show the results of all the performed multi-seed experiments.

| Experiment | Metrics | | | | |
|---|---|---|---|---|---|
| | Error | Worst | Best | Ratio | Effective ratio |
| 1 | 0.1396 ± 0.1413 | 0.4547 ± 0.0168 | 0.0000 ± 0.0000 | inf | inf |
| 2 | 0.1487 ± 0.0546 | 0.2841 ± 0.0263 | 0.0250 ± 0.0026 | 11.5626 ± 2.0067 | 5.9940 ± 2.2673 |
| 3 | 0.3142 ± 0.0315 | 0.3952 ± 0.0146 | 0.2373 ± 0.0279 | 1.6842 ± 0.1707 | 1.3357 ± 0.1595 |
| 4 | 0.0934 ± 0.1026 | 0.2332 ± 0.1117 | 0.0000 ± 0.0000 | inf | inf |
| 5 | 0.1604 ± 0.0487 | 0.2547 ± 0.0386 | 0.0633 ± 0.0155 | 4.2519 ± 1.1479 | 2.6843 ± 1.0642 |
| 6 | 0.3366 ± 0.0316 | 0.4150 ± 0.0110 | 0.2453 ± 0.0240 | 1.7069 ± 0.1613 | 1.3833 ± 0.1720 |
| 7 | 0.0077 ± 0.0349 | 0.1205 ± 0.1114 | 0.0000 ± 0.0000 | inf | inf |
| 8 | 0.1399 ± 0.0587 | 0.2517 ± 0.0157 | 0.0216 ± 0.0016 | 11.7189 ± 1.2254 | 6.5182 ± 2.7904 |
| 9 | 0.3564 ± 0.0207 | 0.4252 ± 0.0079 | 0.3005 ± 0.0070 | 1.4163 ± 0.0531 | 1.1867 ± 0.0747 |
| 10 | 0.0002 ± 0.0004 | - | - | - | - |
| 11 | 0.0775 ± 0.0198 | - | - | - | - |
| 12 | 0.2744 ± 0.0335 | - | - | - | - |
| 13 | 0.0131 ± 0.0201 | - | - | - | - |
| 14 | 0.0876 ± 0.0191 | - | - | - | - |
| 15 | 0.2788 ± 0.0144 | - | - | - | - |
| 16 | 0.0000 ± 0.0000 | - | - | - | - |
| 17 | 0.0331 ± 0.0096 | - | - | - | - |
| 18 | 0.1622 ± 0.0227 | - | - | - | - |
| 19 | 0.0002 ± 0.0004 | - | - | - | - |
| 20 | 0.0806 ± 0.0222 | - | - | - | - |
| 21 | 0.1953 ± 0.0345 | - | - | - | - |

Table 4.7: Metrics from the experiments shown in Table 4.6.

| Experiment | Quantized metrics | | | |
|---|---|---|---|---|
| | Worst | Best | Ratio | Effective ratio |
| 1 | $0.4102 \pm 0.0269$ | $0.0000 \pm 0.0000$ | inf | inf |
| 2 | $0.2414 \pm 0.0193$ | $0.0350 \pm 0.0064$ | $7.1055 \pm 1.3003$ | $4.4804 \pm 1.7428$ |
| 3 | $0.3742 \pm 0.0166$ | $0.2559 \pm 0.0242$ | $1.4721 \pm 0.1219$ | $1.2409 \pm 0.1333$ |
| 4 | $0.2137 \pm 0.1077$ | $0.0001 \pm 0.0006$ | inf | inf |
| 5 | $0.2320 \pm 0.0373$ | $0.0752 \pm 0.0168$ | $3.2060 \pm 0.7609$ | $2.2540 \pm 0.7980$ |
| 6 | $0.3943 \pm 0.0146$ | $0.2648 \pm 0.0231$ | $1.5004 \pm 0.1442$ | $1.2875 \pm 0.1512$ |
| 7 | $0.0803 \pm 0.1089$ | $0.0000 \pm 0.0000$ | inf | inf |
| 8 | $0.2326 \pm 0.0211$ | $0.0289 \pm 0.0049$ | $8.2787 \pm 1.5627$ | $5.0926 \pm 2.2014$ |
| 9 | $0.4013 \pm 0.0111$ | $0.3130 \pm 0.0082$ | $1.2832 \pm 0.0553$ | $1.1432 \pm 0.0696$ |

Table 4.8: Quantized metrics from the experiments shown in Table 4.6.

**Vanilla 2x2 reservoir setup**

This block of experiments (from 1 to 3) correspond to the same ones of the single-seed experiments. Using multiple seeds, we aim to verify the conclusions obtained in the previous section with a higher robustness.

First, we can observe that, indeed, the ideal case corresponding to experiment 1 obtains the best and worst possible error values among the results from this block, both using regular and 6-state non-volatile phase shifters. Moreover, the best case from the quantized metrics is the same as the one from the complete metrics, as it happened between Table 4.4 and Table 4.5.

The second experiment provides an average error comparable to the ideal case but with less variability, as expected. This behaviour is more stable and, therefore, more suitable for fully random reservoirs and non-volatile phase shifters. The gain shown as ratio and effective ratio, although it is not as high as in the ideal case, it offers a great average improvement with respect to random reservoirs. Regarding the quantized metrics, the best performing configuration is comparable to the one from the normal metrics, which also happens with both the ratio and effective ratio.

Experiment 3, corresponding to the signal with chromatic dispersion, shows that this setup is not able to compute the XOR, the error is very high in every metric, as it was also observed during the qualitative analysis. The quantized version of the reservoir shows similar results to the regular metrics.

In general, the gain and average gain from the metrics and quantized metrics are lower compared to the single-seed experiments, but still good to justify the use of tunnable parameters in reservoir cirucits.

**All-input 2x2 reservoir setup**

This block of experiments (4 to 6) aims to determine the optimal input configuration: whether using all four nodes, which enhances interaction richness but also increases interference, or just nodes 0 and 1.

Looking at experiment 4 corresponding to an ideal signal, we can observe that the results are better for every metric and quantized metric compared to experiment 1. Specially, the average error and the worst cases outperform the vanilla setup, which prove a more consistent behaviour. Comparing the metrics and quantized metrics of this same experiment, the optimal value and ratios are very similar, as happened before for the ideal case.

Regarding the experiment 5, whose input signals show amplifier noise and high power non-linearities, we can see that now the average error is worse than in the previous setup. Moreover, both in regular and quantized metrics, the lowest error value is much higher in this case, so we can say that the general performance has dropped. The quantized metrics still stay consistent with respect to the regular ones.

In experiment 6, every single metric has worsen compared to the vanilla setup, which emphasizes the lack of complexity of this system to calculate the XOR with this kind of data. The quantized metrics remain providing similar results to the normal metrics.

**No-recurrent 2x2 reservoir setup**

Following the same idea as in the previous block, it is not clear if the additional interactions from previous signals improve the performance of the model or not. In this block (7 to 9), the recurrency of the circuit has been blocked by placing grating couplers at every output port of node 2. The feedback loop is thus broken and the signals just propagate during three cycles.

The results from the ideal case in experiment 7 greatly outperform the two previous attempts. These results have extremely low error and a consistent behaviour, both for regular and quantized metrics.

In experiment 8, the general performance is also higher than the previous setups, as can be seen looking at the error and best values. The improvement is not as high as with the ideal case but it is still notable, specially in terms of maximum and average gain (ratio and effective ratio). In this case, the effect of phase shifters, regular and non-volatile, is more important.

However, in experiment 9, the performance is the worst among all the circuits, which agrees with the observations made during the qualitative study. There is not enough memory to handle all the relevant information provided by the distorted signal.

**Higher order reservoir setups**

In this block (10 to 21), the 2x2 tunnable reservoir circuit is compared to different higher complexity configurations to verify if the "free" miniaturization is actually posible. To do so, we need to compare the average error of the high order reservoirs with the best value obtained by the 2x2 reservoir when normal and non-volatile phase shifters are used.

If we use as reference the results taken from the 2x4 reservoir, all the error values for every type of signal are worse than the vanilla case, both with regular and non-volatile parameters. When 4x4 reservoirs are considered, the experiment with chromatic dispersion presents the lowest error among all the setups, but that is not the case for the other two kinds of input signal, which occur the same as with the 2x4 reservoir.

These results are very promising and show, at least in simulations, that it is possible to halve the circuit size in all cases without loss of performance and that, depending on the problem, a reduction of up to a quarter of the circuit size could be achieved. This result is obviously not generalizable for every case and further research is needed in this line, but this first step indicate that it could be posible.

# 5

# Layout design

Designing a layout for photonic integrated circuits (PICs) involves creating a detailed plan for the physical arrangement and interconnection of various optical components, such as waveguides, modulators, detectors, and other photonic devices, on a semiconductor chip. This process includes determining the optimal placement, routing, and dimensions of these components to ensure efficient signal transmission, minimal loss, and desired functionality while considering fabrication constraints and integration with electronic components.

Specifically, this involves drawing the geometries of the components and their interconnecting waveguides, which are organized into various purpose groups (layers). These layers, when assembled, fully define the components' shapes and their relationships on the chip.

## 5.1 Description of the tools

To visualize and generate the chip layout, the IPKISS Python library was used. IPKISS is an object-oriented programming tool that defines components as parameterized hierarchical blocks, known as PCells (Parametric Cells), which can be reused multiple times.

Electromagnetic simulations to obtain further physical characteristics of certain circuit components were performed using Lumerical. This framework provides an environment for representing the 3D structures under study and includes various electromagnetic solvers tailored to different geometries and problems. Additionally, Lumerical can generate S-parameters models of the components, which can be used to enhance the accuracy of the simulations

## 5.2 Technology employed

The chip for this project was fabricated using SOI (Silicon on Insulator) technology, enhanced with an additional PZT (Lead Zirconate Titanate) layer for electro-optical modulation. Standard SOI substrates consist of a 2-micron silicon oxide layer topped with a 220 nm silicon layer, enabling the formation of single-mode waveguides with

high confinement. In this project, after etching the circuit components, the chip was planarized with silicon oxide before the lanthanide and PZT layers were deposited. Figure 5.1 illustrates the resulting waveguide cross section along with their respective thicknesses.

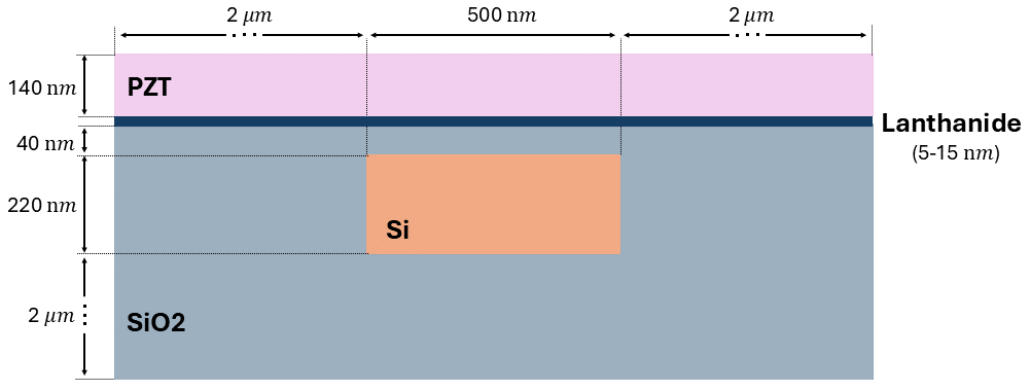


Figure 5.1: Waveguide cross-section.

To calculate the effective index ($n_{eff}$) and group index ($n_g$) of the waveguide cores with this material stack—necessary for both simulations and designing the interconnection lengths between nodes—we used Lumerical's Finite Difference Eigenmode (FDE) solver. Figure 5.2 shows the eigenmode solver window, where the E field can be observed. The most relevant mode is the fundamental (ground) mode, with $n_{eff}$ and $n_g$ values of 2.498 and 4.088, respectively.

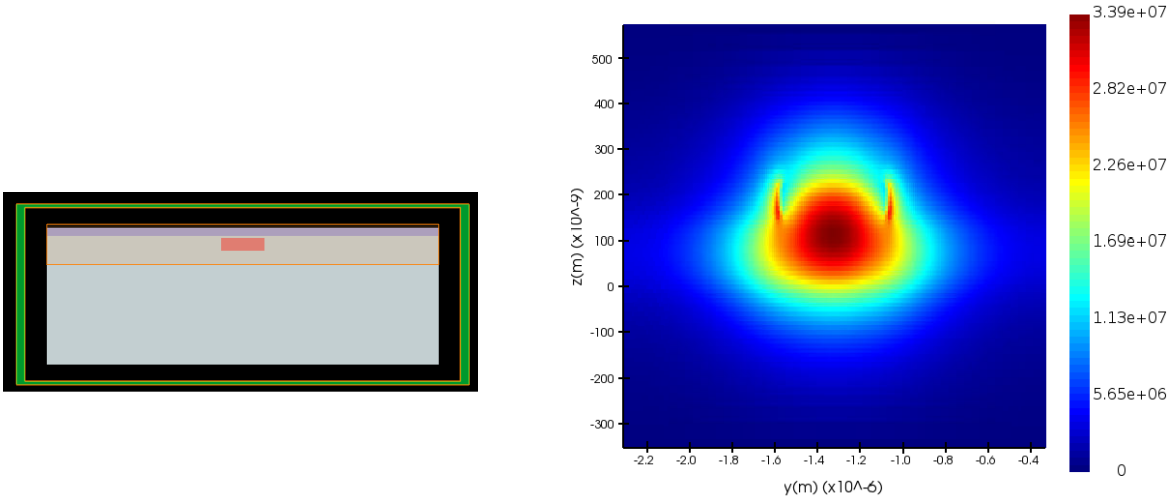


(a) (b)

Figure 5.2: Electromagnetic simulation of a waveguide cross-section. In (a), the simulated waveguide cross section can be visualized. In (b), the electric field amplitude of the cross section is observed. The colorbar represents the field amplitude in $Vm^{-1}$

.

## 5.3 Chip design

The chip that has been designed, illustrated in Figure 5.3, is composed of two main blocks: the reservoir circuit itself, on top, and the isoleted components that comprise the circuit, at the bottom. This way, it is posible to characterize both the structure under study and its constitutent parts separately, facilitating the analysis task. We can observe, in turn, 5 groups of testing devices, each with different purposes and structures, which are also highlighted in figure 5.3 (b).

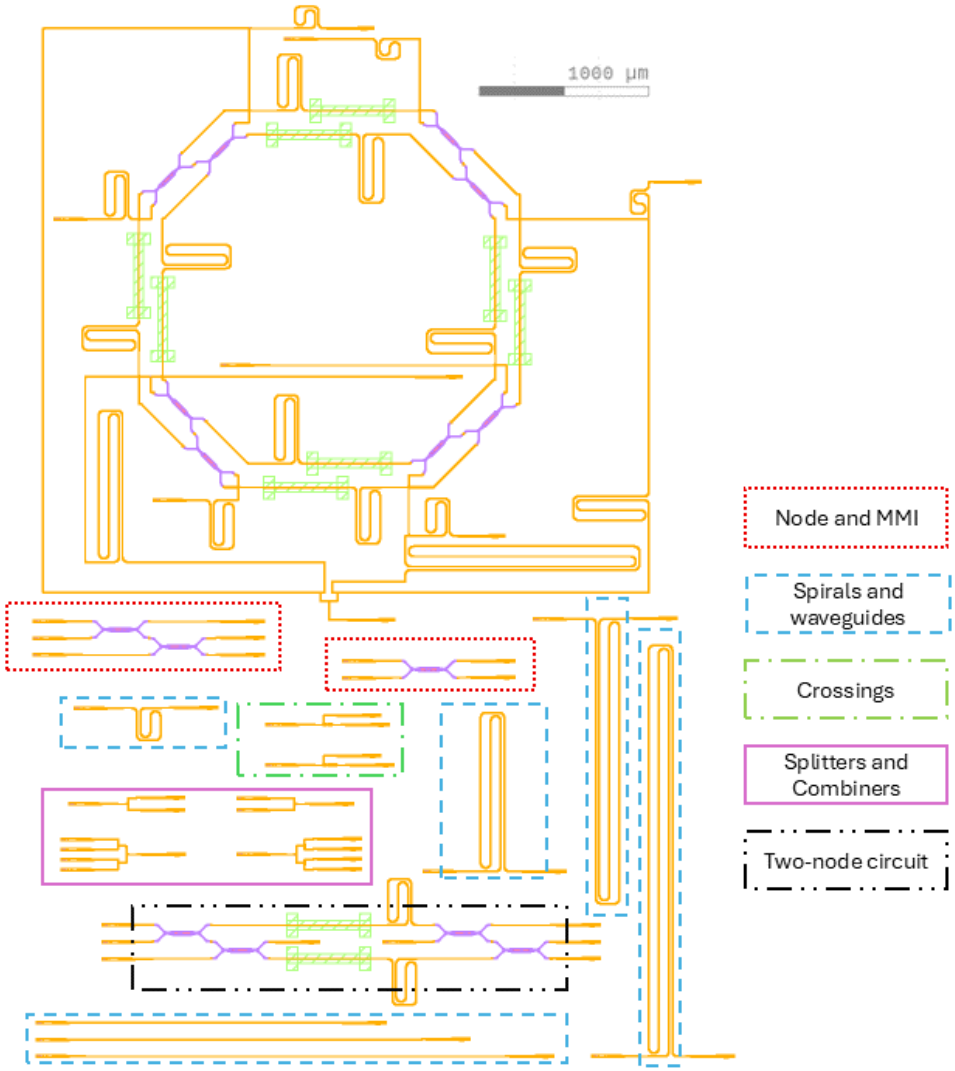


Figure 5.3: Design of the full chip with the different groups of test devices highlighted.

The chip has a total footprint of $3.9 \times 6.25 mm^2$ when considering all the components. The arrangement shown in Figure 5.3 was chosen to minimize the area used on the wafer.

Table 5.1 summarizes the most important features and parameters of the circuit. The chip has been designed on a silicon-on-insulator (SOI) platform, which explains the high refractive index gradient between the core and the cladding and the waveguide dimensions. This gradient allows for a low bend radius while still keeping the light confined. Additionally, the distance between one node and the next has been designed so that it takes one bit period of the input bitstream to travel through both interconnecting waveguides. This distance can be straightforwardly calculated using the formula $length = \frac{c}{n_g br}$, where $c$ is the speed of light, $n_g$ is the group index, and $br$ is the bitrate of the signal. In this case, $br = 32 Gbps$, as shown in Table 4.1.

| Parameter | Value |
|---|---|
| Core width | 0.5 $\mu m$ |
| Cladding width | 2 $\mu m$ |
| Deep etching depth | 220 $nm$ |
| Shallow etching depth | 70 $nm$ |
| Core $n_r$ | 3.476 ($Si$) |
| Cladding $n_r$ | 1.444 ($SiO_2$) |
| Waveguide $n_{eff}$ | 2.498 |
| Waveguide $n_g$ | 4.088 |
| Interconnection length | 2.292 $mm$ |

Table 5.1: General layout design parameters. The refractive index values have been extracted from Palik's Handbook of Optical Constants of Solids [81]. The waveguide dimensions correspond to single mode TE waveguides typical dimensions. The $n_{eff}$ and $n_g$ have been obtained through the electromagnetic simulations described in this chapter.

In the following, the reservoir circuit as well as all the 5 groups of test structures and their components are described and discussed. Additional measurements and more detailed views of every part are provided. Moreover, certain elements have been analyzed with electromagnetic simulations to further evaluate the performance of certain structures.

### 5.3.1 Reservoir circuit

The reservoir circuit has been designed to match the circuit model analyzed in previous chapters. In Figure 5.4, a closer view of the circuit, along with a comparison with the logical components, is presented. A notable feature is the large number of spirals in the reservoir. This design ensures that the signals propagating through the waveguides have the same delay from the detectors and sources to the nodes and between the nodes, ensuring that the detected interactions correspond to those previously studied. The grating couplers used by sources and detectors have been arranged so that all the gratings that couple the light into the circuit remain on the left side, while the gratings that couple the light out remain on the right side to facilitate easier and faster measurements. Spirals are used to match travel lengths of light.

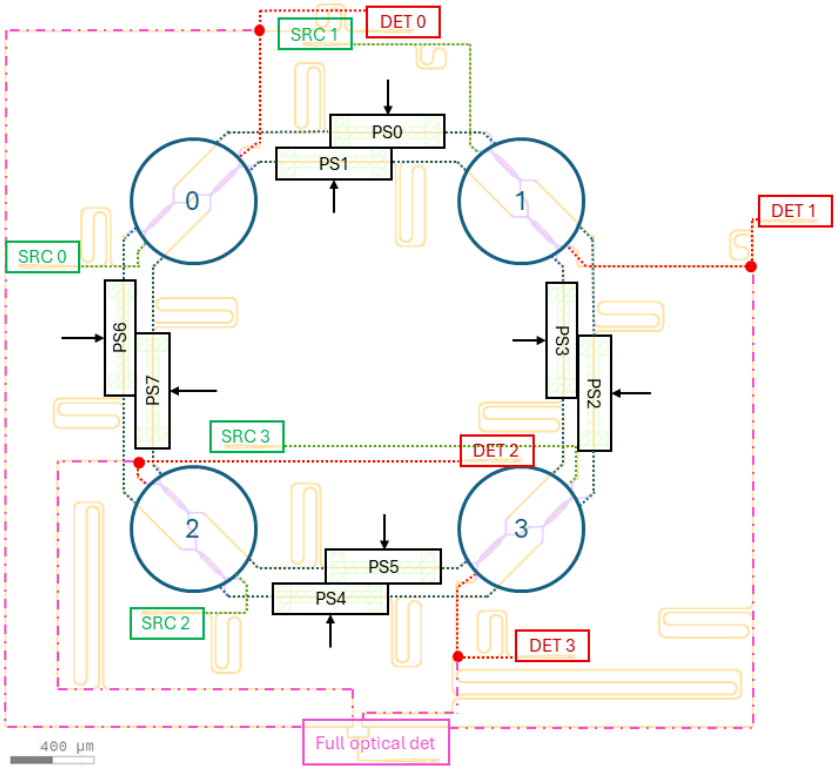


Figure 5.4: Layout design of the complete reservoir circuit with its logical analog on top of it.

Note that there is also a fully optical implementation of the circuit, highlighted in pink. The purpose of this block is to test whether directly detecting the combination of all output nodes can solve the XOR task. Some approximations attempt to include the phase shifters in these final pink interconnections, so it was found interesting to try a similar implementation but with the weights within the reservoir instead of in the output links. Moreover, this approach only requires the inclusion of splitters before the detectors, so its impact on the actual circuit is minimal.

### 5.3.2 Two-node subcircuit

Theoretical analysis and temporal simulations have shown that solving the XOR task with an ideal source signal can be achieved using just two nodes and two phase shifters. To verify this experimentally, we included a structure highlighted in black in Figure 5.3 among the test devices. This structure represents the minimum computing unit of the circuit. By isolating this unit, we can minimize the circuit's sensitivity to errors, which tend to increase as more components are added. Figure 5.5 provides a close-up view of this design.

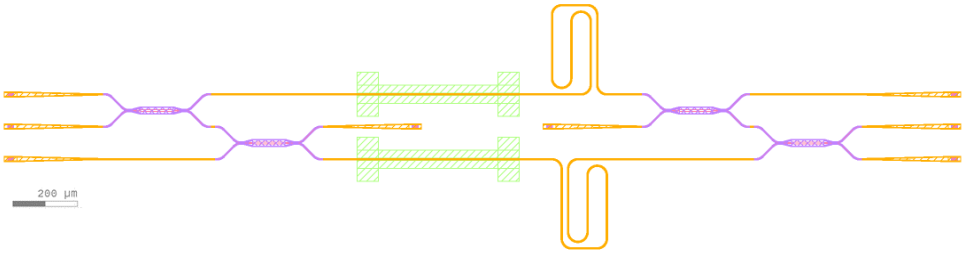


Figure 5.5: Design implementing the minimal computational unit of the circuit, a two-node reservoir subcircuit

One of the most important elements contained in this subcircuit are the phase shifters placed in the interconnections between nodes. They are implemented as metal contacts (in green) and their geometry was taken from a previous work in which the authors implemented electro-optic modulators with PZT [61] aswell. Figure 5.6 shows the final chosen geometry for the contacts.

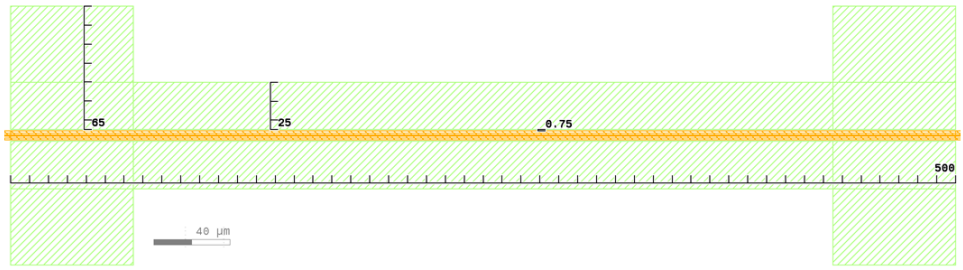


Figure 5.6: Geometric shape of the metal contacts used for the electro-optic modulation.

### 5.3.3 Node and MMI

Nodes are the fundamental components that enable computation in the circuit, making it crucial to verify their expected behavior. Figure 5.7 provides a closer view of the cascaded 2x2 MMI and its constituent element, the 2x2 MMI. The dimensions for the MMI were sourced from the iMEC PDK such that the splitting performed is balanced.


(a) (b)

Figure 5.7: On (a), the design of an isolated node conformed by cascaded 2x2 MMIs is depicted. On (b), the testing 2x2 MMI is shown.

To verify the correct behavior of the 2x2 MMI design, electromagnetic simulations were conducted using Lumerical's Eigen Mode Expansion (EME) solver. This solver propagates multiple modes to determine the response of

the device, so it is able to efficiently simulate the MMI, since it is intrinsically multimodal. In figure 5.8, the S-parameters and the electromagnetic simulation obtained with the EME solver are shown. It can be seen that the splitting performed by this device is even, as it was expected.

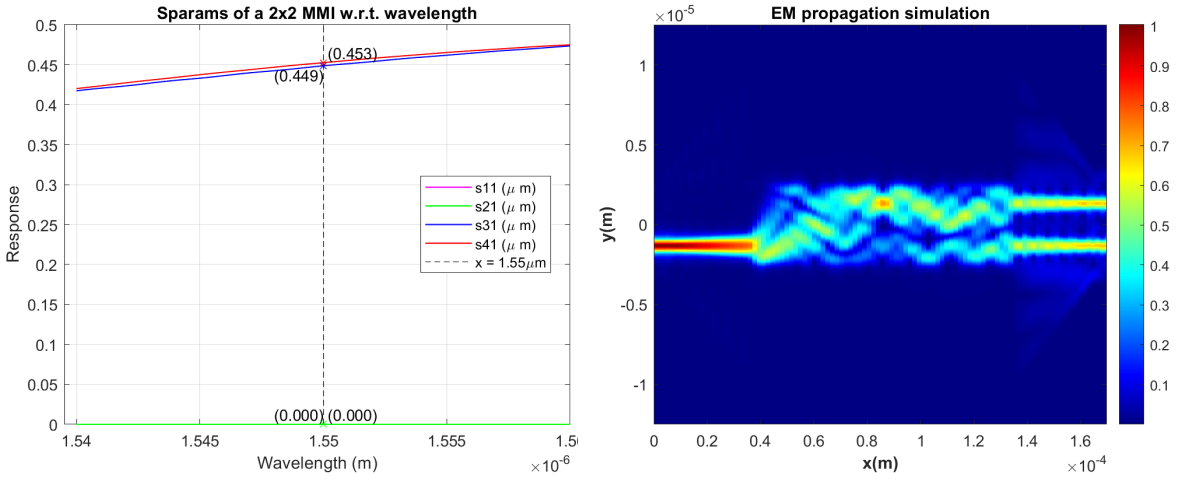


(a) (b)

Figure 5.8: (d) Response of the MMI w.r.t. frequency in terms of S-parameters. The values at the operating point of $\lambda = 1.55\mu m$ are highlighed. (e) Simulation of electromagnetic propagation of the MMI. The multiple mode as well as the balanced splitting are observed. Colorbar indicating normalized intensity.

### 5.3.4 Spirals and waveguides

The propagation loss in interconnections between components is a critical parameter that limits the circuit's capabilities. As discussed in the theoretical analysis, the amount of loss is significant because it affects the circuit's resiliency and tolerance to phase errors. Understanding this property helps in designing better experiments. However, accurately determining the loss is challenging due to the uncommon material stack and uncertainties in the fabrication process.

Grating couplers used by sources and detectors are highly wavelength-dependent and typically exhibit high losses and cause reflections upon light arrival. Manufacturing uncertainties can further modify their behavior, making proper characterization essential.

Figure 5.9a displays various testing waveguides and spirals of different sizes integrated into the chip to measure losses and reflections experimentally. A close-up view of a grating coupler and a waveguide section is provided in Figure 5.9, allowing for observation of their dimensions. Evaluating multiple lengths provides robust approximations of real errors, while the spirals offer additional insights into bend loss.

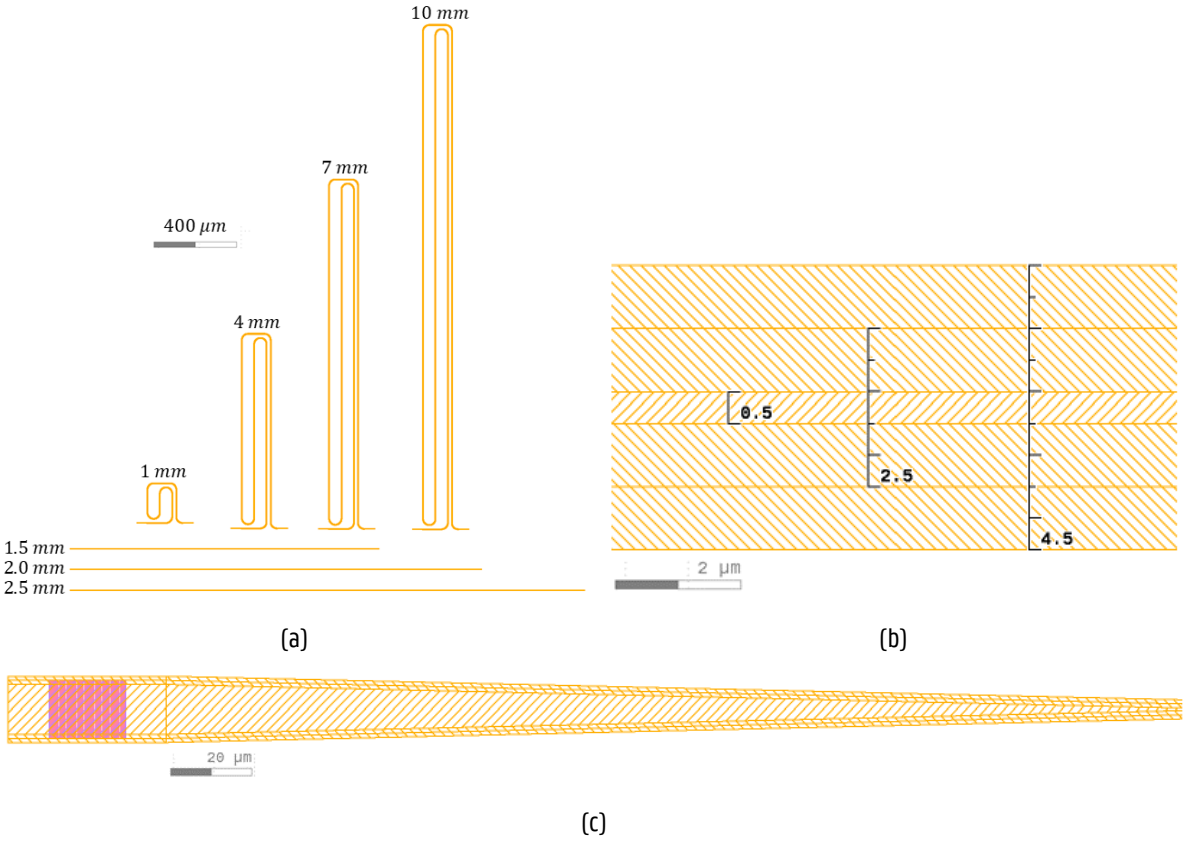


(a) (b)

(c)

Figure 5.9: (a) Multiple size test waveguides and spirals to evaluate the propagation loss in the circuit. (b) View of a waveguide section, showing the shape width, matching the ones from Table 5.1. (c) View of the grating coupler.

### 5.3.5 Splitters and combiners

The full-optical alternative implementation necessitates the use of additional splitters before the detectors and combiners to merge signals from each node. Figure 5.10 illustrates isolated testing devices for splitters and combiners, along with a close-up view of a single splitter. Again, characterizing their loss is crucial to accurately quantify the model's capabilities.

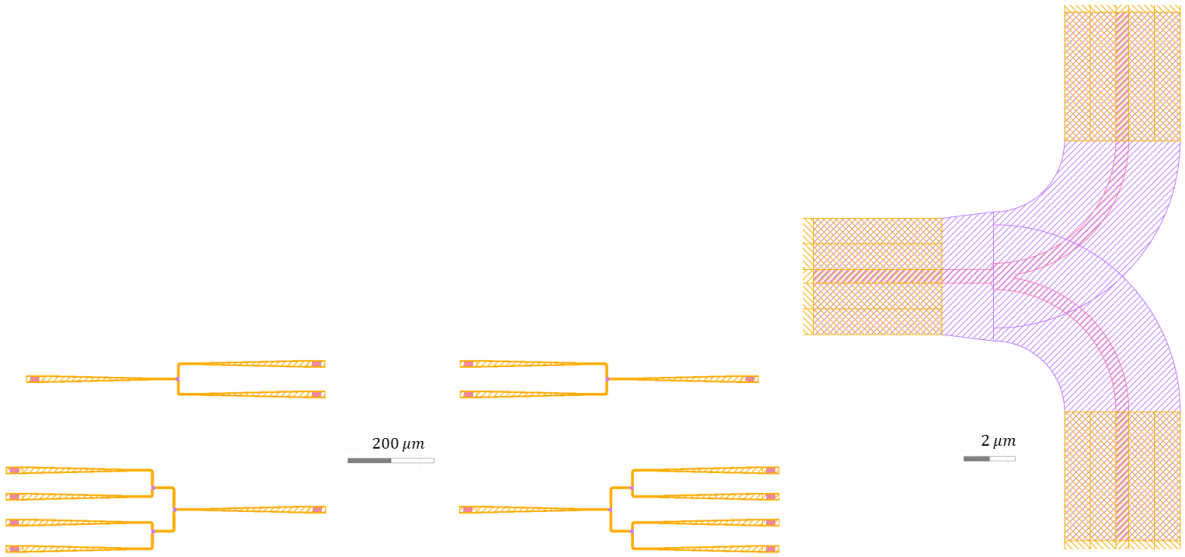


(a) (b)

Figure 5.10: (a) Testing structures of splitters and combiners. (b) Close-up view of a single splitter.

### 5.3.6 Crossings

The grating couplers are relatively long compared to the overall circuit dimensions, necessitating their placement outside the circuit and resulting in unavoidable crossings. Additionally, as previously mentioned, the gratings associated with the sources are positioned on the left, while those for the detectors are on the right, further contributing to the number of crossings. To address this, the test structures illustrated in Figure 5.11 were incorporated into the chip. These structures were designed to evaluate both the straight loss and cross talk caused by the crossings, using configurations with either a 4-crossing stack or a 6-crossing stack. Figure 5.11 also provides additional views that highlight the shape and structural details of these crossings.

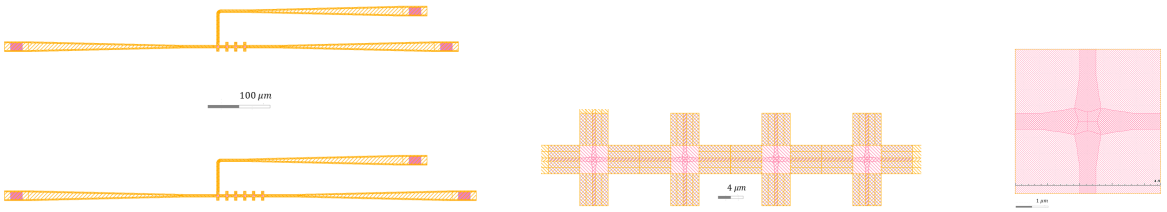


(a) (b) (c)

Figure 5.11: (a) Testing structures of crossings. Four cascaded crossings are placed in the structure on top, and four in the one on the bottom. (b) Closer view of the 4-crossing structure. (c) Single crossing full view.

# 6

# Fabrication

In this chapter, an overview of the different fabrication and processing techniques used during the fabrication is presented. Then, the entire fabrication process of the chip is described step by step.

## 6.1 Fabrication and processing techniques

### 6.1.1 Electron beam lithography

The electron beam lithography (EBL) is a mask-less technique used for the generation of custom shapes with few nanometers resolution on substrates by scanning thin layers of organic film with a beam of electrons [82]. The operating principle of this device is as follows:

First, the substrate is coated with an electron-sensitive film known as a resist. This resist changes its solubility upon exposure to the electron beam. It is called a positive resist if it becomes more soluble due to exposure, and a negative resist if it becomes less soluble.

An electron beam is then directed onto the resist and precisely controlled through lenses and electromagnetic fields to draw the desired structures. This process is known as exposure. However, the writing field - the maximum area covered by the electron beam using only the lenses and deflection systems - has a limited size, typically on the order of $100\mu m$ to $1mm$. For patterns larger than this area, the stage (which moves the substrate and aligns the electron beam) must be repositioned to cover the entire pattern. Ideally, this repositioning ensures that the new writing field aligns perfectly with the previous one without any overlap. However, achieving such perfect alignment can be challenging, leading to stitching (aligning adjacent writing fields) and pattern overlay errors, often caused by stochastic thermal drifts.

One posible solution to minimize these errors is using the Fixed Beam Moving Stage (FBMS) mode. In this mode, the stage continuously moves the substrate while the electron beam remains fixed. Although FBMS mode typically has lower resolution compared to the standard mode, it avoids stitching errors, making it suitable for large patterns that span multiple writing fields, such as waveguides [83].

After the exposure process, the resist undergoes development. In this step, the sample is immersed in a solvent that selectively removes either the exposed regions (for positive resist) or the non-exposed regions (for negative resist), thereby transferring the desired pattern onto the substrate.

### 6.1.2 Photolithography

Photolithography is a mask-based technique for creating custom patterns with sub-micron resolution on substrates by exposing a light-sensitive photoresist to light through a photomask. The process begins by coating the substrate with the photoresist, which can be either positive or negative, similar to the electron-sensitive resist used in EBL. However, unlike EBL, which directly writes patterns with an electron beam, photolithography transfers a pre-defined pattern from the photomask onto the photoresist using light.

During exposure, the photomask is placed over the photoresist-coated substrate, and light is passed through the mask to transfer the pattern onto the photoresist. The type of light used varies depending on the technology, ranging from near UV (350 to 500 nm) to deep UV (150 to 300 nm) to extreme UV (10 to 14 nm). Shorter wavelengths allow for higher resolution but also result in lower brightness due to increased material absorption.

After exposure, the photoresist is developed, revealing the pattern as either the exposed or unexposed areas are removed, depending on whether a positive or negative photoresist is used. Photolithography is essential in semiconductor manufacturing, offering a balance of precision and speed by efficiently transferring patterns across the entire substrate. [84]

### 6.1.3 Reactive-ion etching

Reactive Ion Etching (RIE) is a plasma-based etching technique used to transfer patterns onto a substrate with high precision. In RIE, the substrate coated with a resist is placed inside a reactor chamber, where a specific mixture of gases is introduced. By applying a radio frequency (RF) electric field, these gases are ionized, breaking down into reactive ions and radicals that form a plasma. The electric field then accelerates these ions toward the substrate's surface, where they can participate in two main types of etching processes: chemical and physical.

The reactive ions chemically interact with the material on the substrate, forming volatile byproducts that are evacuated from the chamber. Simultaneously, the ions can physically bombard the substrate, dislodging atoms from the surface. This dual-action process allows RIE to achieve highly anisotropic etching, which is essential for creating features with high aspect ratios and sharp, vertical sidewalls. The process is carefully calibrated so that the etch rate matches the rate at which the resist is etched away. This synchronization ensures that only the unprotected areas of the substrate are removed, allowing for accurate and consistent pattern transfer.

This technique is widely used in semiconductor manufacturing, microelectronics, PICs and microelectromechanical systems (MEMS) fabrication where detailed pattern transfer is required.

### 6.1.4 Electron-beam evaporation

Electron-beam (e-beam) evaporation is a thin-film deposition technique used to coat a substrate with a material by evaporating a target material using a high-energy electron beam. In this process, an electron beam heats the target material—typically a metal or dielectric—to a point where it transitions from a solid to a vapor phase.

This vapor then condenses onto the surface of a substrate, forming a thin, uniform film. E-beam evaporation is commonly used in the fabrication of optical coatings, semiconductor devices, and MEMS, where precise control over film thickness and composition is required [85].

### 6.1.5 Spin coating

Spin coating is a widely used technique for applying thin, uniform films to flat surfaces, often utilized in the fabrication of semiconductor devices, microelectronics, and photonics. The process involves depositing a small amount of a liquid solution (such as a polymer, photoresist, or other material dissolved in a solvent) onto the center of a substrate. The substrate is then rapidly rotated at high speeds, typically ranging from a few hundred to several thousand revolutions per minute (RPM), causing the solution to spread out evenly until the desired thickness is achieved. During this process, most of the solvent in the solution evaporates.

For spin-coated materials like resists and photoresists used in EBL and PL, respectively, a curing process is required after coating. This is done by softbaking the sample (e.g. placing the substrate on a hot plate), which removes any remaining solvents and leads to the solidification and stabilization of the coated material [86].

For the case of deposited materials like $SiO_2$ or PZT, an annealing process is carried out posterior to the spin coating at a critical temperature that ensures optimal material properties. This annealing step is crucial as it facilitates the curing of the films, improves their uniformity, enhances their adhesion to the substrate, and optimizes their structural and optical characteristics.

## 6.2 Fabrication process

The chip fabrication was performed on a Silicon on Insulator (SOI) substrate, which offers key advantages for integrated photonic circuits. The 220 nm thick silicon layer is suitable for constructing single-mode waveguides, as it supports the propagation of the fundamental TE mode with minimal interference from higher-order modes when the waveguide width is 500 nm. Additionally, the high refractive index contrast between the silicon layer and its surroundings enables tight bends, facilitating compact circuit designs. The SOI platform is also compatible with the PZT, which is used for electro-optic modulation in this design.

Even in the controlled environment of a clean room, contamination is inevitable and must be addressed before further processing. Therefore, thorough cleaning is essential both before and after each fabrication step. Different

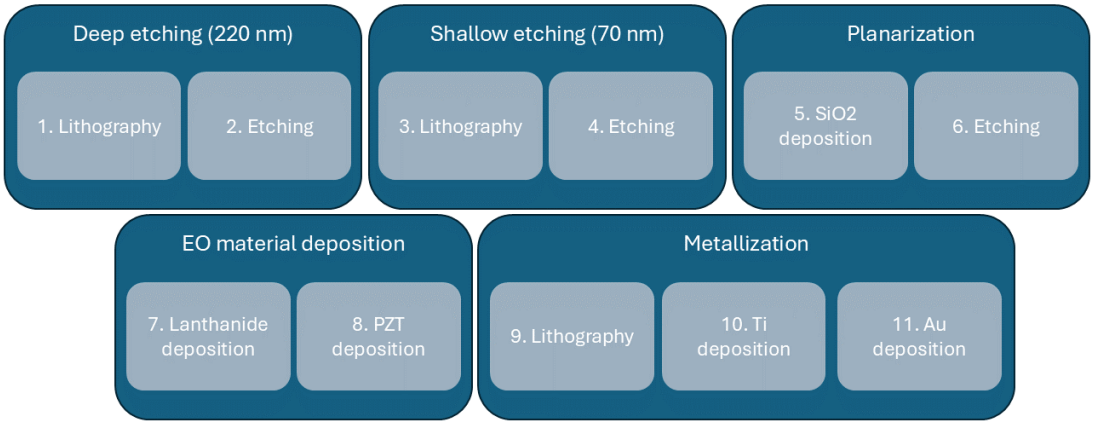


Figure 6.1: Fabrication recipe of the designed chip.

processes can introduce new particles or unwanted residues, which necessitates a systematic cleaning protocol. Two main cleaning methods are employed:

- Wet Cleaning involves sequentially rinsing the chip with acetone, isopropanol, and distilled water. Acetone and isopropanol are effective in dissolving and removing organic contaminants, while deionized water is used to eliminate any residual solvents.
- Oxygen Plasma Cleaning exposes the chip to oxygen plasma in an airtight chamber, effectively removing fine contaminants without damaging the substrate.

The fabrication of the chip follows an eleven-step process, organized into five subprocesses, as illustrated in Figure 6.1. Each step is described below, along with corresponding visualizations that depict the development of the chip's cross-section.

### 6.2.1 Block 1: Deep Etching (220 nm)

This initial step creates the 220 nm deep trenches that define the essential components of the circuit, such as waveguides, multimode interferometers (MMIs), splitters, and grating couplers. For such purpose, EBL is used to pattern the substrate with a positive resist, and the pattern is transferred to the silicon layer using RIE. The process overview is depicted in Figure 6.2.

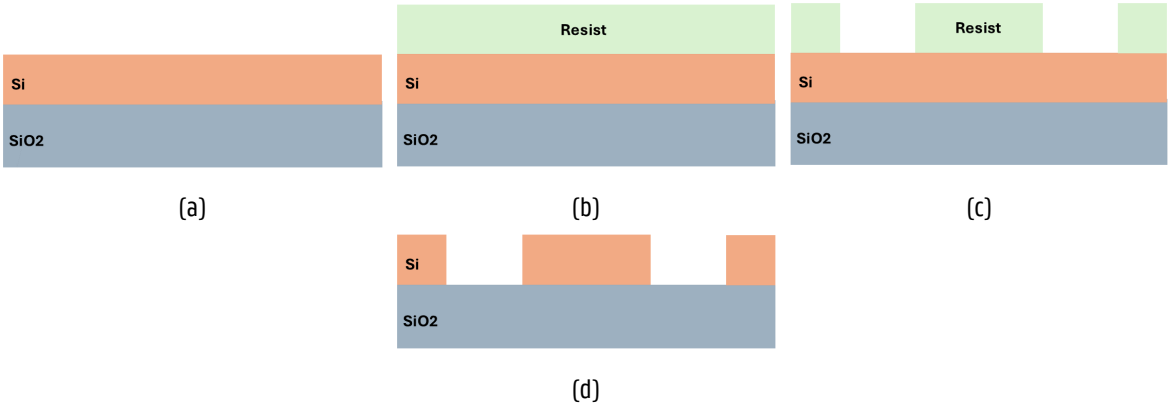


Figure 6.2: Block 1: deep etching (220 nm).

### 6.2.2 Block 2: Shallow Etching (70 nm)

The shallow etching step is responsible for forming the remaining features of the grating couplers and MMIs. This process follows a similar approach to the deep etching, with EBL patterning on a positive resist and subsequent RIE. The steps involved are shown in Figure 6.3.

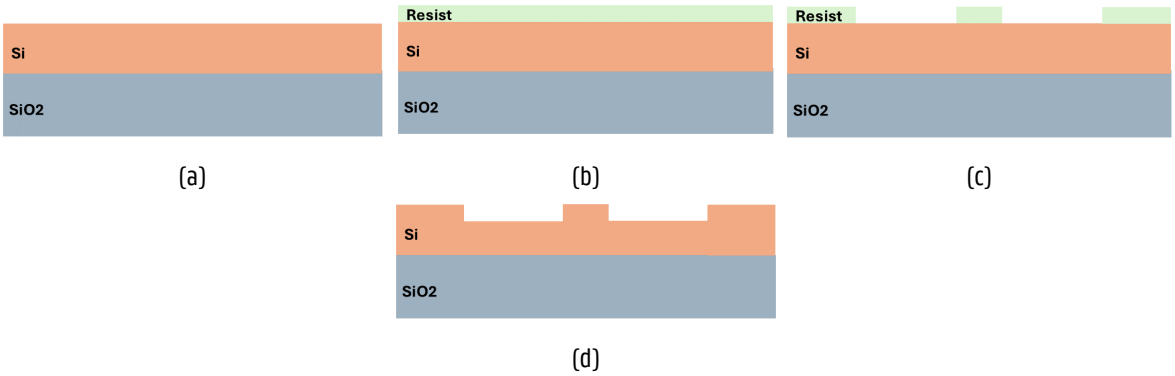


Figure 6.3: Block 2: shallow etching (70 nm).

### 6.2.3 Block 3: Planarization

Planarization is necessary to prepare the surface for the deposition of the PZT layer. Following the shallow etching, a layer of $SiO_2$ is deposited through spin coating plus annealing. Due to the non-uniformity of the underlying circuit, the deposited $SiO_2$ layer also exhibits unevenness. To achieve a flat surface, the sample undergoes RIE, which effectively levels the surface. The resulting planarized cross-section is illustrated in Figure 6.4.


(a) (b) (c)

Figure 6.4: Block 3: Planarization.

### 6.2.4 Block 4: EO material deposition

During this stage of fabrication, a lanthanide intermediate layer is first deposited onto the planarized surface, followed by a PZT layer. These layers are applied sequentially using spin coating plus annealing, which ensure uniform coverage. The lanthanide layer plays a vital role in enhancing the electro-optic properties of the PZT by promoting a high degree of orientation and reducing impurities. This, in turn, optimizes the PZT's effectiveness in electro-optic modulation. Further details on the underlying mechanisms are provided in Chapter 2. The described process is illustrated in Figure 6.5.

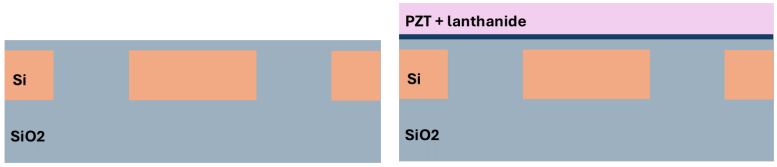


(a) (b)

Figure 6.5: Block 4: EO material deposition.

### 6.2.5 Block 5: Metallization

The final stage of fabrication focuses on depositing metal contacts critical for electro-optic modulation. This involves applying a 10 nm titanium (Ti) layer and a 40 nm gold (Au) layer. The process starts with PL to pattern a positive photoresist layer. Titanium and gold are then deposited using e-beam evaporation. Afterward, the photoresist is lifted off, taking away any excess of metals and leaving the precise contacts on the substrate. This process is illustrated in Figure 6.6.

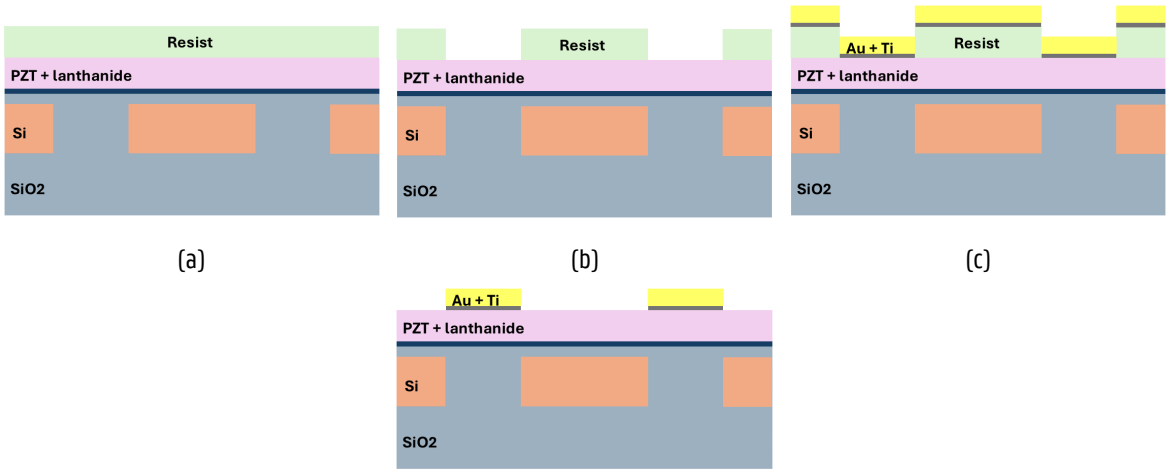


Figure 6.6: Block 5: Metallization.

# 7

# Conclusions and future steps

In this work, the analysis, simulation, and fabrication of a tunable reservoir circuit with an electrical readout, implemented as a photonic integrated circuit (PIC) on silicon-on-insulator (SOI) technology, have been carried out.

First, a suitable test problem was selected for design evaluation. This problem involves calculating the XOR between consecutive bits of an input bitstream. Telecommunications signals, modulated using on-off keying (OOK) and including typical distortions such as phase, intensity, and chromatic dispersion noises, were chosen as input. This problem fits the project's needs due to its non-linear nature, which requires the reservoir to perform part of the processing, and its low memory requirement, allowing for simpler circuit design and manufacturing processes. The distortions were introduced to make the task more realistic.

Theoretical analysis revealed that the minimal configuration of the reservoir capable of solving the problem with an ideal input signal consists of two nodes implemented with 3x3 multi-mode interferometers (MMIs), interconnected by two waveguides adjusted with phase shifters. Modifying the phase of the propagating waves conditions the interactions at the detector to obtain the desired output. The study also investigated phase noise and the feasibility of using non-volatile phase shifters, which maintain their properties without continuous electrical voltage, thereby consuming less power. The circuit is expected to show some resilience to noise, and the performance with non-volatile phase shifters should remain comparable to that with regular phase shifters.

The transmission setup used to generate the simulation signals included a coherent source with ideal linewidth, OOK modulation, a 25 km fiber, and a linear amplifier. The generated signals include distortions such as high-power effects, phase noise, chromatic dispersion, and variations in intensity. A statistical analysis of the data indicated that, except for the case with chromatic dispersion, the remaining signals should enable the XOR computation as predicted by the mathematical study.

The primary configuration examined is a 2x2 reservoir in a swirl architecture, where two consecutive nodes are used for input, and two phase shifters act as tunable parameters. Simulations involved two steps: first, propagating the input signal within the reservoir to leverage its recurrent dynamics, and second, performing linear

regression during the readout stage to obtain the output.

To assess the sensitivity of the reservoir to phase variations of the interconnections, sweeps covering all possible values of the two tunable phase shifters were conducted. To limit simulation time, each phase shifter was set to 36 values (10° increments), resulting in 1296 simulations per experiment. The initial phase shifts of the interconnections were randomly initialized, simulating the fabrication-induced random variations in actual chips.

Due to variability in circuit initialization, experiments were divided into two blocks: one with a single initialization for all six experiments to study general behavior, and another with repeated trials for the most relevant cases to reduce bias from different initializations and alternative architectures. Additional evaluations included non-recurrent circuits, where feedback loops were cut, and using all nodes as inputs. Experiments with higher-dimensional reservoirs were also performed.

The simulations yielded several conclusions about this circuit configuration and problem. It was observed that both low and high-performance operating points are present, indicating the need for configurable parameters to avoid undesired results. However, the circuit's complexity is insufficient for handling input signals with chromatic dispersion, as the pulse spreading exceeds the circuit's memory capacity. Phase noise, while degrading performance in the optimal phase shifter configuration compared to the ideal case, resulted in more stable behavior and easier identification of low-error configurations. The additional complexity provided by more nodes improved overall performance, justifying the use of such architectures even when tunable parameters are included. Results on using all nodes as inputs were inconclusive, varying with the input signal type, and excluding recurrence enhanced the performance when memory requirements were low, achieving the best results among the tested architectures. Non-volatile phase shifters with six states maintained performance similar to conventional phase shifters while reducing energy consumption. Smaller, parameterizable circuits performed as well as or better than non-parameterizable larger circuits, provided they had adequate complexity and memory.

Eventually, a PIC implementing the reservoir circuit has been fabricated. The nodes are conformed by 2x2 cascaded MMI for convenience reasons, but a similar performance and the same conclusions are expected. Unfortunately, misalignement issues during the fabrication process provoked fatal errors which don't allow to properly measure the device.

With respect to future steps, two main issues are of particular interest. First, measurements of the fabricated device are still pending, which could provide further insights into the circuit's dynamics and actual performance. Additionally, testing this architecture on different types of problems could reveal how it handles challenges beyond those addressed in this project.

Furthermore, reservoir computing, which was conceived less than 25 years ago, offers numerous research opportunities starting from this project. For instance, regarding the use of tunnable interconnections, an interesting topic to explore is the optimization of all the phase shifter values in physical systems in a scalable way. Black-box optimization techniques could provide for optimal configurations of circuits with low number of parameters, but

these fail when the optimization problem depends on many variables. Moreover, the use of configurable circuits opens the debate wheather these kinds of architectures are the best, so research exploring new architectures is also an open problem. Feed-forward circuits (without recurrency), parallelization of operations in the frequency domain or the inclusion of other active components like amplifiers that bring additional non-linearities are alternative approaches - with some of them being alredy under study - that could enhance the capabilities of spatially distributed reservoirs. Using other substrates with unique properties different to SOI, e. g. related to chromatic dispersion, loss, error resiliency or technology integration compatibilities, could also open new ways to explore the computing capabilities of photonic systems. An approach that I personally find especially interesting is the use of programmable photonic systems like the hexagonal mesh reported by iPronics [87] to test neuromorphic architectures. This would allow to try different configurations much faster and with a much lower cost, since it is not needed to fabricate a whole new device every time a new system is conceived, just as the FPGA work for the electronics.

In conclusion, the potential of photonic neuromorphic computing is vast, with numerous opportunities for research and development. This is just the beginning, and future advancements will reveal the true capabilities of this technology. The coming years promise exciting developments, and it is a privilege to witness the progress in this field.

# Bibliography


[1] I. T. Union. (2023) Facts and figures 2023 - internet traffic. [Online; accessed 16-05-2024]. [Online]. Available: https://www.itu.int/itu-d/reports/statistics/2023/10/10/ff23-internet-traffic/

[2] C. Architecture and P. Group, "The death of moore's law: What it means and what might fill the gap going forward," 2024, [Online; accessed 16-05-2024]. [Online]. Available: https://cap.csail.mit.edu/death-moores-law-what-it-means-and-what-might-fill-gap-going-forward

[3] A. B. Abdallah and K. N. Dang, *Neuromorphic computing principles and organization*. Springer, 2022.

[4] G. Van der Sande, D. Brunner, and M. C. Soriano, "Advances in photonic reservoir computing," *Nanophotonics*, vol. 6, no. 3, pp. 561–576, 2017.

[5] R. Hassan, F. Qamar, M. K. Hasan, A. H. M. Aman, and A. S. Ahmed, "Internet of things and its applications: A comprehensive survey," *Symmetry*, vol. 12, no. 10, p. 1674, 2020.

[6] P. Glauner, P. Plugmann, and G. Lerzynski, *Digitalization in healthcare*. Springer, 2021.

[7] W. Breuer and A. Knetsch, "Recent trends in the digitalization of finance and accounting," *Journal of Business Economics*, vol. 93, no. 9, pp. 1451–1461, 2023.

[8] S. Mihailă, G. Bădicu, V. Codrean, and I. Dascălu, "E-commerce in the context of globalization and digitalization: opportunities, challenges and perspectives," *European Journal of Accounting, Finance and Business*, pp. 1–9, 2021.

[9] D. Haileselassie Hagos, R. Battle, and D. B. Rawat, "Recent advances in generative ai and large language models: Current status, challenges, and perspectives," *arXiv e-prints*, pp. arXiv–2407, 2024.

[10] Y. Kim, A. Eddins, S. Anand, K. X. Wei, E. Van Den Berg, S. Rosenblatt, H. Nayfeh, Y. Wu, M. Zaletel, K. Temme *et al.*, "Evidence for the utility of quantum computing before fault tolerance," *Nature*, vol. 618, no. 7965, pp. 500–505, 2023.

[11] Y. Lu, A. Sigov, L. Ratkin, L. A. Ivanov, and M. Zuo, "Quantum computing and industrial information integration: A review," *Journal of Industrial Information Integration*, p. 100511, 2023.

[12] N. Stroev and N. G. Berloff, "Analog photonics computing for information processing, inference, and optimization," *Advanced Quantum Technologies*, vol. 6, no. 9, p. 2300055, 2023.

[13] X.-Y. Xu and X.-M. Jin, "Integrated photonic computing beyond the von neumann architecture," *ACS Photonics*, vol. 10, no. 4, pp. 1027–1036, 2023.

[14] N. Rathi, I. Chakraborty, A. Kosta, A. Sengupta, A. Ankit, P. Panda, and K. Roy, "Exploring neuromorphic com-

puting based on spiking neural networks: Algorithms to hardware," *ACM Computing Surveys*, vol. 55, no. 12, pp. 1–49, 2023.

[15] X. Liang, J. Tang, Y. Zhong, B. Gao, H. Qian, and H. Wu, "Physical reservoir computing with emerging electronics," *Nature Electronics*, pp. 1–14, 2024.

[16] M. Freiberger, "Scaling up integrated photonic reservoirs towards low-power high-bandwidth computing," Ph.D. dissertation, Ghent University, 2020.

[17] M. L. Minsky and S. A. Papert, "Perceptrons: expanded edition," 1988.

[18] F. Martinuzzi, C. Rackauckas, A. Abdelrehim, M. D. Mahecha, and K. Mora, "Reservoircomputing.jl: An efficient and modular library for reservoir computing models," *Journal of Machine Learning Research*, vol. 23, no. 288, pp. 1–8, 2022. [Online]. Available: http://jmlr.org/papers/v23/22-0611.html

[19] K. Vandoorne, W. Dierckx, B. Schrauwen, D. Verstraeten, R. Baets, P. Bienstman, and J. Van Campenhout, "Toward optical signal processing using photonic reservoir computing," *Optics express*, vol. 16, no. 15, pp. 11 182–11 192, 2008.

[20] H. Jaeger, "The "echo state" approach to analysing and training recurrent neural networks-with an erratum note," *Bonn, Germany: German National Research Center for Information Technology GMD Technical Report*, vol. 148, no. 34, p. 13, 2001.

[21] W. Maass, T. Natschläger, and H. Markram, "Real-time computing without stable states: A new framework for neural computation based on perturbations," *Neural Computation*, vol. 14, no. 11, pp. 2531–2560, 2002.

[22] M. Yan, C. Huang, P. Bienstman, P. Tino, W. Lin, and J. Sun, "Emerging opportunities and challenges for the future of reservoir computing," *Nature Communications*, vol. 15, no. 1, p. 2056, 2024.

[23] A. Yariv, P. Yeh, and A. Yariv, *Photonics: optical electronics in modern communications*. Oxford university press New York, 2007, vol. 6.

[24] K. Asakawa, Y. Sugimoto, and S. Nakamura, "Silicon photonics for telecom and data-com applications," *Opto-Electronic Advances*, vol. 3, no. 10, pp. 200 011–1, 2020.

[25] S. B. Yoo, "Prospects and challenges of photonic switching in data centers and computing systems," *Journal of Lightwave Technology*, vol. 40, no. 8, pp. 2214–2243, 2021.

[26] M. A. Butt, N. L. Kazanskiy, S. N. Khonina, G. S. Voronkov, E. P. Grakhova, and R. V. Kutluyarov, "A review on photonic sensing technologies: status and outlook," *Biosensors*, vol. 13, no. 5, p. 568, 2023.

[27] G. Tanaka, T. Yamane, J. B. Héroux, R. Nakane, N. Kanazawa, S. Takeda, H. Numata, D. Nakano, and A. Hirose, "Recent advances in physical reservoir computing: A review," *Neural Networks*, vol. 115, pp. 100–123, 2019.

[28] K. Vandoorne, J. Dambre, D. Verstraeten, B. Schrauwen, and P. Bienstman, "Parallel reservoir computing using optical amplifiers," *IEEE transactions on neural networks*, vol. 22, no. 9, pp. 1469–1481, 2011.

[29] K. Vandoorne, P. Mechet, T. Van Vaerenbergh, M. Fiers, G. Morthier, D. Verstraeten, B. Schrauwen, J. Dambre, and P. Bienstman, "Experimental demonstration of reservoir computing on a silicon photonics chip," *Nature communications*, vol. 5, no. 1, p. 3541, 2014.

[30] S. Sackesyn, C. Ma, A. Katumba, J. Dambre, and P. Bienstman, "A power-efficient architecture for on-chip reservoir computing," in *Artificial Neural Networks and Machine Learning–ICANN 2019: Workshop and Special Sessions: 28th International Conference on Artificial Neural Networks, Munich, Germany, September 17–19, 2019, Proceedings 28*. Springer, 2019, pp. 161–164.

[31] S. Sackesyn, C. Ma, J. Dambre, and P. Bienstman, "Experimental demonstration of nonlinear fibre distortion compensation with integrated photonic reservoir computing," in *2021 European Conference on Optical Communication (ECOC)*. IEEE, 2021, pp. 1–4.

[32] ——, "Experimental realization of integrated photonic reservoir computing for nonlinear fiber distortion compensation," *Optics Express*, vol. 29, no. 20, pp. 30 991–30 997, 2021.

[33] A. Katumba, J. Heyvaert, B. Schneider, S. Uvin, J. Dambre, and P. Bienstman, "Low-loss photonic reservoir computing with multimode photonic integrated circuits," *Scientific reports*, vol. 8, no. 1, p. 2653, 2018.

[34] B. Schneider, J. Dambre, and P. Bienstman, "Using digital masks to enhance the bandwidth tolerance and improve the performance of on-chip reservoir computing systems," *IEEE transactions on neural networks and learning systems*, vol. 27, no. 12, pp. 2748–2753, 2015.

[35] A. Katumba, M. Freiberger, P. Bienstman, and J. Dambre, "A multiple-input strategy to efficient integrated photonic reservoir computing," *Cognitive Computation*, vol. 9, pp. 307–314, 2017.

[36] T. Yamane, S. Takeda, D. Nakano, G. Tanaka, R. Nakane, S. Nakagawa, and A. Hirose, "Dynamics of reservoir computing at the edge of stability," in *Neural Information Processing: 23rd International Conference, ICONIP 2016, Kyoto, Japan, October 16–21, 2016, Proceedings, Part I 23*. Springer, 2016, pp. 205–212.

[37] C. Ma, J. Van Kerrebrouck, H. Deng, S. Sackesyn, E. Gooskens, B. Bai, J. Dambre, and P. Bienstman, "Integrated photonic reservoir computing with an all-optical readout," *Optics Express*, vol. 31, no. 21, pp. 34 843–34 854, 2023.

[38] I. Bauwensa, K. Harkhoea, E. Gooskensb, P. Bienstmanb, G. Verschaffelta, and G. Van der Sandea, "Increasing the nonlinear computational capacity of a spatial photonic reservoir computing system," in *Proceedings of SPIE*. SPIE, 2024.

# 7 Bibliography


[39] S. Biasi, G. Donati, A. Lugnan, M. Mancinelli, E. Staffoli, and L. Pavesi, "Photonic neural networks based on integrated silicon microresonators," *Intelligent Computing*, vol. 3, p. 0067, 2024.

[40] M. Borghi, S. Biasi, and L. Pavesi, "Reservoir computing based on a silicon microring and time multiplexing for binary and analog operations," *Scientific Reports*, vol. 11, no. 1, p. 15642, 2021.

[41] D. Bazzanella, S. Biasi, M. Mancinelli, and L. Pavesi, "A microring as a reservoir computing node: memory/nonlinear tasks and effect of input non-ideality," *Journal of Lightwave Technology*, vol. 40, no. 17, pp. 5917–5926, 2022.

[42] L. Appeltant, M. C. Soriano, G. Van der Sande, J. Danckaert, S. Massar, J. Dambre, B. Schrauwen, C. R. Mirasso, and I. Fischer, "Information processing using a single dynamical node as complex system," *Nature communications*, vol. 2, no. 1, p. 468, 2011.

[43] G. Donati, C. R. Mirasso, M. Mancinelli, L. Pavesi, and A. Argyris, "Microring resonators with external optical feedback for time delay reservoir computing," *Optics Express*, vol. 30, no. 1, pp. 522–537, 2022.

[44] C. Mesaritakis, V. Papataxiarhis, and D. Syvridis, "Micro ring resonators as building blocks for an all-optical high-speed reservoir-computing bit-pattern-recognition system," *JOSA B*, vol. 30, no. 11, pp. 3048–3055, 2013.

[45] C. Mesaritakis, A. Bogris, A. Kapsalis, and D. Syvridis, "High-speed all-optical pattern recognition of dispersive fourier images through a photonic reservoir computing subsystem," *Optics letters*, vol. 40, no. 14, pp. 3416–3419, 2015.

[46] F. Denis-Le Coarer, M. Sciamanna, A. Katumba, M. Freiberger, J. Dambre, P. Bienstman, and D. Rontani, "All-optical reservoir computing on a photonic chip using silicon-based ring resonators," *IEEE Journal of Selected Topics in Quantum Electronics*, vol. 24, no. 6, pp. 1–8, 2018.

[47] M. A. A. Fiers, T. Van Vaerenbergh, F. Wyffels, D. Verstraeten, B. Schrauwen, J. Dambre, and P. Bienstman, "Nanophotonic reservoir computing with photonic crystal cavities to generate periodic patterns," *IEEE transactions on neural networks and learning systems*, vol. 25, no. 2, pp. 344–355, 2013.

[48] F. Laporte, A. Katumba, J. Dambre, and P. Bienstman, "Numerical demonstration of neuromorphic computing with photonic crystal cavities," *Optics express*, vol. 26, no. 7, pp. 7955–7964, 2018.

[49] D. Brunner and I. Fischer, "Reconfigurable semiconductor laser networks based on diffractive coupling," *Optics letters*, vol. 40, no. 16, pp. 3854–3857, 2015.

[50] J. Bueno, S. Maktoobi, L. Froehly, I. Fischer, M. Jacquot, L. Larger, and D. Brunner, "Reinforcement learning in a large-scale photonic recurrent neural network," *Optica*, vol. 5, no. 6, pp. 756–760, 2018.

[51] J. Dong, S. Gigan, F. Krzakala, and G. Wainrib, "Scaling up echo-state networks with multiple light scattering," in *2018 IEEE Statistical Signal Processing Workshop (SSP)*. IEEE, 2018, pp. 448–452.

[52] T. Kawanishi, *Electro-Optic Modulation for Photonic Networks*. Springer, 2022.

[53] G. T. Reed, G. Mashanovich, F. Y. Gardes, and D. Thomson, "Silicon optical modulators," *Nature photonics*, vol. 4, no. 8, pp. 518–526, 2010.

[54] J. Beeckman, "Lecture notes on electro-optic effects," Lecture notes from the course Optical Materials, University of Ghent, 2024, accessed: 20-05-2024.

[55] M. Berciano, G. Marcaud, P. Damas, X. Le Roux, P. Crozat, C. Alonso Ramos, D. Pérez Galacho, D. Benedikovic, D. Marris-Morini, E. Cassan *et al.*, "Fast linear electro-optic effect in a centrosymmetric semiconductor," *Communications Physics*, vol. 1, no. 1, p. 64, 2018.

[56] T. Granzow, S. Glinsek, and E. Defay, "Piezoelectric ceramics," in *Encyclopedia of Smart Materials*, A.-G. Olabi, Ed. Oxford: Elsevier, 2022, pp. 22–34. [Online]. Available: https://www.sciencedirect.com/science/article/pii/B9780128157329000437

[57] R. Thapliya, Y. Okano, and S. Nakamura, "Electrooptic characteristics of thin-film plzt waveguide using ridge-type mach-zehnder modulator," *Journal of Lightwave Technology*, vol. 21, no. 8, pp. 1820–1827, 2003.

[58] J. P. George, P. F. Smet, J. Botterman, V. Bliznuk, W. Woestenborghs, D. Van Thourhout, K. Neyts, and J. Beeckman, "Lanthanide-assisted deposition of strongly electro-optic pzt thin films on silicon: Toward integrated active nanophotonic devices," *ACS Applied Materials & Interfaces*, vol. 7, no. 24, pp. 13 350–13 359, 2015, pMID: 26043103. [Online]. Available: https://doi.org/10.1021/acsami.5b01781

[59] G. F. Feutmba, J. P. George, K. Alexander, D. Van Thourhout, and J. Beeckman, "Hybrid pzt/si tm/te electro-optic phase modulators," in *Integrated Optics: Devices, Materials, and Technologies XXIII*, vol. 10921. SPIE, 2019, pp. 85–91.

[60] G. F. Feutmba, T. Van de Veire, I. Ansari, J. P. George, D. Van Thourhout, and J. Beeckman, "A strong pockels pzt/si modulator for efficient electro-optic tuning," in *Integrated Photonics Research, Silicon and Nanophotonics*. Optica Publishing Group, 2020, pp. ITu1A–6.

[61] G. F. Feutmba, L. Da Silva, N. Singh, L. Breyne, K. De Geest, J. P. George, J. Bauwelinck, D. Van Thourhout, X. Yin, and J. Beeckman, "High frequency characterization of pzt thin-films deposited by chemical solution deposition on soi for integrated high speed electro-optic modulators," *Optical Materials Express*, vol. 13, no. 7, pp. 2120–2134, 2023.

[62] D. Ban, G. Liu, H. Yu, Y. Wu, and F. Qiu, "Low driving voltage and low optical loss electro-optic modulators based on lead zirconate titanate thin film on silicon substrate," *Journal of Lightwave Technology*, vol. 40, no. 9, pp. 2939–2943, 2022.

[63] N. Boynton, H. Cai, M. Gehl, S. Arterburn, C. Dallo, A. Pomerene, A. Starbuck, D. Hood, D. C. Trotter, T. Fried-

mann *et al.*, "A heterogeneously integrated silicon photonic/lithium niobate travelling wave electro-optic modulator," *Optics express*, vol. 28, no. 2, pp. 1868–1884, 2020.

[64] W. Heni, Y. Kutuvantavida, C. Haffner, H. Zwickel, C. Kieninger, S. Wolf, M. Lauermann, Y. Fedoryshyn, A. F. Tillack, L. E. Johnson *et al.*, "Silicon–organic and plasmonic–organic hybrid photonics," *ACS photonics*, vol. 4, no. 7, pp. 1576–1590, 2017.

[65] S. Abel, F. Eltes, J. E. Ortmann, A. Messner, P. Castera, T. Wagner, D. Urbonas, A. Rosa, A. M. Gutierrez, D. Tulli *et al.*, "Large pockels effect in micro-and nanostructured barium titanate integrated on silicon," *Nature materials*, vol. 18, no. 1, pp. 42–47, 2019.

[66] J. Geler-Kremer, F. Eltes, P. Stark, D. Stark, D. Caimi, H. Siegwart, B. Jan Offrein, J. Fompeyrine, and S. Abel, "A ferroelectric multilevel non-volatile photonic phase shifter," *Nature Photonics*, vol. 16, no. 7, pp. 491–497, 2022.

[67] L. Photonics. (2024) Multimode interferometer (mmi). Accessed: 2024-08-16. [Online]. Available: https://academy.lucedaphotonics.com/ipkiss/picazzo/filters/mmi/

[68] R. Penrose, "A generalized inverse for matrices," in *Mathematical proceedings of the Cambridge philosophical society*, vol. 51, no. 3. Cambridge University Press, 1955, pp. 406–413.

[69] D. R. Paschotta, "Laser noise," 2024, accessed: 2024-07-18. [Online]. Available: https://www.rp-photonics.com/laser_noise.html

[70] ——, "Intensity noise," 2024, accessed: 2024-07-18. [Online]. Available: https://www.rp-photonics.com/intensity_noise.html

[71] ——, "Phase noise," 2024, accessed: 2024-07-18. [Online]. Available: https://www.rp-photonics.com/phase_noise.html

[72] ——, "Silica fibers - encyclopedia of laser physics and technology," 2024, accessed: 2024-08-13. [Online]. Available: https://www.rp-photonics.com/silica_fibers.html

[73] ——, "Scattering - encyclopedia of laser physics and technology," 2024, accessed: 2024-08-13. [Online]. Available: https://www.rp-photonics.com/scattering.html

[74] ——, "Chromatic dispersion - encyclopedia of laser physics and technology," 2024, accessed: 2024-08-13. [Online]. Available: https://www.rp-photonics.com/chromatic_dispersion.html

[75] ——, "Kerr effect - encyclopedia of laser physics and technology," 2024, accessed: 2024-08-13. [Online]. Available: https://www.rp-photonics.com/kerr_effect.html

[76] ——, "Coherence - encyclopedia of laser physics and technology," 2024, accessed: 2024-08-13. [Online]. Available: https://www.rp-photonics.com/coherence.html

[77] F. Lafavre, "Digital modulation," https://www.lafavre.us/robotics/digital-modulation.html, n.d., accessed: 2024-08-17. [Online]. Available: https://www.lafavre.us/robotics/digital-modulation.html

[78] H. O. Dries Van Thourhout, Alberto Curto, "Lecture notes on wave interference," Lecture notes from the course Microphotonics, University of Ghent, 2024, accessed: 20-05-2024.

[79] VPIphotonics, *VPIphotonics Design Suite*, VPIphotonics, Berlin, Germany, 2024, software package for photonic design and simulation. [Online]. Available: https://www.vpiphotonics.com

[80] F. Laporte, J. Dambre, and P. Bienstman, "Highly parallel simulation and optimization of photonic circuits in time and frequency domain based on the deep-learning framework pytorch," *Scientific reports*, vol. 9, no. 1, p. 5918, 2019.

[81] E. D. Palik, *Handbook of Optical Constants of Solids*. San Diego, CA: Academic Press, 1998, vol. 1.

[82] N. Pala and M. Karabiyik, *Electron Beam Lithography (EBL)*. Dordrecht: Springer Netherlands, 2016, pp. 1033–1057. [Online]. Available: https://doi.org/10.1007/978-94-017-9780-1_344

[83] J. E. Sanabia, K. E. Burcham, J. Klingfus, G. Piaszenski, M. Kahl, and R. Jede, "Fixed beam moving stage electron beam lithography of waveguide coupling device structures," in *2012 Conference on Lasers and Electro-Optics (CLEO)*, 2012, pp. 1–2.

[84] M. Madou and C. Wang, *Photolithography*. Dordrecht: Springer Netherlands, 2012, pp. 2051–2060. [Online]. Available: https://doi.org/10.1007/978-90-481-9751-4_342

[85] A. Bashir, T. I. Awan, A. Tehseen, M. B. Tahir, and M. Ijaz, "Chapter 3 - interfaces and surfaces," in *Chemistry of Nanomaterials*, T. I. Awan, A. Bashir, and A. Tehseen, Eds. Elsevier, 2020, pp. 51–87. [Online]. Available: https://www.sciencedirect.com/science/article/pii/B9780128189085000032

[86] J. Scholvin, "Spin coating of photoresist," https://web.mit.edu/scholvin/www/nt245/Documents/resists.AN.spin_coating_photoresist.pdf, 2009, accessed: 2024-08-15.

[87] D. Pérez-López, A. Gutierrez, D. Sánchez, A. López-Hernández, M. Gutierrez, E. Sánchez-Gomáriz, J. Fernández, A. Cruz, A. Quirós, Z. Xie *et al.*, "General-purpose programmable photonic processor for advanced radiofrequency applications," *Nature Communications*, vol. 15, no. 1, p. 1563, 2024.